Alma Mater Studiorum – Università di Bologna

DOTTORATO DI RICERCA IN

CHIMICA

Ciclo XXVII

Settore Concorsuale di afferenza
03/A2 - MODELLI E METODOLOGIE PER LE SCIENZE CHIMICHE

Settore Scientifico disciplinare
CHIM/02 - CHIMICA FISICA

ATOMISTIC SIMULATIONS OF LIQUID CRYSTALS IN THE BULK AND AT THEIR INTERFACES

Presentata da: Mattia Felice Palermo

Coordinatore Dottorato
Prof. Aldo Roda

Relatore
Prof. Claudio Zannoni

Correlatore
Dr. Luca Muccioli

Esame finale anno 2015

Abstract

In this thesis, we have dealt with several problems concerning liquid crystals (LC) phases, either in the bulk or at their interfaces, by the use of atomistic molecular dynamics (MD) simulations. We first focused our attention on simulating and characterizing the bulk smectic phase of 4-n-octyl-4′-cyanobiphenyl (8CB), allowing us to investigate the antiparallel molecular arrangement typical of SmA_d smectic phases. A second topic of study was the characterization of the 8CB interface with vacuum by simulating freely suspended thin films, which allowed us to determine the influence of the interface on the orientational and positional order. Then we investigated the LC-water and LC-electrolyte water solution interface. This interface has recently found application in the development of sensors for several compounds, including biological molecules, and here we tried to understand the re-orientation mechanism of LC molecules at the interface which is behind the functioning of these sensors. The characterization of this peculiar interface has incidentally led us to develop a polarizable force field for the pentyl-cyanobiphenyl mesogen, whose process of parametrization and validation is reported here in detail. We have shown that this force field is a significant improvement over its previous, static charge non polarizable version in terms of density, orientational order parameter and translational diffusion.

Contents

Chapter 1

Introduction

During the three years of Ph.D. we have tackled various problems concerning liquid crystals (LC) phases through the use of molecular dynamics (MD) simulations. Nowadays, computer simulations allow to reproduce the macroscopic properties of a given molecular system, if a suitable set of parameters describing the interaction at the atomistic, microscopic level (Force Field) is provided. Here, we exploited the atomistic MD technique to study LCs either in their bulk phase or at their interfaces. LCs are anisotropic fluids which share properties between those of isotropic liquids and solid crystals[1,2], featuring long range orientational order, like in nematics, and in some cases even positional order, such as in smectics. In addition to their peculiar long range arrangement, many LCs are also known to change their alignment if exposed to a relatively weak electric or magnetic field. LC molecules are also found to align due to the presence of interfaces, let it be with solid phases[3–6], air/vacuum and liquids, or even in the presence of certain chemical species at these interfaces[7–9].
Simulating such interfaces can be a very challenging task and, as in every complex task, we first started by tackling some (apparently) easier problems, and focused our attention on the characterization of the bulk smectic phase of 4-n-octyl-4′-cyanobiphenyl(8CB) through atomistic MD simulations. While there have been several attempts to simulate the smectic phase 8CB through the MD technique[10–13], each of them failed to reproduce certain properties, such as transition temperatures or the smectic order parameter. In our work,

which was published on the Journal of Chemical Physics[14], we undertook the non trivial task of investigating whether it was possible to reproduce the peculiar smectic SmA_d phase of 8CB employing a united atom (UA) force field recently developed by our group[15] which was specifically tuned to reproduce the the nematic phase of cyanobiphenyls. One of the fundamental issues we examined was to determine the type and extent of antiparallel arrangement in the smectic phase of molecules possessing a strong terminal dipole. We also exploited this case study to define a standard protocol for the computation of the positional order parameter, which until now could be found in literature with quite different values, although without a rigorous justification of the methods used to obtain these surprising results.

Once we became sufficiently familiar with the bulk phase of 8CB, we proceeded studying its interface with vacuum by simulating freely suspended thin films of 8CB. One of the most fascinating aspects of these smectic films is that they are extremely stable and that their thickness is quantized and varies only by a multiple of the double layer thickness[16,17]. Moreover, studying these films allowed us to observe the variation of the properties of the LC phase and of the molecular order when going from a 2D infinitely planar system to the bulk. In fact, it is well known that when interfaced with air or vacuum, smectic liquid crystals show the so called surface-freezing phenomenon[18], consisting in the enhancement of the orientational and positional order at the interface. This behaviour is quite peculiar of smectic LC phases and of molecules bearing long alkyl chains[19], as opposed to the more common surface-melting phenomenon shown by solids. Thus, through MD simulations we tried to investigate the influence of the interface with vacuum on the 8CB smectic phase, and the extent to which it enhances both the positional and orientational order in the SmA_d phase.

Another target of the PhD project has been the characterization of an even more complex system, that is the LC-water interface. This interface has recently gathered a lot of attention as it can be employed in the design of sensors apt to reveal the presence of several compounds, including biological ones[7,8,20,21].

Our main focus has been to investigate the response of the LC phase to the presence of ions, in particular the iodide one, in the water phase. In fact, it has been shown that the LC phase is responsive to the presence of ions in the water phase, also by changing its alignment from planar to homeotropic[22]. Understanding the mechanism behind this alignment process, may help to improve a rational design of sensing devices.

As the change of alignment of the LC phase may rely on electrostatic interactions, we apparently found that classic static charges force fields[23], which lack of the description of polarizability effects on molecules, may not be suited for describing such phenomena. While we successfully employed the fixed charge, non polarizable united atom (UA) model for cyanobiphenyls to reproduce transition temperatures, density, translational diffusion, SmA_d arrangement etc., it failed to reproduce the experimental findings, i.e. the homeotropic alignment of the LC phase when interfaced with water solutions of electrolytes (NaI in this case). This eventually lead us to develop a completely new polarizable force field for the pentyl-cyanobiphenyl series, based on the Drude oscillator model[24], which not only allows for a better atomistic description of the LC-water system, but that might be also employed to study other LC interfaces where electrostatic interaction and polarization processes are of relevance.

Bibliography

[1] M. J. Stephen and J. P. Straley, "Physics of liquid crystals," *Rev. Mod. Phys.*, vol. 46, no. 4, pp. 617–704, 1974.

[2] P.-G. De Gennes and J. Prost, *The physics of liquid crystals*, vol. 23. Clarendon press Oxford, 1993.

[3] W. Chen, L. Martinez-Miranda, H. Hsiung, and Y. Shen, "Orientational wetting behavior of a liquid-crystal homologous series," *Phys. Rev. Lett.*, vol. 62, no. 16, p. 1860, 1989.

[4] D.-S. Seo, S. Kobayashi, and M. Nishikawa, "Study of the pretilt angle for

5CB on rubbed polyimide films containing trifluoromethyl moiety and analysis of the surface atomic concentration of f/c (%) with an electron spectroscope for chemical analysis," *Appl. Phys. Lett.*, vol. 61, no. 20, pp. 2392–2394, 1992.

[5] A. Pizzirusso, R. Berardi, L. Muccioli, M. Ricci, and C. Zannoni, "Predicting surface anchoring: molecular organization across a thin film of 5CB liquid crystal on silicon," *Chem. Sci.*, vol. 3, no. 2, p. 573, 2012.

[6] O. M. Roscioni, L. Muccioli, R. G. Della Valle, A. Pizzirusso, M. Ricci, and C. Zannoni, "Predicting the anchoring of liquid crystals at a solid surface: 5-cyanobiphenyl on cristobalite and glassy silica surfaces of increasing roughness," *Langmuir*, vol. 29, no. 28, pp. 8950–8958, 2013.

[7] N. A. Lockwood, J. J. De Pablo, and N. L. Abbott, "Influence of surfactant tail branching and organization on the orientation of liquid crystals at aqueous-liquid crystal interfaces," *Langmuir*, vol. 21, no. 15, pp. 6805–6814, 2005.

[8] R. J. Carlton, J. T. Hunter, D. S. Miller, R. Abbasi, P. C. Mushenheim, L. N. Tan, and N. L. Abbott, "Chemical and biological sensing using liquid crystals.," *Liq. Cryst. Rev.*, vol. 1, no. 1, pp. 29–51, 2013.

[9] Y. Bai and N. L. Abbott, "Recent advances in colloidal and interfacial phenomena involving liquid crystals," *Langmuir*, vol. 27, no. 10, pp. 5719–5738, 2011.

[10] A. J. McDonald and S. Hanna, "Atomistic simulation of a model liquid crystal," *J. Chem. Phys.*, vol. 124, p. 164906, 2006.

[11] L. De Gaetani and G. Prampolini, "Computational study through atomistic potentials of a partial bilayer liquid crystal: structure and dynamics," *Soft Matter*, vol. 5, p. 3517, 2009.

[12] J. Zhang, J. Su, and H. Guo, “An atomistic simulation for 4-cyano-4’-pentylbiphenyl and its homologue with a reoptimized force field,” *J. Phys. Chem. B*, vol. 115, p. 2214, 2011.

[13] F. Chami, M. R. Wilson, and V. S. Oganesyan, “Molecular dynamics and EPR spectroscopic studies of 8CB liquid crystal,” *Soft Matter*, vol. 8, p. 6823, 2012.

[14] M. F. Palermo, A. Pizzirusso, L. Muccioli, and C. Zannoni, “An atomistic description of the nematic and smectic phases of 4-n-octyl-4’ cyanobiphenyl (8CB),” *J. Phys. Chem*, vol. 138, pp. 204901–204916, 2013.

[15] G. Tiberio, L. Muccioli, R. Berardi, and C. Zannoni, “Towards in silico liquid crystals. realistic transition temperatures and physical properties for n-cyanobiphenyls via molecular dynamics simulations,” *ChemPhysChem*, vol. 10, p. 125, 2009.

[16] F. Picano, P. Oswald, and E. Kats, “Disjoining pressure and thinning transitions in smectic-a liquid crystal films,” *Phys. Rev. E*, vol. 63, no. 2 II, pp. 1–9, 2001.

[17] W. H. De Jeu, B. I. Ostrovskii, and A. N. Shalaginov, “Structure and fluctuations of smectic membranes,” *Rev. Mod. Phys.*, vol. 75, no. 1, pp. 181–235, 2003.

[18] R. Hołyst, “Landau-Peierls instability, X-ray-diffraction patterns, and surface freezing in thin smectic films,” *Phys. Rev. A*, vol. 44, no. 6, p. 3692, 1991.

[19] X. Z. Wu, B. M. Ocko, E. B. Sirota, S. K. Sinha, M. Deutsch, B. H. Cao, and M. W. Kim, “Surface tension measurements of surface freezing in liquid normal alkanes.,” *Science*, vol. 261, no. 5124, pp. 1018–1021, 1993.

[20] J. M. Brake, M. K. Daschner, Y.-Y. Luk, and N. L. Abbott, “Biomolecular interactions at phospholipid-decorated surfaces of liquid crystals.,” *Science*, vol. 302, no. 5653, pp. 2094–2097, 2003.

[21] I.-H. Lin, D. S. Miller, P. J. Bertics, C. J. Murphy, J. J. d. Pablo, and N. L. Abbott, "Endotoxin-induced structural transformations in liquid crystalline droplets.," *Science*, vol. 332, no. 6035, pp. 1297–1300, 2011.

[22] S. K. Pal, C. Acevedo-Vélez, J. T. Hunter, and N. L. Abbott, "Effects of divalent ligand interactions on surface-induced ordering of liquid crystals," *Chem. Mater.*, vol. 22, no. 19, pp. 5474–5482, 2010.

[23] J. Wang, P. Cieplak, and P. A. Kollman, "How well does a restrained electrostatic potential (RESP) model perform in calculating conformational energies of organic and biological molecules?," *J. Comput. Chem.*, vol. 21, p. 1049, 2000.

[24] W. Jiang, D. J. Hardy, J. C. Phillips, A. D. MacKerell, K. Schulten, and B. Roux, "High-performance scalable molecular dynamics simulations of a polarizable force field based on classical drude oscillators in NAMD," *J. Phys. Chem. Lett.*, vol. 2, no. 2, pp. 87–92, 2011.

Chapter 2

Liquid Crystals

2.1 General properties of liquid crystals

The Liquid Crystal (LC) phase is a peculiar state of matter possessing properties typical to both isotropic liquids and crystals. In isotropic liquids, we find a partial correlation in the positions and orientations of the molecules only at short distances, a correlation that is usually lost after the first or second coordination shell. On the other hand, molecules in a LC phase are aligned with each other, even at large intermolecular distances, forming the large ordered domains that give rise to the intense scattering responsible of the turbidity of LC melts.

From a macroscopic point of view, LCs are quite similar to isotropic liquids, but they differ as to the molecules can be easily re-oriented by applying either weak magnetic or electric fields. Moreover, LCs are also sensitive to the topology of surfaces and thus can be aligned if placed in cells of the thickness of few μm that have received proper surface treatment, showing thus the typical anisotropy of crystals. Despite the features typical of ordered phases, LC molecules maintain rotational and translational freedom and all those properties which are typical of liquids, e.g. they adapt to the shape of their container, they feature viscosities comparable to isotropic fluids, although anisotropic, and can form free surfaces characterized by considerable surface tension.

There exists two main categories of LCs: lyotropics and thermotropic liquid

crystals. The former category is characterized by the dependence of the molecular organization on the concentration of LC in a solvent, with molecules adopting several configurations such as bilayers, dispersed micelles and micelles arranged in cubic lattices or even hexagonal ones. Instead, thermotropic liquid crystals undergo phase transitions as the temperature is changed. In this brief chapter, among the many LC phases (columnar, nematic, smectic, discotic, etc.) we will focus mainly on the nematic and smectic one, as they will be the main subject of study in this thesis.

2.2 Nematic phase

The nematic phase is probably the most common and relevant among all thermotropic phases, as it has found application in many technological devices such as LCDs. The name “nematic” finds its roots in the Greek word $\nu\eta\mu\alpha$ (nema), which means “thread”. This term is often used to describe the thread-like defects that can be recognized when observing the texture of nematic phase through a polarized light microscope. Such threads are analogous to the dislocations found in solids and are usually referred to as ’disclinations’. Typical nematic LC textures can be found in Figure 2.1.

As already mentioned, the most peculiar characteristic of the nematic phase is the presence of long-range orientational order, i.e. rod-like molecules tend to align their long molecular axis along a preferred direction called director. In absence of external orienting factors, such as an electric field or interfaces with other phases, the orientation of the director varies continuously in a random way throughout the sample. Such director fluctuations modulate the refractive index of nematics on the microscopic scale and therefore lead to a strong light scattering, from which their turbid appearance originates. Positional long-range order is instead absent in nematic phases, but a short-range arrangement of the center of mass of the molecules can be found, similarly to isotropic liquids. Nematic phases commonly show anisotropy in their physical properties, even though on average such properties usually resemble those of other organic

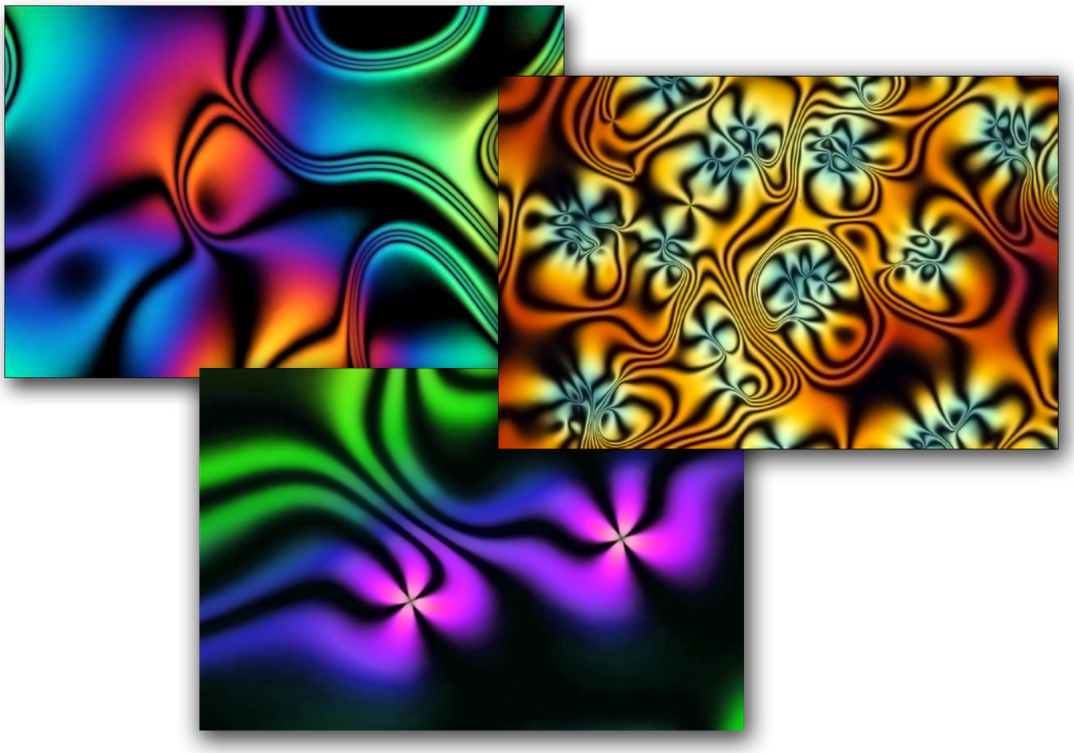

Figure 2.1: Typical schlieren textures of nematic liquid crystals observed through a polarized light microscope.

fluids. In Figure 2.2 a few common examples of molecules possessing a liquid crystalline phase are reported.

2.3 Smectic phase

Smectic phases have further degrees of order compared to the nematic ones and typically can be found at lower temperatures. The term smectic comes from the Greek word $\sigma\mu\eta\gamma\mu\alpha$ (smegma) which means soap. This due to the preponderance, at the time of their discovery, of soap-like compounds that featured this peculiar phase. Smectic phases are characterized by stratified, lamellar structures, with a well defined interlayer spacing that, depending on the specific smectic phase, can be lower than or similar to the molecular length of the single mesogen. Therefore, molecules exhibit a strong correlations in their positions in addition to the orientational ordering, similarly to solid crystals, albeit

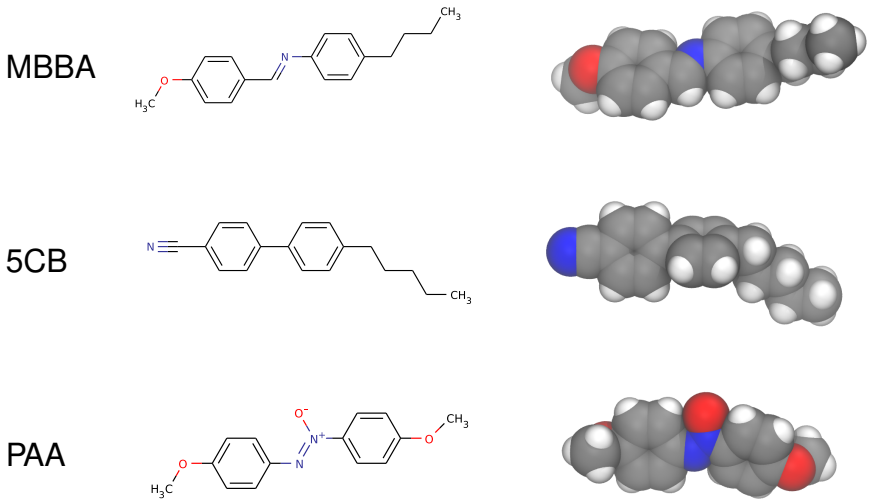

Figure 2.2: Typical liquid crystal compounds: N-(4-Methoxybenzylidene)-4-butylaniline (MBBA), 4-Cyano-4'-pentylbiphenyl (5CB), para-Azoxyanisole (PAA)

only in one dimension rather than three. Given the weakness of the interlayer attractions, layers are able to slide over one another relatively easily, giving rise to highly viscous fluid systems. Several categories of smectic phases can be found, each characterized by the extent of the in-plane positional ordering of the molecules and by the orientational order given by the tilt of the long molecular axis with respect to the layer planes.

The most simple smectic structure is the smectic A. In this phase, molecules are arranged in layers each composed by molecules with their long axis on average perpendicular to the layer planes. Within each layer, the molecular center of mass are disordered in a liquid-like fashion and they have considerable translational and rotational freedom around their long-axes. Given the flexibility of layers, distortions are often present in smectic A phases, giving rise to optical patterns known as focal-conic textures, as shown in Figure 2.3.

The long molecular axis can be tilted up to $\sim 15^{\circ}$ away from the layer normal, resulting in a layer spacing that is slightly shorter than the molecular length. However, since the tilting occurs randomly across the bulk phase, the direction of the molecules is on average perpendicular to the layer planes thus making

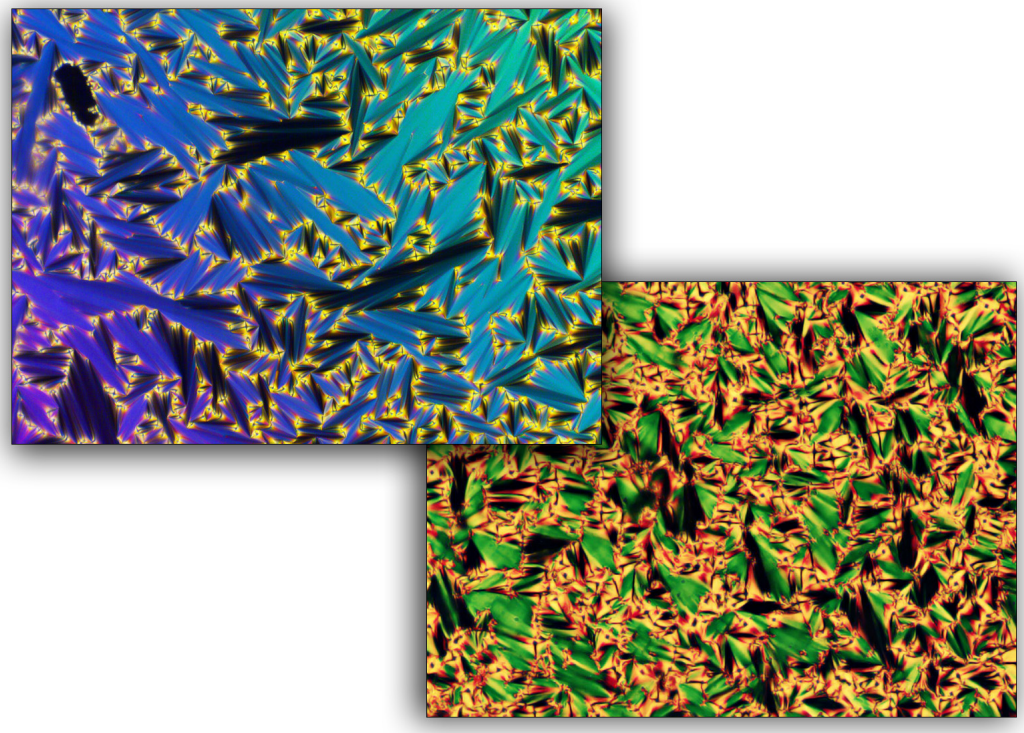

Figure 2.3: Typical focal-conic textures of smectic liquid crystals observed through a polarized light microscope.

the phase uniaxial.

Another common lamellar system is the smectic C one. In this phase, molecules are still arranged in layers, but the orientation of the molecular long axis is tilted at a temperature-dependent angle with respect to the layer planes. Many other types of smectic phases exist (S_B, S_I, S_F, S_L, S_J, S_G, S_E, SmA_d and so on), each featuring either a peculiar molecular orientation or packing.

Chapter 3

Theory of computer simulations

3.1 Molecular dynamics computer simulations

Molecular Dynamics (MD) is a computational technique that allows to simulate physical movements of atoms or molecules in a system composed by N interacting bodies. The trajectory of the interacting particles is obtained by integrating Newton's equations of motion of classical mechanics, allowing to follow the time evolution of the simulated system. Forces between simulated entities are usually modeled through the gradient of a potential energy function, and the realism of the simulation thus depends on the ability of the chosen potential to reproduce the one experienced by particles in the real system, on the numerical accuracy of the integration of the equations of motions and on the extent of the phase space explored during the simulation.

During a MD simulation, the system explores the phase space, i.e. the collection of all the states it could assume if no constraints were present. In reality, we are limited to considering systems under certain constraints (such as constant energy, temperature, pressure) and thus only a portion of the phase space is accessible, also called an *ensemble*. The extent of the accessible phase space is explored during the simulation is also a function of the simulation time and of the length-scale of the process subject to study. Thanks to continuous development of high performance computing machines, nowadays molecular dynamics simulations can possibly reach the microsecond timescale for systems as large

as 10^6 particles. System size and simulation length are strictly interconnected as the larger is a system, the longer equilibration and production times are required to obtain meaningful results.

Classical molecular dynamics methods are currently applied to tackle several classes of problems, ranging from defects in solids, fracture, biomolecules, molecular clusters, interfacial phenomena, soft matter, polymers etc. This resulted in the development of many simulation codes: among them, the most popular are Amber[1], CHARMM[2], NAMD[3], GROMACS[4] and LAMMPS[5].

3.2 Hamiltonian Dynamics

The trajectory of a system can be followed with the help of Hamiltonian dynamics. Hamiltonian dynamics was introduced as a generalization of Newton's equations for a point particle in a force field; virtually all of the fundamental models in physics are described by such dynamics. Because of Hamilton's equations are of first-order, and because of the symmetry between momenta and positions, the Hamiltonian formulation is easier to simulate numerically than other formulation such as the Euler-Lagrange.

The Lagrangian of a system is defined as

$$L = T - V \tag{3.1}$$

where T is the total kinetic energy and V is the total potential energy. Given a Lagrangian L, we can define the Hamiltonian of a system as

$$H(\mathbf{q}, \dot{\mathbf{q}}, t) = \sum_{i=1}^{n} (\dot{q}_i p_i) - L(\mathbf{q}, \dot{\mathbf{q}}, t) \tag{3.2}$$

where q_i is a generalized coordinate, p_i is a generalized momentum, that for most of the systems studied correspond to position r_i and momentum $p_i = m_i v_i$. If L is a sum of functions homogeneous (i.e., no products of different degrees) in generalized velocities of degrees 0, 1, and 2 and the equations defining the generalized coordinates are not functions of time, then the Hamiltonian can be

expressed as follows:

$$H = T + V = E \tag{3.3}$$

where T is the kinetic energy, V is the potential energy, and E is the total energy of the system.

As p_i and q_i are conjugate variables, an Hamiltonian system has always an even number of dimensions $2N$, therefore $2N$ integrals are necessary to specify a trajectory, following Hamilton's equations:

$$\dot{q}_i = \frac{\partial H}{\partial p_i} \tag{3.4}$$

$$\dot{p}_i = -\frac{\partial H}{\partial q_i} \tag{3.5}$$

$$\dot{H} = -\frac{\partial L}{\partial t} \tag{3.6}$$

These equations have fixed points when

$$\dot{q}_i = \frac{\partial H}{\partial p_i} = 0 \tag{3.7}$$

$$\dot{p}_i = -\frac{\partial H}{\partial q_i} = 0 \tag{3.8}$$

In other words an equilibrium point is found when $\nabla H = 0$, i.e. when the system reaches a critical point of the total energy function H.

A Hamiltonian system is *conservative*, as the energy is invariant along the trajectories:

$$\begin{aligned} \frac{dH}{dt} &= \sum_{i=1}^{n} \left(\frac{\partial H}{\partial q_i}\frac{\partial q_i}{\partial t} + \frac{\partial H}{\partial p_i}\frac{\partial p_i}{\partial t} \right) \\ &= \sum_{i=1}^{n} \left(\frac{\partial H}{\partial q_i}\frac{\partial H}{\partial p_i} - \frac{\partial H}{\partial p_i}\frac{\partial H}{\partial q_i} \right) \\ &= 0 \end{aligned} \tag{3.9}$$

It can also be proved that Hamiltonian flows are volume preserving. From these properties of the Hamiltonian systems follows that the trajectories obtained belongs to the microcanonical (NVE) ensemble.

Integration of motion equations and algorithms

First MD simulations studied simple fluids modelled with potentials such as the hard sphere or square well potential models, and thus particle motion could be described with very simple analytical expressions. With the introduction of more realistic continuous potentials like the Lennard-Jones one[6], the force acting on each particle instead varies continuously whenever its position and the one of the other particles change. This coupling of the motions in the system gives rise to the so called many-body problem, which cannot be solved analytically. To avoid this issue, the equations of motion are thus integrated using finite difference methods.

Finite difference techniques

The idea behind the finite difference methods is that the integration is of the equation of motion is broken down into small time frames called timestep δt. All the algorithms assume that positions and dynamics properties such as velocities, accelerations, etc. can be expanded in a Taylor series:

$$\mathbf{r}(t+\delta t) = \mathbf{r}(t) + \delta t \mathbf{v}(t) + \frac{1}{2}\delta t^2 \mathbf{a}(t) + \frac{1}{6}\delta t^3 \mathbf{b}(t) + \frac{1}{24}\delta t^4 \mathbf{c}(t) + \dots \tag{3.10}$$

The force experienced by each particle is calculated as a vector sum of its interactions with other particles, which for simplicity sake are often assumed to be pairwise additive, thus:

$$\mathbf{F}_i(\mathbf{r}_i) = \sum_{j, j \neq i} \mathbf{F}_{i,j}(\mathbf{r}_i, \mathbf{r}_j) \tag{3.11}$$

where $\mathbf{F}_{i,j}$ is the force on particle i resulting from an interaction with particle j.

Acceleration of the particles can be determined from the forces acting on them from $\mathbf{f} = m\mathbf{a}$ and, if the series is truncated at the third term, can be combined with their velocity and position in Equation 3.10 to obtain the new positions at time $(t + \delta t)$. This procedure can be iterated for as long as required, generating a trajectory of the motion of atoms. Many algorithms rely on this integration scheme, even though implemented in different flavours, each with their own strengths and weaknesses.

Verlet algorithm

The Verlet algorithm[7,8] is one of the most common integrating schemes in molecular dynamics simulations. It uses the positions and accelerations at time t, combined with the positions from the previous step, $\mathbf{r}(t - \delta t)$, to compute the new positions at time $t + \delta t$. If we write the Taylor expansion for the position at time $t + \delta t$ and $t - \delta t$:

$$\mathbf{r}(t + \delta t) = \mathbf{r}(t) + \delta t\mathbf{v}(t) + \frac{1}{2}\delta t^2\mathbf{a}(t) + \dots \tag{3.12}$$

$$\mathbf{r}(t - \delta t) = \mathbf{r}(t) - \delta t\mathbf{v}(t) + \frac{1}{2}\delta t^2\mathbf{a}(t) - \dots \tag{3.13}$$

and sum them up, we obtain:

$$\mathbf{r}(t + \delta t) \approx 2\mathbf{r}(t) - \mathbf{r}(t - \delta t) + \delta t^2\mathbf{a}(t) \tag{3.14}$$

Advantages of the Verlet algorithm are that the storage requirements are low, as only two sets of configurations ($\mathbf{r}$ and $\mathbf{r}(t+\delta t)$) and accelerations $\mathbf{a}(t)$ must be saved, and its implementation is straightforward. A drawback of this algorithm is that the positions $\mathbf{r}(t + \delta t)$ are computed by adding a small term ($\delta t^2\mathbf{a}(t)$) to the rather large $2\mathbf{r}(t) - \mathbf{r}(t - \delta t)$) one, leading to a loss of precision. Moreover, the Verlet algorithm lacks of an explicit velocity term in the equations, which are often important to obtain physical quantities such as the kinetic energy.

Velocities can be computed separately as follows:

$$\mathbf{v}(t) = [\mathbf{r}(t + \delta t) - \mathbf{r}(t - \delta t)]/2\delta t \tag{3.15}$$

but it is evident that they cannot be evaluated until the new positions have been computed at the next step. One other disadvantage is that the algorithm is not self starting, as the new positions are obtained from the current positions and the ones from the previous step.

Leap Frog

The Leap Frog algorithm is a variation of the Verlet one, and take its name after the fact that positions and velocities are evaluated alternatively at each half step.
If we subtract two Taylor expansions of the velocity at timestep $(t + \delta t/2)$ and $(t - \delta t/2)$:

$$\mathbf{v}(t + \delta t/2) = \mathbf{v}(t) + \frac{1}{2}\delta t\mathbf{a}(t) + O(\delta t^2) \tag{3.16}$$

$$\mathbf{v}(t - \delta t/2) = \mathbf{v}(t) - \frac{1}{2}\delta t\mathbf{a}(t) + O(\delta t^2) \tag{3.17}$$

we obtain the following expression for the evolution of the velocities:

$$\mathbf{v}(t + \delta t/2) = \mathbf{v}(t - \delta t/2) + \delta t\mathbf{a}(t) \tag{3.18}$$

while positions can be obtained as:

$$\mathbf{r}(t + \delta t) = \mathbf{r}(t) + \delta t\mathbf{v}(t + \delta t/2) \tag{3.19}$$

Velocity Verlet

The Velocity Verlet method[9], compared to the ones shown above, has the advantage of giving positions, velocities and accelerations at the same time without compromising the precision. It is based on a simple three-step procedure:

1. Compute $\mathbf{r}(t+\delta t) = \mathbf{r}(t) + \delta t \mathbf{v}(t) + \frac{1}{2}\delta t^2 \mathbf{a}(t)$
2. Evaluate $\mathbf{a}(t+\delta t)$ from the interaction potential for $\mathbf{r}(t+\delta t)$
3. Calculate $\mathbf{v}(t+\delta t) = \mathbf{v}(t) + \frac{1}{2}\delta t(\mathbf{a}(t) + \mathbf{a}(t+\delta t))$

Due to the presence of an additional step, this algorithm is more expensive in terms of computational cost than other integrators. That said, it must be noted that during a MD simulation only a small fraction of time is spent on the integration step, while most the most computationally expensive step is the forces evaluation, thus the impact of a third step on the performance is negligible.

Constant energy (NVE) simulations

Classical molecular dynamics simulations generate trajectories in the micro-canonical ensemble (NVE), thus obtaining systems where the total energy is conserved during the simulation. Constant energy simulations can be used during the production phase to explore the constant-energy surface of the conformational space but are not recommended for the system equilibration as it is difficult to reach the desired temperature.

Constant temperature (NVT) simulations

The constant temperature ensemble, also known as canonical ensemble, represents the possible states of a system at the thermal equilibrium, obtained by means of a termal bath which maintains the system at a specific temperature. This ensemble is significant for molecular dynamics simulations as most of the

real-life laboratory experiments are carried out at constant temperature, or often it is desirable to obtain trends of specific observables as a function of the temperature.

Running simulations at a specific temperature is not a trivial task, and some modifications to the algorithms of classical molecular dynamics are required to obtain the canonical ensemble. The temperature T of a system is related to the average kinetic energy with the equipartition theorem:

$$\left\langle \sum_i \frac{\mathbf{p}_i^2}{2m_i} \right\rangle = \langle K \rangle = \frac{3}{2} NkT \tag{3.20}$$

$$T = \frac{1}{3kN} \left\langle \sum_i \frac{\mathbf{p}_i^2}{m_i} \right\rangle \tag{3.21}$$

where $\mathbf{p}_i = m_i \mathbf{v}_i$ is the momentum of a particle i, m_i is the mass of the particle, N is the total number of particles in the system and k is the Boltzmann constant. There are several techniques to obtain constant temperature molecular dynamics, each with its own advantages and disadvantages:

- scaling velocities methods (simple velocity scaling and Berendsen thermostat)
- stochastic forces and/or velocities methods (Andersen and Langevin thermostats)
- "extended Lagrangian" methods (Nosé-Hoover thermostat)

Velocity scaling thermostats

Velocity scaling is the simplest way to implement constant temperature into molecular dynamics simulations, as it just requires to rescale the velocities of all particles by a certain factor in order to obtain the desired temperature. Velocity rescaling schemes do not strictly follow the canonical ensemble, even though in practice they deviate from the canonical only by a small amount. With this approach, the velocities of all particles is rescaled periodically by a constant factor λ, defined as:

$$\lambda = \sqrt{T/T_i} \tag{3.22}$$

where T_i is the instantaneous temperature of the system, calculated from equation 3.21 and T is the temperature of the thermal bath.

Another popular velocity rescaling scheme is the one proposed by Berendsen[10], often called weak-coupling thermostat. Here, the rescaling factor λ is again a function of the deviation of the instantaneous temperature T_i from the average value T:

$$\lambda = \sqrt{1 + \frac{\delta t}{\tau_T}\left(\frac{T}{T_i} - 1\right)} \tag{3.23}$$

where δt is the time step of the MD simulation, τ_T is the so-called "rise time" of the thermostat, and has the dimension of a time. τ_T defines the strength of the coupling with the thermostat: large values of τ_T lead to a weaker coupling and thus a longer time will be needed to drift back to the desired T after a change in the instantaneous temperature T_i.

These two isokinetic thermostats are not appropriate for the conduction of a simulation in the canonical ensemble as they do not correspond to the condition of constant temperature, that is temperature and kinetic energy fluctuations follow different laws, but can be effectively used for equilibration purposes as they both lead to trajectories whose average values correspond to those of the canonical ensemble.

Stochastic forces thermostats

Differently from velocity rescaling schemes, stochastic forces thermostats correctly sample the NVT ensemble, and the most simple implementation is perhaps the Andersen scheme[11]. In this thermostat, the coupling to a heath bath is obtained by stochastic collisions that periodically act on random select parti-

cles.

In order to maintain a constant temperature, two parameters need to be specified: the desired temperature T and the frequency of stochastic collisions ν which determines the strength of the heat bath. Provided that successive collisions are uncorrelated, the probability that a collision will take place is described by a Poisson distribution:

$$P(t, \nu) = \nu e^{-\nu t} \tag{3.24}$$

In the event of a particle suffering a collision, the value of the momentum of the particle after the collision is chosen at random from a Maxwell-Boltzmann distribution at temperature T.

Another popular stochastic force scheme is the Langevin thermostat. Here, the desired temperature is obtained by assuming that the system being simulated is embedded in a continuum of small fictional particles. At each time step, all the particles in the system are subject to random forces and have their velocities slowed down through constant friction, thus obeying the "fluctuation-dissipation" theorem and therefore obtaining a NVT ensemble.

In the Langevin scheme, the particle-i equation of motion is thus modified:

$$m\mathbf{a}_i = -\nabla_i U - m\Gamma\mathbf{v}_i + \mathbf{W}_i(t) \tag{3.25}$$

where, Γ is a friction coefficient and $\mathbf{W}_i$ is a random force which is not time and particle correlated.

A disadvantage of stochastic thermostats is that information on the dynamics of the system are lost as the algorithms randomly decorrelate particle velocities, thus observables such as the diffusion coefficient cannot be computed when using these schemes.

"Extended Lagrangian" methods

The most common thermostat of this class is the Nosé-Hoover thermostat[12,13]. The name "Extended Lagrangian" comes from the idea of describing the effect of an external heat reservoir by means of an additional degree of freedom. This degree of freedom is introduced into the system's Hamiltonian, therefore deriving new equations of motion which are integrated together with the regular equations for spatial coordinates and momenta. New "virtual" variables $\{\pi_i, \rho_i\}$ are also introduced and are related to the real ones $\{p_i, q_i\}$ as follows:

$$p_i = \pi_i/s, \quad q_i = \rho_i, \quad s = \frac{\delta\tau}{\delta t} \tag{3.26}$$

where τ is the virtual time, t is the real time and s is scaling factor. An effective mass M_s is also introduced to connect a momentum to the additional degree of freedom π_s, thus obtaining the following Hamiltonian:

$$H^* = \sum_{i=1}^{N} \frac{\pi_i^2}{2m} + U(\rho_1, \rho_2, ..., \rho_N) + \frac{\pi_s^2}{2M_s} + gk_bTln(s) \tag{3.27}$$

where $g = 3N + 1$ is the number of degrees of freedom of the extended system (N particles + 1 the new degree of freedom). The effective mass M_s is the parameter that determines the rate of the heat transfer, and its value must be set so that it is neither too small nor too large: in the former case the phase space of the system will not be canonical while the latter would result in a inefficient temperature control. Nosé has shown that this new Hamiltonian H^* results in a probability density in the phase space that corresponds to the canonical, NVT ensemble[12].

Constant pressure (NPT) simulations

Molecular dynamics simulations can be run also in the constant pressure, constant temperature NPT ensemble. The pressure of a system can be calculated

from the trace of the pressure tensor:

$$P = \frac{1}{3} Tr(\mathbf{\Pi}) \tag{3.28}$$

where $\mathbf{\Pi}$ is defined as the sum of the (always positive) kinetic energy contribution plus the interparticle energy contribution $\mathbf{W}$:

$$\begin{aligned} \mathbf{W} &= \sum_{i=1}^{N} \mathbf{r_i} \otimes \mathbf{f_i} \\ \mathbf{\Pi} &= \frac{1}{V} \left[\sum_{i}^{N} m_i (v_i \otimes v_i) + \mathbf{W} \right] \end{aligned} \tag{3.29}$$

In the case where a cutoff scheme is used, the interparticle energy contribution $\mathbf{W}$ must be computed from pairwise force and not from the total force acting on each particle[14].

Weak coupling barostat

The most popular scheme for pressure control in molecular dynamics simulation is the so-called Berendsen barostat. Pressure is kept constant to the desired value P_{ext} during the simulation by periodically rescaling the coordinates of the center of mass of the molecules or particles and the box size, following the relation:

$$\frac{dP}{dt} = (P_{\text{ext}} - P)/\tau_P \tag{3.30}$$

which can be integrated in order to obtain the pressure after a timestep δt:

$$P(t + \delta t) = P(t) + [P_{ext} - P(t)] \frac{\delta t}{\tau_p} \tag{3.31}$$

where τ_p is the pressure coupling time constant. In the case of isotropic rescaling of coordinates and box size, the scaling factor η is defined as:

$$\eta = \left[1 + \frac{\delta t}{\tau_p}\beta(P - P_{ext})\right]^{1/3} \tag{3.32}$$

where β is the isothermal compressibility of the system, which influences the frequency of pressure fluctuations during the simulation but does not affect the average value of the pressure.
If an anisotropic rescaling is desired, or in the case of simulations in orthogonal boxes, coordinates must be rescaled through an anisotropic rescaling matrix $\mathbf{h}$. If we define a variation matrix $\mathbf{M}$ as:

$$\mathbf{M} = \left[\frac{\beta}{\tau_p}(\mathbf{\Pi} - P_{ext}\mathbf{I})\right] \tag{3.33}$$

then we can obtain the rescaling $\mathbf{h}$:

$$\mathbf{h}(t + \delta t) = \mathbf{h}(t) + \mathbf{M}\mathbf{h}(t) \tag{3.34}$$

Coordinates can therefore be scaled as follows:

$$\mathbf{r}_{scaled} = \mathbf{h}(t + \delta t)\mathbf{h}^{-1}(t)\mathbf{r} \tag{3.35}$$

Periodic boundary conditions

When running a MD simulation, we are limited to a number of particles of the order of 10^6 or less, due to the computational cost to simulate a larger sample. This poses a great problem when we wish to study the properties of macroscopic systems, typically composed by a number of molecules in the order of $10^{21} \div 10^{23}$. In macroscopic systems, only a small part of the atoms are located

in proximity of the boundaries. If for example we consider a system composed by $N = 10^{23}$ spherical particles placed one close to each other in a cubic lattice, the number of atoms in proximity of the surface would be approximately 10^{16}, meaning that only 1 atom over 10^7 is exposed to the boundaries. If we compute the same value for a typical MD sample of $N = 10^6$ particles, we obtain that 1 atom over about 20 is exposed to the boundaries, resulting in a system dominated by surface effects. Thus, unless we are specifically interested in simulating a small cluster of molecules in vacuum, a workaround is needed in order to simulate bulk systems.

The most convenient approach to avoid the issue of the finite size of MD samples and to minimize surface effects is to apply the so-called periodic boundary conditions (PBC) to the system. PBC are achieved by surrounding the original simulation box with its own replicas. Thus, if a molecules leaves or enters the original box, one of its images will enter or leave through the opposite face, so that the number of particles is conserved during the simulation.

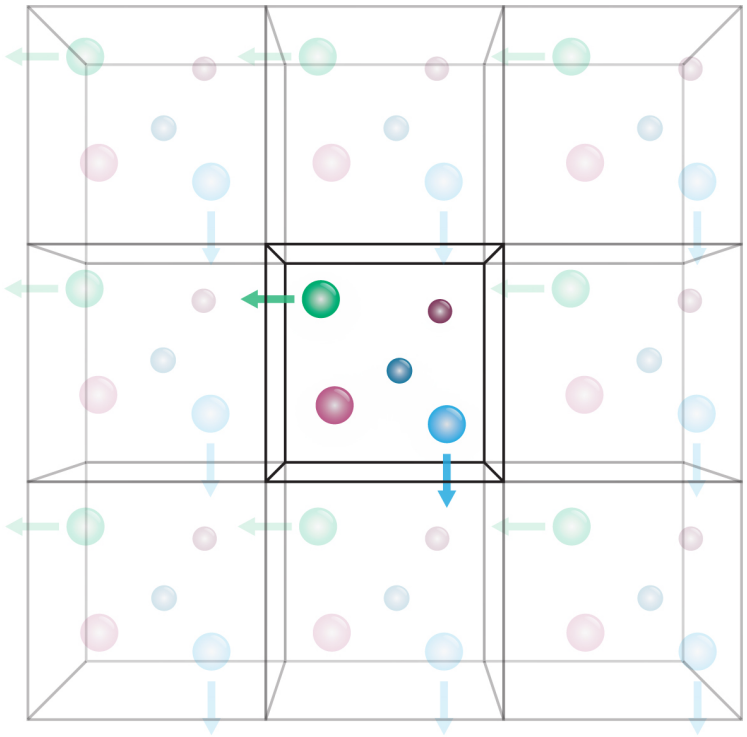

Figure 3.1: Graphical representation of periodic boundary conditions. It can be seen that each particle moving outside of the central cell (in green and blue) automatically enters from the opposite side.

As a result of the use of PBCs, each particle in the simulation box will not only interact with other particles but also with its and their periodic images. If the range of the molecular interaction is less than half side length, the central box comprises all interactions and thus we use the *minimum image convention*: the distance between two different particles i and j is taken as the distance between i and the nearest image of j[15]. As a result, every particle i interacts only with the nearest image of another molecule j. Nevertheless, it must be noted that most simulation packages evaluate potentials using cutoff schemes in order to improve the computational efficiency. Thus, a particle does not interact with all the nearest images of the other $N-1$ particles, but only with those contained in a sphere of a certain cut-off radius R_c.

3.3 Force Fields

Molecular mechanics

Theoretical studies of molecules allow to analyze the relationships between structure, function and dynamics at the atomic level. Since the majority of the problems that one would like to address in complex chemical systems involve many atoms, it is not yet feasible to treat these systems using quantum mechanical (QM) methods.

The answer to the need of high detail at low computational cost is Molecular Mechanics (MM), a technique which uses classical mechanics to analyze the structure and dynamics of molecular systems.

Within this approximation, the molecule is treated at the chemical atomic level, i.e. the electrons are not treated explicitly. The energy and the forces are calculated through a given set of potential energy functions, or *force field* (FF), which is translationally and rotationally invariant and depends on the relative positions of the atoms and on a number of parameters that have been determined either experimentally or via quantum mechanical calculations. In this way, given a particular conformation or configuration, the energy of the system

can be calculated straightforwardly.

The interatomic interactions are typically described by simple two-, three-, and four-body potential energy functions. This classical force field-based approach is a great simplification over quantum chemistry, which describes systems in terms of nuclei, electrons, and wavefunctions. This simplicity allows molecular mechanics to be applied to much larger systems than those that can be studied by QM methods.

Current generation force fields provide a reasonably good compromise between accuracy and computational efficiency. They are often calibrated to experimental results and quantum mechanical calculations of small model compounds. The development of parameter sets is a very laborious task, requiring extensive optimization. This is an area of continuing research and many groups have been working over the past two decades to derive functional forms and parameters for potential energy functions of general applicability to biological molecules. During the past ten years, several force fields have been developed for protein simulations, such as CHARMM[16], GROMOS[17] and OPLS/AMBER[18,19] force fields, while the UFF[20] and MM3[21] force fields are more likely used to study small, isolated molecules. Most recent force fields that have obtained some success are the NERD[22] united atom FF for hydrocarbons and the very complex, yet effective, COMPASS force field[23].

The most important limitation of traditional force fields is that no drastic changes in electronic structure are allowed, i.e., no events like bond making or breaking can be modeled. If one is interested in treating chemical reactions, a quantum mechanical treatment or an alternative, new formulation of force fields is necessary, like the REAXFF one[24].

Recent developments regarding force fields are focused on the explicit inclusion of the electronic polarization for the treatment of nonbonded interactions, leading to the so called polarizable or non additive force fields. This in principle will allow to simultaneously treat molecules in environments with significantly different polar character with high accuracy[25].

The potential

The typical potential energy function is a sum of diverse bonded and non–bonded contributions, each of them containing a sum over the atoms or groups of atoms.

$$U_{\text{total}} = U_{\text{bonds}} + U_{\text{angle}} + U_{\text{dihed}} + U_{\text{LJ}} + U_{\text{charge}} \tag{3.36}$$

$$U_{\text{bonds}} = \sum_{\text{bonds}} K_r^{t_i t_j} (r_{ij} - r_{eq}^{t_i t_j})^2 \tag{3.37}$$

$$U_{\text{angles}} = \sum_{\text{angle}} K_\theta^{t_i t_j t_k} (\theta_{ijk} - \theta_{eq}^{t_i t_j t_k})^2 \tag{3.38}$$

$$U_{\text{dihed}} = \sum_{\text{dihed}} V_\phi^{t_i t_j t_k t_l} [1 + \cos(n^{t_i t_j t_k t_l} \phi_{ijkl} - \gamma^{t_i t_j t_k t_l})] \tag{3.39}$$

$$U_{\text{LJ}} = 4 \sum_{i<j} f_{LJ}^{1,4} \, \epsilon_{t_i t_j} \left[\left(\frac{\sigma_{t_i t_j}}{r_{ij}} \right)^{12} - \left(\frac{\sigma_{t_i t_j}}{r_{ij}} \right)^{6} \right] \tag{3.40}$$

$$\text{where} \quad \epsilon_{t_i t_j} = (\epsilon_{t_i} \epsilon_{t_j})^{\frac{1}{2}} \, , \; \sigma^{t_i t_j} = \frac{\sigma_{t_i} + \sigma_{t_j}}{2}$$

$$U_{\text{charge}} = \sum_{i<j} f_q^{1,4} \, \frac{q_i q_j}{r_{ij}} \tag{3.41}$$

The terms contributing to the energy reported above are common to the majority of the currently used force fields, including CHARMM, AMBER, GROMOS, OPLS among others. The variables contained in Equations 3.37–3.41 are distances r_{ij}, angles θ_{ijk} and dihedral angles ϕ_{ijkl}; all the other terms are force field parameters.

The first ‘bonded’ sum is over bonds between atom pairs; the second sum is over bond angles defined by three atoms; the third sums is over atom foursomes. In the ‘nonbonded’ interactions (Lennard Jones and electrostatics), the summation is over atom pairs and j, where $i < j$ simply ensures that each interaction is counted only once. Generally, atoms separated by one or two bonds are excluded from the nonbonded sum, and those separated by three bonds, the so called ‘1-4 interactions’, may have nonbonded interactions reduced by a multiplicative scale factor ($f_{LJ}^{1,4}$,$f_q^{1,4}$). For bookkeeping purposes, each atom is assigned a number, but it is unlikely to have specific parameters for each atom;

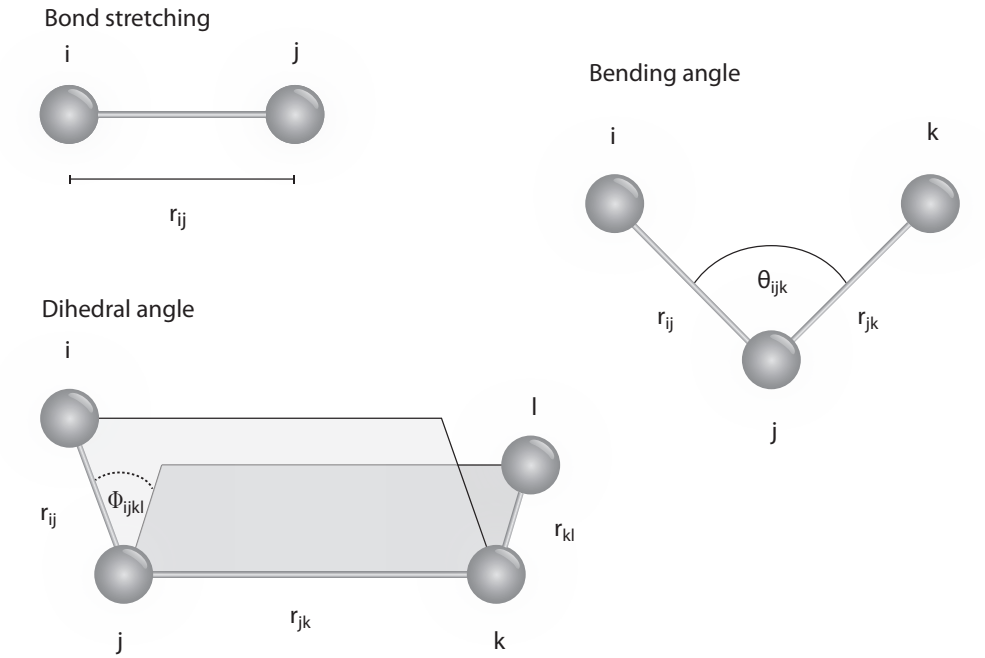

Figure 3.2: Graphical representation of bonded interactions.

instead the force fields are based on the concept of atom types (t_i,t_j), i.e. a set of parameters defined for a chemical type of atom that can possibly used in the MM description of a class of molecules, rather than for single molecular species (e.g. methylene carbon or aromatic carbon are typical atom types).

Bonded interactions

This type of interactions has the main purpose of correctly describing the equilibrium geometry of the molecule, but to a certain extent also to reproduce its conformational space. The description of bonded interactions is based on the molecular topology, i.e. on a fixed connection matrix, making this approach clearly not feasible to describe chemical reactions. As a convention, the bonded energy minimum is set as zero, so the bonded energy is always positive. Bonded interactions are represented schematically in Figure 3.2.

Bonds and angles

The standard way to approximate the potential energy for a bond in molecular mechanics is to use a Hooke's law term:

$$U_{\text{bond,Hooke}} \;=\; K(r_{ij} - r_{eq})^2 \tag{3.42}$$

where r_{ij} is the distance between the two bonded atoms i, j, r_{eq} is the equilibrium bond length and K is a force constant.

The shape of the potential energy well will be parabolic (see Figure 3.3) and the motion will therefore tend to be harmonic. This kind of approach does not attempt to reflect the energy of formation of the bond - it only seeks to reflect the energy difference on a small motion about the equilibrium value. A much more accurate representation of the bond stretching is based on the application of the Morse potential, which has an anharmonic potential energy well as shown in Figure 3.3.

$$U_{\text{bond,Morse}} \;=\; D_e[1 - e^{-(r_{ij} - r_{eq})}]^2 \tag{3.43}$$

where D_e is the "equilibrium" dissociation energy of the molecule (measured from the potential minimum). This formulation is not commonly used for applications in which the main focus is on the study of structural details, but is necessary if one is interested in spectroscopic applications.

A bond angle between atoms i-j-k is defined as the angle between the bonds i-j and j-k. As bond angles, in a similar manner to bond lengths, are found, experimentally and theoretically, to vary around a single value, it is sufficient in most applications to use an harmonic representation in order to provide an accurate description:

$$U_{\text{angle}} \;=\; K_{\theta}^{t_i t_j t_k}(\theta_{ijk} - \theta_{eq}^{t_i t_j t_k})^2 \tag{3.44}$$

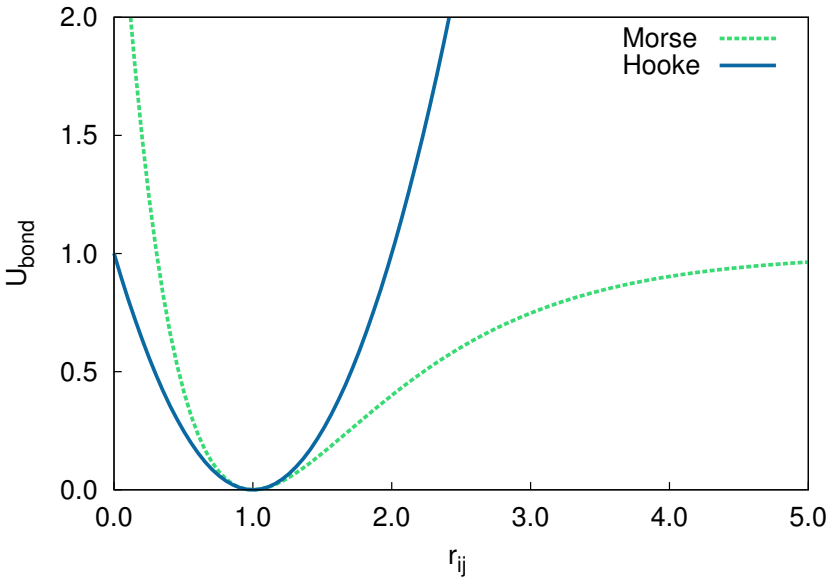

Figure 3.3: Morse potential with $D_e = 1$, $r_{eq} = 1$ and best fitting Hooke potential in the interval $r_{ij} \in [0.6, 1.4]$ ($K = 1.0003$)

Torsion angles

Torsion angles are distinguished in two brands: dihedral or proper torsion angles and improper torsion angles.

Formally, the dihedral angle (also known as a torsion angle) between four atoms i-j-k-l is defined as the angle between the planes ijk and jkl (see Figure 3.2). The angle can vary from -180 to 180 degrees, and its sign is taken as the one of the scalar product $(\mathbf{n}_{ijk} \times \mathbf{n}_{jkl}) \cdot \mathbf{r}_{jk}$, where the $\mathbf{n}$ are the normal to the planes. The standard functional form for representing the potential energy for a torsional rotation was introduced by Pitzer[26]:

$$U_{\text{dihed}} = V_\phi[1 + \cos(n\ \phi_{ijkl} - \gamma)] \tag{3.45}$$

where V_ϕ is the half energy barrier to rotation, n is the number of maxima (or minima) in one full rotation and γ determines the angular phase. Barriers for dihedral angle rotation can be attributed to the exchange interaction of electrons in adjacent bonds and to steric effects.

The Pitzer potential is often insufficient to give a full representation of the en-

ergy barriers of a dihedral angle change. Modern potential energy functions normally model the dependence of the energy on dihedral angle change by a combination of truncated Fourier series and non-bonded effects.
Improper torsions are named so because the atoms involved are not serially bonded but rather branched, and the form of the potential used is the same employed for bond angles (Equation 3.45).
Improper dihedral potentials are sometimes necessary to reproduce out-of-plane bending frequencies, i.e. to keep four atoms properly trigonal planar for a two-fold torsional potential. They are additionally used in the united-atom force field model when a carbon with an implicit hydrogen is a chiral center, thus preventing an unphysical inversion of chirality.

Nonbonded interactions

The number of valence interactions that must be calculated for a molecule is usually proportional to the number of atoms N_A. The number of nonbonded terms, however is roughly proportional to N_A^2, since they involve almost all possible pairs of atoms, except the ones bonded, directly or in 1-3, one to each other.
Despite the systematic use of cutoffs, for large systems the bulk of computational time is spent calculating the nonbonded interactions, thus great efforts have been made to optimize these calculations for vector and parallel processors.

Charges

Electrostatic interactions represent one of the most crucial issues to MD simulations of soft matter, since they are by nature long range and thus requiring interactions between all particles in the system to be considered. The most common approach to include their contribution in a simulation is to place a charge at each atomic center (nucleus). The charge can take a fraction of an

electron and can be positive or negative. Charges on adjacent atoms (joined by one or two covalent bonds) are normally made invisible to one another, since the interactions between these atoms are taken into account by the bonded interaction term.

The electrostatic attraction or repulsion between two charges is described by Coulomb's law:

$$U_{\text{charge}} = \frac{1}{4\pi\epsilon_0\epsilon_r}\frac{q_i q_j}{r_{ij}} \tag{3.46}$$

where q_i and q_j are the atoms partial charges, r_{ij} is the distance separating the atom centers, ϵ_0 is the permittivity of free space, and ϵ_r is the relative dielectric coefficient of the medium between the charges (often taken as one).

Using partial charges at nuclear centres is the crudest effective abstraction. To obtain a more accurate representation, two approaches are commonly used: the first is to add dipole, quadrupole and higher moments to the nuclear centres; the second is to introduce further non-nuclear centres. This is commonly done to represent the anisotropy in a potential caused by lone pairs on oxygen atoms[27].

In many respects, electrostatic interactions represent the biggest problem to computational studies of soft matter, as, by their nature, they are long range and dependent on the properties of the surrounding medium.

Particle Mesh Ewald

The long range nature of electrostatic interactions results in a computationally expensive $\mathcal{O}(N^2)$ problem that, if treated without any approximation, increases substantially the execution time of the simulation. This is particularly true for simulations with periodic boundary conditions, as not only interactions between particles in the central cell but also those with all the periodic images must be

computed:

$$U = \frac{1}{2} \sum_{i,j=1}^{N} \sum_{\mathbf{n}}{}' \frac{q_i q_j}{\mathbf{r}_{ij} - \mathbf{n}L} \tag{3.47}$$

Here, $\mathbf{n}$ is the lattice vector and $\sum_{\mathbf{n}}{}'$ implies that $i \neq j$ for $\mathbf{n}$ = 0. This kind of lattice sum though is well known to be a conditionally convergent sum, namely the serie can converge only if its evaluation is performed on properly rearranged terms. A workaround to this problem that allows a more efficient evaluation of coulomb interactions was developed by Ewald[28].

In the Ewald summation method, it is also assumed that the net point charges are surrounded by a diffuse charge distribution of the opposite sign that cancels out the net charge. This way, the electrostatic potential due to each particle that has not been effectively screened by the diffuse opposite charge distribution quickly decays to zero. Since we are not interested in computing the potential due to a set of screened charges but of point charges, we must correct for the fact that we added screening charge clouds with a compensating, inverse, charge distribution. This second charge distribution varies smoothly and periodically in space and can therefore be represented by rapidly converging Fourier series.

Thus, the trick in the Ewald sum is to separate the summation in two series, each converging much more rapidly than the original interaction $1/r$ one:

$$\frac{1}{r} = \frac{f(r)}{r} + \frac{1 - f(r)}{r} \tag{3.48}$$

where generally the usual choice for $f(r)$ falls on $erfc(\alpha r)$, with α being the so-called Ewald splitting parameter. The resulting expression for the potential generated by the point charges in the system can be rewritten as:

$$
\begin{aligned}
U_{Ewald} &= U^r + U^k + U^{self} + U^{surf} \\
U^r &= \frac{1}{2}\sum_{i}^{N}\sum_{j}^{N}{\sum_{\mathbf{n}}}' q_i q_j \frac{erfc(\alpha|\mathbf{r}_{ij}+\mathbf{n}L|)}{|\mathbf{r}_{ij}+\mathbf{n}L|} \\
U^k &= \frac{4\pi q_i q_j}{k^2 L^3}\sum_{\mathbf{k}} e^{i\mathbf{k}\mathbf{r}_{ij}} e^{-k^2/4\alpha^2} \\
U^{self} &= \frac{1}{L}\left[\sum_{\mathbf{n}\neq 0}\frac{erfc(\alpha\mathbf{n})}{|\mathbf{n}|} + \frac{e^{-\pi^2\mathbf{n}^2/\alpha^2}}{\pi\mathbf{n}^2} - \frac{2\alpha}{\sqrt{\pi}}\right]\sum_{i=1}^{N} q_i^2 \\
U^{surf} &= \frac{4\pi}{L^3}\left|\sum_{i=1}^{N} q_i\right|^2
\end{aligned}
\tag{3.49}
$$

While the last two terms are constant throughout the simulation, thus can be compute only once, the U^r and U^k terms depend on the interparticle separation $\mathbf{r}_{ij}$ and must be evaluated at each time step. It can be seen that the α parameter here appears explicitly and it should be chosen in way to limit the evaluation of the real term U^r to the central simulation cell. The Ewald summation method leads to a computational scaling of $\mathcal{O}(N^{3/2})$, as opposed to the $\mathcal{O}(N^2)$ of the direct sum method.

Lennard–Jones

The equilibrium distance between two proximal atomic centers is determined by a trade off between an attractive dispersion force and a core-repulsion force that reflects electrostatic repulsion.
The Lennard-Jones potential represents a successful effort in reproducing this balance with a simple expression:

$$
U_{\mathrm{LJ}} \;=\; 4\epsilon\left[\left(\frac{\sigma}{r_{ij}}\right)^{12} - \left(\frac{\sigma}{r_{ij}}\right)^{6}\right] \;=\; \frac{A}{r_{ij}}^{12} - \frac{B}{r_{ij}}^{6} \tag{3.50}
$$

where σ is the contact distance (where $U_{\mathrm{LJ}}(\sigma) = 0$) and ϵ is the well depth (where $\partial U_{\mathrm{LJ}}/\partial r_{ij} = 0$).

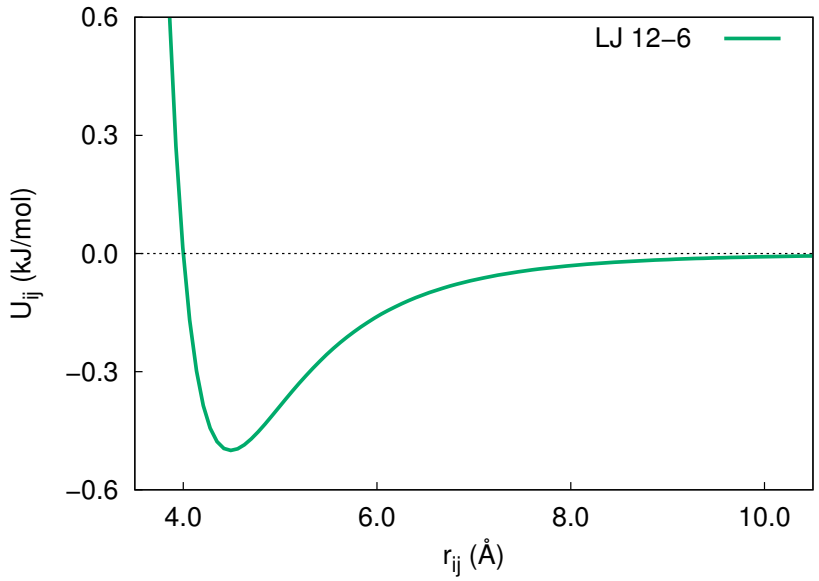

Figure 3.4: Typical LJ potential used in atomistic simulation: the practical impossibility of taking a cutoff lower than 9 Å is apparent.

The term r_{ij}^{-12} dominating at short distance, models the repulsion between atoms when they are brought very close to each other. Its physical origin is related to the Pauli principle: when the electronic clouds surrounding the atoms starts to overlap, the energy of the system increases abruptly. The exponent 12 was chosen exclusively on a practical basis, as it is particularly easy to compute, knowing the attractive term. In fact, on physical grounds an exponential behavior would be more appropriate, as represented in the Buckingham potential, used in simulations of solids:

$$U_{\text{Buckingham}} = A\exp(-Cr_{ij}) - \frac{B}{r_{ij}}^{6} \tag{3.51}$$

The term r_{ij}^{-6}, dominating at large distance, constitutes the attractive part. This is the term which gives cohesion to the system and originates from van der Waals dispersion forces arising from induced dipole-induced dipole interactions which are due to fluctuating dipoles. These are rather weak interactions, which however dominate the bonding character of closed-shell systems, that is, rare gases such as Ar or Kr, non polar solvents and also large organic molecules.
For simplicity, Lennard-Jones forces are typically modeled as effectively pair-

wise additive, and the rules to calculate the mixing parameters for couples of different atom types, are simple as well. Nonetheless, one of the major issue that limits the possibility to mix LJ parameters from different force fields originates from the different combining rules employed to compute such interactions. These rules are used to take LJ parameters σ_i and r_i for an individual atom i and combine them with the ones of an atom j in order to yield the LJ interaction for a specific atom pair ij. Unfortunately, each force field employs a different way to combine parameters. For example, CHARMM and AMBER obtain the combined σ_{ij} value via geometric mean and the r_{ij} value via arithmetic mean, while OPLS combines both parameters through geometric mean. In cases where the combining rules for two force fields are different, it is typically not recommended to transfer parameters between the two force fields, since this could lead to unexpected, non-realistic results.

For its simplicity and effectiveness, LJ is also the standard potential used for all the investigations where the focus is on fundamental issues, rather than studying the properties of a specific material.

3.4 Observables

Molecular dynamics simulations allows to determine or predict the macroscopic properties of a system through the knowledge of information at the microscopic level, such as atomic positions and velocities. In order to do so, one must find a way to relate microscopic details to macroscopic properties, and this is obtained through statistical mechanics. Statistical mechanics provides a rigorous mathematical approach that links macroscopic properties to the distribution and motion of the atoms or molecules in system.

While real experiments are usually carried out on macroscopic samples containing an extremely large number of atom or molecules, sampling over vast numbers of conformations, in statistical mechanics experimental observables are expressed in terms of ensemble averages. An ensemble average can be generically defined as:

$$\langle A \rangle = \iint d\mathbf{v}^N d\mathbf{r}^N A(\mathbf{v}^N, \mathbf{r}^N) \rho(\mathbf{v}^N, \mathbf{r}^N) \tag{3.52}$$

where $A(\mathbf{v}^N, \mathbf{r}^N)$ is the observable of interest and $\rho(\mathbf{v}^N, \mathbf{r}^N)$ is the probability density of the ensemble, both a function of the velocities $\mathbf{v}$ and positions $\mathbf{r}$. The integral in Equation 3.52 is extremely difficult to calculate for complex systems as it comprises all the possible states of a system. Therefore, while it is not feasible to evaluate Equation 3.52 through means of MD simulations, we can obtain a time average over the trajectory length of the desired observable A:

$$\langle A \rangle_{MD} = \frac{1}{M} \sum_{t=1}^{M} A(\mathbf{v}^N, \mathbf{r}^N) \tag{3.53}$$

where A is the instantaneous value of the property A, t is the simulation time and M is the number of simulated configurations. Provided that M is sufficiently large, the observable computed through molecular dynamics will be representative of the ensemble average, as stated by the ergodic hypothesis: $\langle A \rangle_{ensemble} = \langle A \rangle_{time}$.

In molecular dynamics simulations we therefore wish to generate a representative number of conformations with a reasonable amount of computer resources in order to compute observables that are comparable to their experimental counterparts. Here we present some of the most common observables employed in the liquid crystal field, which have been employed thorough this thesis to interpret the simulation results.

Characterization of molecular organization in LC systems

As previously discussed, there exist several LC phases, each characterized by a peculiar molecular arrangement. Thus it is important to define and employ a suitable set of observables allowing us to discern between one and the other and to correctly describe the order in the studied system[29,30]. Since LC phase

can feature both orientational and translational order, we need to define a general probability distribution accounting for both, and then derive special cases to inspect one or the other aspect of the molecular arrangement. In the case of an uniaxial LCs, we can approximate the molecules as uniaxial objects with orientation axis $\hat{u}$ and we assume the liquid crystal to be cylindrically symmetric around a director z, then we can expand the probability distribution of finding a molecule at a certain position z and orientation β, $\cos\beta \equiv \hat{u}\cdot\hat{z}$ i.e. $P(z,\cos\beta)$ in an orthogonal basis of Legendre polynomials P_L and of Fourier harmonics $\cos q_n z$, $q_n \equiv 2\pi n/d$, with d a layer spacing, as:[31,32]

$$P(z,\cos\beta) = \sum_{\substack{L=0\\ n=0}}^{\infty} \frac{2L+1}{2d}(1+\delta_{L0}\delta_{n0})p_{L;n}P_L(\cos\beta)\cos(q_n z), \quad L \text{ even}, \tag{3.54}$$

with the normalization

$$\int_0^d \int_{-1}^{1} P(z,\cos\beta)\; dz\; d\cos\beta = 1 \tag{3.55}$$

The positional-orientational order parameters $p_{L;n}$ are defined from the expansion coefficients of $P(z,\cos\beta)$ as:

$$p_{L;n} = \langle P_L(\cos\beta)\cos(q_n z)\rangle \tag{3.56}$$

and special cases are the purely orientational and positional order parameters $\langle P_L(\cos\beta)\rangle$ and $\langle\cos(q_n z)\rangle$. In particular, the isotropic-nematic thermotropic phase transition can be identified observing the variation with temperature of the averaged second Legendre polynomial $\langle P_2\rangle$ while the smectic-nematic one can be best appreciated evaluating the first order smectic parameter $\tau_1 = \langle\cos q_1 z\rangle$.

Orientational order

For a uniaxial phase, the probability of finding a molecule at an angle β with respect to the phase director can be expanded in an orthogonal Legendre basis, a special case of Eq. 3.54, as:

$$P(\cos\beta) = \sum_{L=0}^{\infty} \frac{2L+1}{2} \langle P_L \rangle P_L(\cos\beta),\ L \text{ even} \tag{3.57}$$

The second moment of the single molecule orientational distribution $\langle P_2 \rangle$, which is commonly used to characterize the average degree of alignment of a liquid crystal phase[31], can be calculated in a rotationally invariant way through a standard procedure for liquid crystal simulation studies[33], which requires to build and diagonalize an ordering matrix $\mathbf{Q}$, summing over all *N* molecules of the sample:

$$\mathbf{Q}(t) = \frac{1}{2N} \sum_{i=1}^{N} \left[3\hat{u}_i(t) \otimes \hat{u}_i(t) - \mathbf{I} \right], \tag{3.58}$$

where $\hat{u}_i$ is the chosen reference molecular axis and $\mathbf{I}$ is the identity matrix. The instantaneous scalar order parameter $P_2(t)$ can be obtained from the eigenvalues $\lambda_-(t), \lambda_0(t), \lambda_+(t)$, with $\lambda_-(t) < \lambda_0(t) < \lambda_+(t)$, of the $\mathbf{Q}$ matrix at time t. According to the most common convention, $P_2(t)$ corresponds to the largest eigenvalue, which is to say $P_2(t) = \lambda_+$, and once a sufficiently long equilibrium trajectory is available, its overall average $\langle P_2 \rangle$ can be calculated averaging over the production trajectory.

The orientational order of the simulated samples can be further investigated by studying the fourth rank order parameter P_4[31], which is related the fourth moment of the singlet orientational distribution and that can be calculated as follows:

$$P_4 = \frac{1}{8}(35\cos^4\beta - 30\cos^2\beta + 3), \tag{3.59}$$

Positional order

Liquid crystals often feature some degree of translational symmetry, such as in the case of smectic ones. In these phases, molecules tend to align parallel to one another and are arranged in layers, with the long axes perpendicular to the layer plane. If we consider a uniaxial phase, the probability of finding a molecule at a position z along the layer normal can be expanded in an orthogonal Fourier basis, again a special case of Eq. 3.54, as:

$$P(z) \;=\; \frac{1}{d} + \frac{2}{d}\sum_{n=1}^{\infty} \tau_n \cos(q_n z) \tag{3.60}$$

where d is the layer spacing, $q_n \equiv 2\pi n/d$, and we have assumed the origin of the laboratory frame to be such that $P(z) = P(-z)$. τ_n is the nth positional order parameter, defined as:

$$\tau_n = \int_0^d P(z)\cos(q_n z)\,\mathrm{d}z = \langle \cos(q_n z)\rangle,\; n \geq 1 \tag{3.61}$$

where $\int_0^d P(z)\,\mathrm{d}z = 1$ and z gives the position of the center of mass of each molecule along the layer normal direction z, which is here assumed to be coincident with the phase director.

Notice that here we have considered that the coordinate system origin can be chosen at will, which is fine for theoretical treatments[34–36]. However, in a computer simulation the layers and thus the origin can fluctuate over time and we shall see that an appropriate treatment that gives τ_n in a translationally invariant way is essential to properly analyze simulated data. This is very much similar to obtaining an orientational order parameter in a rotationally invariant (scalar) form, as we have done before using the eigenvalues of the **Q** (Equation 3.58) matrix. More specifically, τ_n can be calculated through two different methods, I and II. The first method is a refinement of that used by De Gaetani and Prampolini[37] and Zhang et al[38] who wrote the positional order parameters as:

$$\tau_n = \sqrt{\langle \cos(q_n z)\rangle^2 + \langle \sin(q_n z)\rangle^2} \tag{3.62}$$

while the second is based on the analysis of the translationally invariant two particle density correlation function $g(z_{12})$:

$$g(z_{12}) \;=\; 1 + 2\sum_{n=1}^{\infty} (\tau_n)^2 \cos(q_n z_{12}) \tag{3.63}$$

Regardless of the choice of method I or II detailed below, in order to correctly determine the positional order it is necessary to sample a portion of the system which can faithfully provide the probability distribution of the phase, thus having the same surface area for any value of z, and possibly containing an integer number of layers. The former condition is satisfied only for the rare case of a box where the director coincides with one of the Cartesian axes. To overcome this issue, the simulation box can be replicated in order to obtain a quasi-cubic cell. Then we can consider only the molecules enclosed in a cylinder with the long axis parallel to the director contained in the largest sphere inscribed in the replicated cell.

Method I. The instantaneous positional order parameter τ_n (Eq. 3.61) can be computed as the sample average:

$$\begin{aligned} \tau_n &= \frac{1}{N}\Big|\sum_{j=1}^{N} \exp(iq_n z)\Big| \\ &= |\langle \cos(q_n z)\rangle + i\langle \sin(q_n z)\rangle| \\ &= \sqrt{\langle \cos(q_n z)\rangle^2 + \langle \sin(q_n z)\rangle^2} \end{aligned} \tag{3.64}$$

This expression of τ_n takes into account that the density distribution does not necessarily present a maximum at $z = 0$ but, say, at a certain $z = z_0$ unknown to begin with, and possibly to change from one instant of time to another. Eq.

3.64 can be easily proved since:

$$\begin{aligned}\langle\cos(q_n z)\rangle &= \int_a^{a+d} P(z+z_0)\cos(q_n z)\,\mathrm{d}z \\ &= \tau_n \cos(q_n z_0) \qquad (3.65)\\ \langle\sin(q_n z)\rangle &= \int_a^{a+d} P(z+z_0)\sin(q_n z)\,\mathrm{d}z \\ &= -\tau_n \sin(q_n z_0) \qquad (3.66)\end{aligned}$$

for an arbitrary a, suggesting that for each snapshot the instantaneous phase factor can be estimated as:

$$q_n z_0 = \frac{1}{n}\mathrm{atan2}\left(\frac{\langle\cos(q_n z)\rangle}{\tau_n}, \frac{\langle\sin(q_n z)\rangle}{\tau_n}\right) \qquad (3.67)$$

where atan2(y,x) returns the angle between the x-axis and the vector from the origin to (x, y) in the correct quadrant[39], e.g., for positive arguments atan2(y, x)≡atan(y/x). We can then further average the instantaneous τ_n over the trajectory to obtain the time average value.

While apparently simple, the evaluation of τ_n is not straightforward, since the instantaneous value of the layer spacing d is obviously not known beforehand. To overcome this issue, for each configuration we first evaluate $\langle\cos(2\pi/d')\rangle$ and $\langle\sin(2\pi/d')\rangle$ in terms of an arbitrary tentative layer spacing d', and then scan d' and, using Eq. 3.64, we obtain a plot of $\tau_m(d')$. We can then select the value of d' that maximizes $\tau_m(d')$ as the instantaneous layer spacing of the sample (see Fig. 3.5). In order to justify such procedure, and also to evaluate the presence of errors resulting from the finite size of the sample box, we derive analytical expressions for $\langle\cos(2m\pi/d')\rangle$ and $\langle\sin(2m\pi/d')\rangle$.

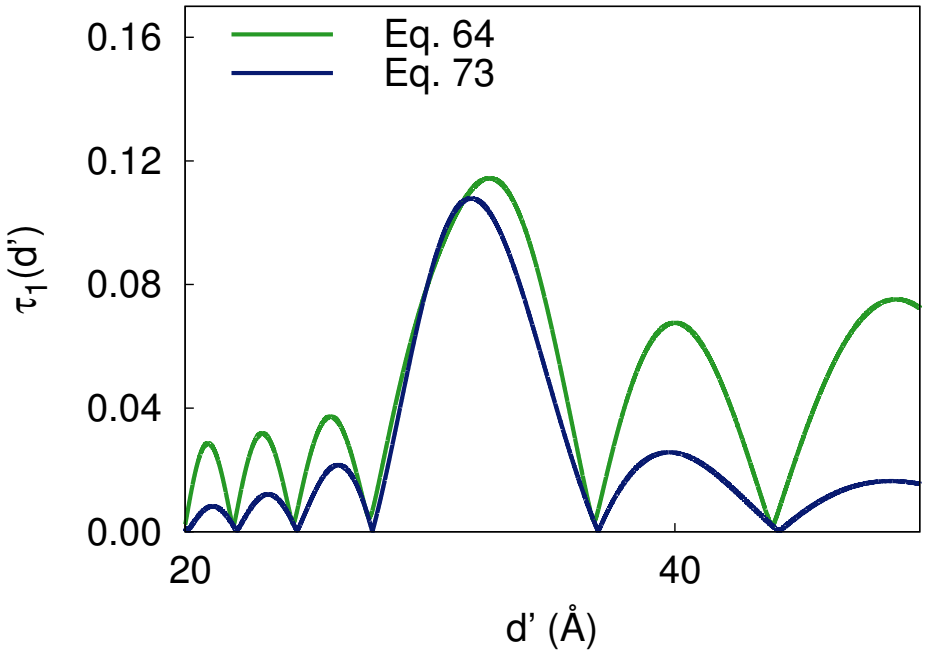

Figure 3.5: $\tau_1(d')$ as a function of the trial layer spacing d' for method I with $\tau_1 = 0.11, d = 31.6$ Å, $L = 110$ Å and $z_0 = 14$ Å , with (blue lines, Eq. 3.73) and without (green lines, Eq. 3.64) removal of the spurious factor.

$$
\begin{aligned}
\langle \cos(\frac{2m\pi z}{d'}) \rangle &= \int_a^b \left[\frac{1}{L} + \sum_m \frac{2\tau_n}{L} \cos\left(q_n(z+z_0)\right) \right] \cos(\frac{2\pi m z}{d'}) dz \\
&= \frac{1}{q'_m L} \sin(q'_m z) \Big|_a^b \\
&+ \sum_{n=1} \frac{\tau_n}{L} \left[\frac{1}{A} \sin(Az + q_n z_0) \right] \Big|_a^b \\
&+ \sum_{n=1} \frac{\tau_n}{L} \left[\frac{1}{B} \sin(Bz + q_n z_0) \right] \Big|_a^b \qquad (3.68) \\
\langle \sin(\frac{2m\pi z}{d'}) \rangle &= -\frac{1}{q'_m L} \cos(q'_m z) \Big|_a^b \\
&- \sum_{n=1} \frac{\tau_n}{L} \left[\frac{1}{A} \cos(Az + q_n z_0) \right] \Big|_a^b \\
&+ \sum_{n=1} \frac{\tau_n}{L} \left[\frac{1}{B} \cos(Bz + q_n z_0) \right] \Big|_a^b \qquad (3.69)
\end{aligned}
$$

with:

$$A = \frac{2\pi(nd' + md)}{dd'}, B = \frac{2\pi(nd' - md)}{dd'} \tag{3.70}$$

where $q'_m = 2\pi m/d'$ and the cell length $L = b - a$, with a and b being the generic cell boundaries.

It can be seen that both $\langle\cos(2m\pi/d')\rangle$ and $\langle\sin(2m\pi/d')\rangle$ are the sum of three terms. The first arises solely from the finite size of the cell and tends to zero for L tending to infinity. The second term is a function of τ_n but does not show a maximum for integer m and is negligible even at fairly small values of L. The third term is the one responsible for the peaks visible in the plot of $\tau_m(d')$, corresponding to τ_n. This can be demonstrated by evaluating the limit for $\delta \equiv md' - nd$ tending to zero:

$$\lim_{\delta\to 0}\langle\cos(\frac{2\pi mz}{d'})\rangle \quad = \quad \tau_n \cos(q_n z_0) \tag{3.71}$$

$$\lim_{\delta\to 0}\langle\sin(\frac{2\pi mz}{d'})\rangle \quad = \quad -\tau_n \sin(q_n z_0) \tag{3.72}$$

This shows that $\tau_m(d')$ has multiple peaks if the phase presents higher order terms of positional order. In particular, $n \neq m$ peaks will appear to the left and right of the one corresponding to the mth order parameter respectively. In practice it is convenient to subtract the first term of Eq. 3.68 and 3.69 before computing $\tau_n(d')$ since, especially when *L* is low and not a multiple of d, it can mask the peak corresponding to τ_n. In Fig. 3.5 the effect of the spurious terms can be observed qualitatively, and it can be seen to affect both the height and the position of the peak. Additionally, Eqs. 3.68 and 3.69 suggest that the sharpness of the peaks corresponding to τ_n depends essentially on the length of the sampling region, as L appears in the argument of the cosine and sine functions, increasing the frequency of their oscillations.

When computing the positional order parameters from the simulations, it is convenient to consider a virtual cylindrical region going from $-L$ to $+L$. This simplifies the expression for the positional order parameter (Equations 3.68 and 3.69), that can be calculated as:

$$\tau_n(d') = \left\{ \left[\langle \cos(\frac{2n\pi}{d'} z) \rangle - \frac{d'}{2\pi n L} \sin(\frac{2\pi n L}{d'} z) \right]^2 + \langle \sin(\frac{2n\pi}{d'} z) \rangle^2 \right\}^{1/2} \quad (3.73)$$

It is worth noting that the choice of the computational approach used to obtain the averages positional order parameters can influence the estimate of the positional order of a smectic sample. In their works, Prampolini et al.[37] and Zhang et al.[38] determined τ_1 by summing the instantaneous $\tau_1(d')$ plots and taking the maximum value of the resulting averaged plot as τ_1. However, this approach may lead to artificially low values of τ_1. In fact, the instantaneous value of the layer spacing, d', is not constant during the simulation, thus the peaks of $\tau_m(d')$ of different configurations do not superimpose anymore, resulting in lower values of τ_1. To avoid this problem, here we computed τ_1 as the average of the maximum values of the instantaneous $\tau_1(d')$ plot.

This method to evaluate the positional order has the advantage of being computationally inexpensive, since it scales with $O(N)$. Additionally, the evaluation of $\tau(d)$ can be exploited also to compute the average probability density distributions. Since liquid crystal phases are fluid systems and thus the maxima of the density distribution tends to shift during the simulation, we can exploit the phase factor calculated from Eq. 3.67 to re-phase the instantaneous probability distribution and obtain the average one.

Method II. A second way to estimate the positional order exploits the two particle correlation function $P(z_{12})$, which can be obtained as:

$$P(z_{12}) = \int_0^d P(z_1) \cdot P(z_1 - z_{12})\,\mathrm{d}z_1 = \frac{1}{d} + \frac{2}{d}\sum_{n=1}^{\infty}(\tau_n)^2 \cos(q_n z_{12}) \quad (3.74)$$

with $z_{12} = z_1 - z_2$ being the projection of the intermolecular distance on the layer normal.

In the simplest case[36,40], the normalized correlation function along the layer normal (Fig. 4.8) can be truncated to the first term in the Fourier expansion as:

$$g(z_{12}) \approx 1 + 2\tau_1^2 \cos(q_1 z_{12}), \quad (3.75)$$

The values of τ_1 and d can then be extrapolated by least square fitting the $g(z_{12})$ profiles with Eq. 3.75[41].

The correlation function method has three main advantages: i) it is independent on any phase factor and on the length of the sampling region L, always featuring a maxima at $z_{12} = 0$, ii) it increases the signal to noise ratio, allowing for a more accurate fit, iii) it allows to obtain directly both τ_n and the layer spacing d. On the other hand, it scales with $O(N^2)$ and thus is much slower than method I. Hence its use is recommended only for small samples, where the noise is high and the sampling region is inevitably small.

Pair distributions

An additional way of characterizing the molecular organization of a fluid material is through pair distributions. The simplest is the radial distribution function $g_0(r)$:

$$g_0(r) = \frac{1}{4\pi r^2 \rho_N}\langle\delta(r - r_{ij})\rangle_{ij}, \quad (3.76)$$

where $\rho_N \equiv N/V$ is the number density of the sample, $\mathbf{r}_{ij}$ is the vector connecting the chosen reference centers of the i and j molecules.

For anisotropic systems it is also important to introduce the set of probability distributions of finding two molecules i, j at a certain distance and relative orientation from each other, $G_L(r)$, defined as

$$G_L^u(r) \quad = \quad \langle \delta(r - r_{ij}) P_L(\hat{u}_i \cdot \hat{u}_j) \rangle_{ij} / \langle \delta(r - r_{ij}) \rangle_{ij} \tag{3.77}$$

where $\hat{u}_i, \hat{u}_j$ are convenient unit vectors fixed on molecules i, j and P_L is a Legendre polynomial of order L. In the uniaxial model $\hat{u}$ would just be the rod axis. In an atomistic simulation the choice of the reference centers and of the vector $\hat{u}$ is not univocal and actually in some cases it might be convenient to introduce more than one to give a more complete description.

Dielectric constant

In the most common case, in atomistic computer simulations the charge distribution is described as a collection of atomic point charges, while its polarizability is partially neglected and partially included in the Lennard–Jones potential. As a consequence, the polarizability term in the classical expression for the calculation of the dielectric constant[42] becomes ill defined and difficult to evaluate, and it is usually dropped, at least in the computations for water (see e.g.[43]). The most important term are hence the instantaneous molecular dipoles (expressed in e/Å units):

$$\vec{\mu_j} \quad = \quad \sum_{i=1}^{N_{atoms}} q_i \vec{\mathbf{r}}_i \ , \tag{3.78}$$

which are summed up to give the total dipole moment:

$$\vec{\mathbf{M}} \quad = \quad \sum_{j=1}^{N_{mols}} \vec{\mu}_j \ . \tag{3.79}$$

Considering smooth Particle Mesh Ewald[44] as a good approximation of Ewald method, the fluctuation formula for “conducting” or “tin foil” boundary condi-

tions[45] should hold (cgs units)[46]:

$$\epsilon = 1 + \frac{4\pi}{3}\frac{\langle M^2\rangle}{Vk_BT} \tag{3.80}$$

where with the angular parentheses is meant an ensemble average; passing to SI units we obtain:

$$\epsilon = 1 + \frac{1}{3\epsilon_0}\frac{\langle M^2\rangle}{Vk_BT}\ . \tag{3.81}$$

As in the simulations the average total dipole moment may be non zero, the equilibrium fluctuation of M is better described by the formula for the variance of a gaussian distribution:

$$\sigma^2_{\mathbf{M}} = \langle M^2\rangle - \langle M\rangle^2 \tag{3.82}$$

Introducing the symbol $\kappa = \frac{1}{3\epsilon_0 Vk_BT}$ and recasting in tensorial form:

$$\boldsymbol{\epsilon} = 1 + \kappa(\langle\vec{\mathbf{M}}\otimes\vec{\mathbf{M}}\rangle - \langle\vec{\mathbf{M}}\rangle\otimes\langle\vec{\mathbf{M}}\rangle) \tag{3.83}$$

$$\epsilon = \frac{1}{3}\mathrm{Tr}(\boldsymbol{\epsilon}) \tag{3.84}$$

In principle, in the director frame $\boldsymbol{\epsilon}$ should be diagonal; in practice, due to director fluctuations, it is not possible to define a director frame for the whole simulation. Therefore, we suggest to compute $\vec{\mathbf{M}}$ in the director frames R in each configuration i and to calculate the dielectric constant after the diagonalization of the $\boldsymbol{\epsilon}$ matrix):

$$\boldsymbol{\epsilon}^{dir} = 1 + \kappa(\langle R\vec{\mathbf{M}}\otimes R\vec{\mathbf{M}}\rangle - \langle R\vec{\mathbf{M}}\rangle\otimes\langle R\vec{\mathbf{M}}\rangle) \tag{3.85}$$

Each eigenvalue of $\boldsymbol{\epsilon}^{dir}$ then should provide the value of the dielectric constant

in the corresponding direction (eigenvector).

$$\boldsymbol{\epsilon}^{dir}\mathbf{x} = \boldsymbol{\Lambda}\mathbf{x} \tag{3.86}$$

$$\epsilon = \frac{1}{3}\mathrm{Tr}(\boldsymbol{\Lambda}) = \mathrm{Tr}\begin{bmatrix} \epsilon_x/3 & 0 & 0 \\ 0 & \epsilon_y/3 & 0 \\ 0 & 0 & \epsilon_z/3 \end{bmatrix} \tag{3.87}$$

Again, this does not necessarily hold in a simulation, $\boldsymbol{\epsilon}^{dir}$ is not diagonal and consequently its eigenvectors do not coincide with the director frame. As we are interested in the dielectric tensor components in the director frame, the diagonalization may not be the best choice. In addition, as for an uniaxial phase the x and y axes of the director frame fluctuate randomly, it is very unlikely to obtain $\epsilon_x = \epsilon_y$, and $\epsilon_\perp$ must be calculated as the average of the two values.
In simulations at constant pressure, V is not a constant, and we must average $\vec{\mathbf{M}}/V$ instead of $\vec{\mathbf{M}}$:

$$\boldsymbol{\epsilon}^{dir} = 1 + \frac{\langle V\rangle}{3\epsilon_0 k_B T}\left[\langle R\vec{\mathbf{M}}/V \otimes R\vec{\mathbf{M}}/V\rangle - \langle R\vec{\mathbf{M}}/V\rangle \otimes \langle R\vec{\mathbf{M}}/V\rangle\right] . \tag{3.88}$$

The fluctuations of $\mathbf{M}$ and in particular of its sign, which are fundamental in the correct evaluation of the term $\vec{\mathbf{M}} \otimes \vec{\mathbf{M}}$ (in principle it should average to zero), are bound to the first rank orientational correlation functions of the molecular axes ϕ^1_{00} and ϕ^1_{10}. These functions are known to decay very slowly for liquid crystals, therefore it is very difficult in a normal–length simulation (let say 10 nanoseconds) to evaluate correctly the above mentioned term. It is probably better to use a more pragmatic approach, neglecting the average of $\vec{\mathbf{M}}$:

$$\boldsymbol{\epsilon}^{dir} = 1 + \frac{\langle V\rangle}{3\epsilon_0 k_B T}\left[\langle R\vec{\mathbf{M}}/V \otimes R\vec{\mathbf{M}}/V\rangle\right] . \tag{3.89}$$

Translational diffusion

There are mainly two common ways to obtain a self-diffusion coefficient from molecular dynamics simulations. One is from the molecular positions (Einstein relation[47]) and the other from their velocities (Green-Kubo relations[48,49]). Theoretically, one should obtain the same result from both methods. In practice, obtaining the self-diffusivity D from the velocities $\mathbf{r}$ requires to integrate the velocity autocorrelation function:

$$D = \frac{1}{3}\int_0^\infty \langle \mathbf{v}(t) \cdot \mathbf{v}(0) \rangle dt \tag{3.90}$$

However, the evaluation of this integral can cause numerical problems for long trajectories. From this perspective, a more reliable alternative is to compute the diffusion coefficient from the molecular coordinates $\mathbf{r}$ through the Einstein relation:

$$D_{ii} = \lim_{t\to\infty} \frac{\langle (r_i(t_0+t) - r_i(t_0))^2 \rangle}{2t}, \tag{3.91}$$

where r_i is the component of the molecular position vector of each molecule along the axis $i = x, y, z$ of the director frame. The numerator of the equation is the mean square displacement (MSD) and angular brackets indicate the average over the all molecules and over all origins, meaning that any timestep can be considered as the t_0. This allows for a collection of a better statistic and thus less noise in the square displacement diagram. In practice, in order to compute the diffusion coefficient, one has to build the MSD plot as a function of time. The MSD(t) function can can then be fitted by linear least square regression and the obtained slope corresponds to the diffusion coefficient by a factor of $2d$, where d is the dimensionality of the system.

Bibliography

[1] D. A. Case, T. E. Cheatham, T. Darden, H. Gohlke, R. Luo, K. M. Merz, A. Onufriev, C. Simmerling, B. Wang, and R. J. Woods, “The AMBER biomolecular simulation programs,” *J. Comput. Chem.*, vol. 26, no. 16, pp. 1668–1688, 2005.

[2] B. R. Brooks, C. L. Brooks, A. D. Mackerell, L. Nilsson, R. J. Petrella, B. Roux, Y. Won, G. Archontis, C. Bartels, S. Boresch, and et al., “CHARMM: The biomolecular simulation program,” *J. Comput. Chem.*, vol. 30, no. 10, pp. 1545–1614, 2009.

[3] J. C. Phillips, R. Braun, W. Wang, J. Gumbart, E. Tajkhorshid, E. Villa, C. Chipot, R. D. Skeel, L. Kalé, and K. Schulten, “Scalable molecular dynamics with NAMD,” *J. Comput. Chem.*, vol. 26, no. 16, pp. 1781–1802, 2005.

[4] D. Van Der Spoel, E. Lindahl, B. Hess, G. Groenhof, A. E. Mark, and H. J. C. Berendsen, “GROMACS: Fast, flexible, and free,” *J. Comput. Chem.*, vol. 26, no. 16, pp. 1701–1718, 2005.

[5] S. Plimpton, “Fast parallel algorithms for short-range molecular dynamics,” *J. Comput. Phys.*, vol. 117, no. 1, pp. 1–19, 1995.

[6] J. E. Jones, “On the determination of molecular fields. ii. from the equation of state of a gas,” *Proc. R. Soc. Lond. A*, vol. 106, no. 738, pp. 463–477, 1924.

[7] L. Verlet, “Computer "experiments" on classical fluids. i. thermodynamical properties of lennard-jones molecules,” *Phys. Rev.*, vol. 159, pp. 98–103, Jul 1967.

[8] L. Verlet, “Computer "experiments" on classical fluids. ii. equilibrium correlation functions,” *Phys. Rev.*, vol. 165, pp. 201–214, Jan 1968.

[9] W. C. Swope, H. C. Andersen, P. H. Berens, and K. R. Wilson, “A computer simulation method for the calculation of equilibrium constants for the formation of physical clusters of molecules: Application to small water clusters,” *J. Chem. Phys.*, vol. 76, no. 1, 1982.

[10] H. J. C. Berendsen, J. P. M. Postma, W. F. v. Gunsteren, A. DiNola, and J. R. Haak, “Molecular dynamics with coupling to an external bath,” *J. Chem. Phys.*, vol. 81, no. 8, pp. 3684–3690, 1984.

[11] H. C. Andersen, “Molecular dynamics simulations at constant pressure and/or temperature,” *J. Chem. Phys.*, vol. 72, no. 4, pp. 2384–2393, 1980.

[12] S. Nosé, “A unified formulation of the constant temperature molecular dynamics methods,” *J. Chem. Phys.*, vol. 81, no. 1, pp. 511–519, 1984.

[13] W. G. Hoover, “Canonical dynamics: Equilibrium phase-space distributions,” *Phys. Rev. A*, vol. 31, no. 3, pp. 1695–1697, 1985.

[14] P. Procacci and M. Marchi, “Taming the Ewald sum in molecular dynamics simulations of solvated proteins via a multiple time step algorithm,” *J. Chem. Phys.*, vol. 104, no. 8, pp. 3003–3012, 1996.

[15] M. P. Allen and D. J. Tildesley, *Computer Simulation of Liquids*. Walton Street, Oxford OX2 6DP: Oxford University Press, 1989.

[16] P. Corp., “Parameter and topology files for CHARMM, version 22,” Copyright 1986, Release 1992.

[17] W. F. van Gunsteren and H. J. C. Berendsen, *Groningen Molecular Simulation (GROMOS) Library Manual*. Biomos, Groningen, 1987.

[18] J. Wang, P. Cieplak, and P. A. Kollman, “How well does a restrained electrostatic potential (RESP) model perform in calculating conformational energies of organic and biological molecules?,” *J. Comput. Chem.*, vol. 21, p. 1049, 2000.

[19] W. L. Jorgensen and N. A. McDonald, “Development of an all-atom force field for heterocycles. properties of liquid pyridine and diazenes,” *Theochem - J. Mol. Struct.*, vol. 424, p. 145, 1998.

[20] A. K. Rappè, C. J. Casewit, K. S. Colwell, W. A. Goddard, and W. M. Skiff, “UFF, a full periodic table force field for molecular mechanics and molecular dynamics simulations,” *J. Am. Chem. Soc.*, vol. 114, pp. 10024–10035, 1992.

[21] N. L. Allinger, Y. H. Yuh, and J. Lii, “Molecular mechanics. the MM3 force field for hydrocarbons. 1,” *J. Am. Chem. Soc.*, vol. 111, p. 8551, 1989.

[22] S. K. Nath and R. Khare, “New forcefield parameters for branched hydrocarbons,” *J. Chem. Phys.*, vol. 115, p. 10837, 2001.

[23] H. Sun, “Compass: an ab initio force field optimized for condensed-phase applications overview with details on alkane and benzene compounds,” *J. Phys. Chem. B.*, vol. 102, pp. 7338–7364, 1998.

[24] A. C. T. van Duin, S. Dasgupta, F. Lorant, and W. A. Goddard III, “ReaxFF: A reactive force field for hydrocarbons,” *J. Phys. Chem. A*, vol. 105, p. 9396, 2001.

[25] A. D. Mackerell, “Empirical force fields for biological macromolecules: Overview and issues,” *J. Comput. Chem.*, vol. 25, pp. 1584–1604, 2004.

[26] K. Pitzer *Disc. Faraday Soc.*, vol. 107, pp. 4519–4529, 1951.

[27] P. Cieplak, W. D. Cornell, C. Bayly, and P. A. Kollmann, “Application of the multimolecule and multiconformational RESP methodology to biopolymers: Charge derivation for DNA, RNA, and proteins,” *J. Comput. Chem.*, vol. 16, pp. 1357–1377, 1995.

[28] P. P. Ewald, “Die berechnung optischer und elektrostatischer gitterpotentiale,” *Annalen der Physik*, vol. 369, no. 3, pp. 253–287, 1921.

[29] C. Zannoni, “Order parameters and orientational distributions in liquid crystals,” in *Polarized Spectroscopy of Ordered Systems*, pp. 57–83, Springer, 1988.

[30] C. Zannoni, “On the description of ordering in liquid crystals,” in *The Molecular Dynamics of Liquid Crystals*, pp. 11–40, Springer, 1994.

[31] C. Zannoni, “Distribution function and order parameters,” in *The Molecular Physics of Liquid Crystals* (G. Luckhurst and G. Gray, eds.), p. 51, Academic Press, London, 1979.

[32] P. Wojtowicz, “Introduction to the molecular theory of smectic-A liquid crystals,” in *Introduction to Liquid Crystals* (E. Priestley and S. P. Wojtowicz, P.J., eds.), p. 83, Plenum Press, 1975.

[33] D. Frenkel and B. Smit, *Understanding Molecular Simulations: From Algorithms to Applications.* Accademic Press, San Diego, 1996.

[34] G. Kventsel, G. Luckhurst, and H. Zewdie, “A molecular field theory of smectic A liquid crystals - a simpler alternative to the McMillan theory,” *Mol. Phys.*, vol. 56, p. 589, 1985.

[35] W. L. McMillan, “Simple molecular model for the smectic A phase of liquid crystals,” *Phys. Rev. A*, vol. 4, p. 1238, 1971.

[36] W. L. McMillan, “X-ray scattering from liquid crystals. i. cholesteryl nonanoate and myristate,” *Phys. Rev. A*, vol. 6, p. 936, 1972.

[37] L. D. Gaetani and G. Prampolini, “Computational study through atomistic potentials of a partial bilayer liquid crystal: structure and dynamics,” *Soft Matter*, vol. 5, pp. 3517–3526, 2009.

[38] J. Zhang, J. Su, and H. Guo, “An atomistic simulation for 4-cyano-4’-pentylbiphenyl and its homologue with a reoptimized force field,” *J. Phys. Chem. B*, vol. 115, pp. 2214–27, 2011.

[39] *http://en.wikipedia.org/wiki/Atan2*.

[40] R. G. Marguta, E. M. del Río, and E. de Miguel, "Revisiting McMillan's theory of the smectic A phase," *J. Phys.: Condens. Matter*, vol. 18, p. 10335, 2006.

[41] *Note that in[50,51], the values of τ_1 reported were obtained by fitting the autocorrelation function with Eq- 3.60, so they are really $(\tau_1)^2$.*

[42] J. G. Kirkwood, "The dielectric polarization of polar liquids," *J. Chem. Phys.*, vol. 7, p. 911, 1939.

[43] Y. Guissani and B. Guillot, "A computer simulation study of the liquid–vapor coexistence curve of water," *J. Chem. Phys.*, vol. 98, p. 8221, 1993.

[44] U. Essmann, L. Perera, M. L. Berkowitz, T. A. Darden, H. Lee, and L. G. Pedersen, "A smooth particle mesh Ewald method," *J. Chem. Phys.*, vol. 101, p. 8577, 1995.

[45] M. Neumann, "Dipole moment fluctuation formulas in computer simulations of polar systems," *Mol. Phys.*, vol. 50, p. 841, 1983.

[46] M. Neumann, "Computer simulation and the dielectric constant at finite wavelength," *Mol. Phys.*, vol. 57, p. 97, 1986.

[47] A. Einstein, "Über die von der molekularkinetischen theorie der wärme geforderte bewegung von in ruhenden flüssigkeiten suspendierten teilchen," *Annalen der Physik*, vol. 322, no. 8, pp. 549–560, 1905.

[48] M. S. Green, "Markov random processes and the statistical mechanics of time dependent phenomena. ii. irreversible processes in fluids," *J. Chem. Phys.*, vol. 22, no. 3, 1954.

[49] R. Kubo, "Statistical-mechanical theory of irreversible processes. i. general theory and simple applications to magnetic and conduction problems," *J. Phys. Soc. Jpn.*, vol. 12, no. 6, pp. 570–586, 1957.

[50] T. A. Papadopoulos, L. Muccioli, S. Athanasopoulos, A. B. Walker, C. Zannoni, and D. Beljonne, "Does supramolecular ordering influence exciton transport in conjugated systems? insight from atomistic simulations," *Chem. Sci.*, vol. 2, pp. 1025–1032, 2011.

[51] A. Pizzirusso, M. Savini, L. Muccioli, and C. Zannoni, "An atomistic simulation of the liquid-crystalline phases of sexithiophene," *J. Mater. Chem.*, vol. 21, pp. 125–133, 2011.

Chapter 4

An atomistic description of the nematic and smectic phases of 4-n-octyl-4‘cyanobiphenyl (8CB)

This chapter is an extract from the article “An atomistic description of the nematic and smectic phases of 4-n-octyl-4‘cyanobiphenyl (8CB)” published in J. Chem. Phys. 2013 May 28, vol. 138, issue 20, pag. 204901.

4.1 Introduction

Atomistic simulations have recently started to offer a view with an unprecedented level of detail on the molecular organization and dynamics of condensed matter, and of liquid crystals (LC) in particular, allowing us to inspect for the first time the role of specific molecular features like internal flexibility and charge distributions on the phase behavior[1–6].

Compared with generic models, like the Gay-Berne one[7,8], where each mesogen molecule is replaced by a single rigid object, the atomistic level of description grants access to the chemical details needed to quantitatively predict or at least interpret the results of X-ray diffraction, nuclear magnetic resonance (NMR) and other real experiments. For instance, several papers published

in the last few years have proved that “in silico” nematics like cinnamates[1] and cyanobiphenyls[5,9,10] can reproduce a large number of experimental results such as transition temperatures, density, order parameters, NMR dipolar couplings, and can help to interpret the origin of phenomena like the odd-even effect, i.e. the alternation in nematic-isotropic (NI) transition temperatures determined by the variation of the number of aliphatic carbon atoms in the homologous series of these LC compounds.

It is also worth pointing out that atomistic simulations have a significant predictive potential: for example, simulated values of the fourth rank orientational order parameter $\langle P_4 \rangle$ computed for 4-n-pentyl-4′-cyanobiphenyl were at variance with experimental ones available at the time of publication[11] obtained from depolarized Raman scattering, but have more recently proved to be in good agreement with those obtained using an improved version of the same technique[12]. It should also be pointed out that it is quite common to find a relatively large scattering amongst measurements of structural and dynamic data published by different groups, even when the same characterization technique is nominally used, and that simulations can thus represent also a useful complement to experiment. In another context the advantages of combining experiments and predictive simulations have also been recently shown for NMR studies of solutes dissolved in nematics[13,14].

While the quality of observable results obtained from molecular dynamics (MD) is approaching that of real experiments for nematics, much less is known on the possibility of reliably reproducing smectic molecular organizations and properties. From this point of view, 4-n-octyl-4′-cyanobiphenyl (8CB) is an ideal test bench system since it has been the subject of numerous experimental investigations and of one of the first atomistic studies a few years ago[15]. Even though such early simulations were started assuming molecules already placed in layers and their trajectories were followed for a time of a few nanoseconds, shorter than the expected rotational relaxation time for a molecule of the size of 8CB, more recently several groups have reported simulation results for the 8CB bulk phase[16–19]. McDonald and Hanna[16], employing a united atom (UA)

level of modeling, where CH, CH_2 and CH_3 groups are considered as suitably parametrized spherical interaction sites, successfully obtained a smectic phase from the isotropic, even if, probably because of the choice of neglecting electrostatic interactions, they did not reproduce neither the transition temperatures (e.g. they obtained $T_{NI} > 400$ K) nor the dimerization of 8CB molecules and thus the layer spacing observed through X-Ray measurements[20–22]. Prampolini and coworkers[17], employing a mixed UA – all atoms model, found instead the spontaneous onset of a partial bilayer smectic phase in a temperature range compatible with the experimental one, although the layer spacing was still rather far from the one obtained by X-ray measurements[20–22] and the limited number of simulations did not allow to precisely assess the transition temperatures. The simulation of cyanobiphenyls, particularly 5CB and 8CB has also been tackled by Zhang et al.[18], with good estimated results for the transition temperatures, using a Force Field (FF) obtained modifying the TraPPE-UA set[23] so as to reproduce the bulk density for 5CB within 2%.

Another recent work by Chami et al.[24] reported the simulation of Electron Paramagnetic Resonance (EPR) spectra of a cholestane nitroxide spin probe dissolved in 8CB starting from all atom MD simulations (thus explicitly including the hydrogens using AMBER parameters). While the simulated EPR spectra closely resemble the experimental ones, the transition temperatures ($T_{NI} \approx 375$ K, $T_{SN} \approx 340 - 360$ K) are still far from the experimental values ($T_{NI}^{exp} \approx 313.8$ K,$T_{SN}^{exp} \approx 306.5$ K)[25]. Moreover, even though the onset of a partial bilayer smectic phase was observed both visually and from the calculation of the radial distribution function parallel to the director, $g_(z)$, no estimation of the positional order parameter was reported[24].

Here, we take advantage of the united atoms force field we have recently developed and validated for the nematic phase of cyanobiphenyls[10] to investigate in detail 8CB in its nematic and smectic phase. One of the significant issues we plan to examine is the type and extent of antiparallel arrangement for these molecules with a strong terminal dipole[26], comparing with X-ray data. Another is the determination of positional and, for the first time, of the mixed positional-

orientational order parameters, testing to what extent the two types of ordering can be considered independent as sometimes assumed in theoretical mean field models.[27] The third is to look at translational dynamics, and in particular to the diffusion coefficients for movements inside the layers and across, examining to what extent the UA approximation can affect a successful comparison with experimental studies.

4.2 Methods and Computational Details

We have run two series of simulations, the first one on systems with a number of molecules $N = 750$ at several temperatures, and the second one on a much larger system with $N = 3000$ to obtain a more in-depth assessment of the positional order of the smectic phase and to study its dependence on the system size.

The 8CB molecules were modelled at UA level of detail using a AMBER-OPLS force field[28,29], which was previously tuned in-house to reproduce the experimental nematic-isotropic transition temperature of n-alkyl cyanobiphenyls with 5 to 8 carbon atoms in the linear alkyl chain[10] but that was not explicitly optimized for the smectic phase.

For the first series of simulations, we followed a previously established procedure[6,10,30]: we started from a temperature at which the sample is isotropic and then we progressively cooled it at lower temperatures, allowing to observe, if occurring, its spontaneous organization. Simulations were run in NPT conditions using NAMD[31] with multiple step integration: bonded, van der Waals and electrostatic interactions were calculated every 2, 4 and 8 fs respectively. The samples were kept at the constant pressure of 1 atm using a Berendsen barostat[32], while the temperature, which ranged from 300 to 320 K, was kept constant through velocity rescaling.

To validate the computational assessment of the positional order, we have also run a second series of simulations and investigated three different N=3000 molecules systems. One is a bulk sample at 300 K obtained by merging two

previously equilibrated free standing 8CB thin films and removing the vacuum, obtaining a sample containing approximately 10 layers. This system was then brought to 310 K in order to investigate the gradual disappearance of the smectic order. We also studied a system obtained by merging 4 replicas of an isotropic system from the previous serie of simulations and cooling it down to 300 K. The samples were kept at the constant pressure of 1 atm using a Langevin piston, allowing us to run simulations with the x and y axis of the cell kept at a constant ratio, thus maintaining a square section of the cell. Three dimensional periodic boundary conditions were used in both two series of simulations and long range electrostatic interactions were computed through the Particle Mesh Ewald method[33].

The average simulation runtime for each sample was about 150 ns long, a time much larger than the expected rotational and translational correlation decay times. It is worth noting that for N = 750 molecules samples at temperatures close to a phase transition, we prolonged the production time up to 400 ns, as far as we know, the longest ever used in MD liquid crystal studies at the time of the publication.

4.3 Results and discussion

The liquid crystalline phase diagram of 8CB presents a nematic and a smectic mesophase in a very narrow temperature range (about 7 K), thus making its reproduction by means of MD simulations a challenging task. More specifically, the experimental smectic-nematic and nematic-isotropic transition temperatures (T_{SmN} and T_{NI}), which will be represented as vertical dashed lines in the following figures, are located at 306.6 and 313.6 K respectively, thus a precision of about 1 K on the simulated results is required.

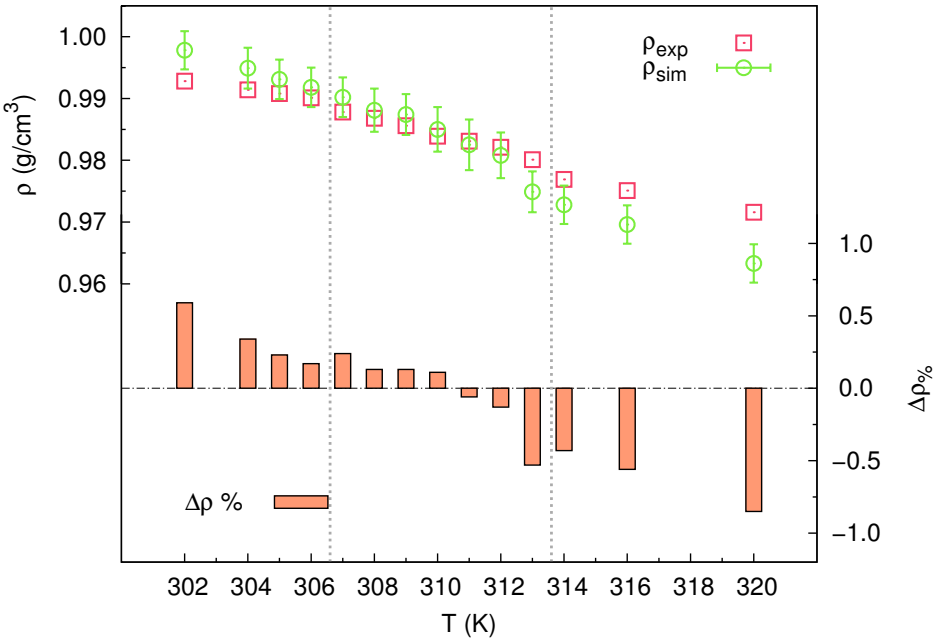

Figure 4.1: Comparison between experimental[34] and simulated density as a function of temperature. $\Delta\rho_{\%}$ is the percent deviation of the simulated density from the experimental value. Vertical dashed lines represent the experimental transition temperatures T_{SmN} and T_{NI}.

Density

A first validation of our results for the N = 750 system can be found comparing density values obtained by our simulations with the experimental ones available in literature[34] (Fig. 4.1).

The simulated density decreases with increasing temperature, reproducing precisely the experimental trend, like already shown in reference[10] for smaller samples composed of 250 molecules. Still in Fig. 4.1, it can be noticed that the most accurate results are obtained in proximity of the experimental T_{NI}, with a deviation from the experiment not greater than 0.1%. Moving away from the transition region, this discrepancy increases to 1%, though these results still qualify as fairly accurate.

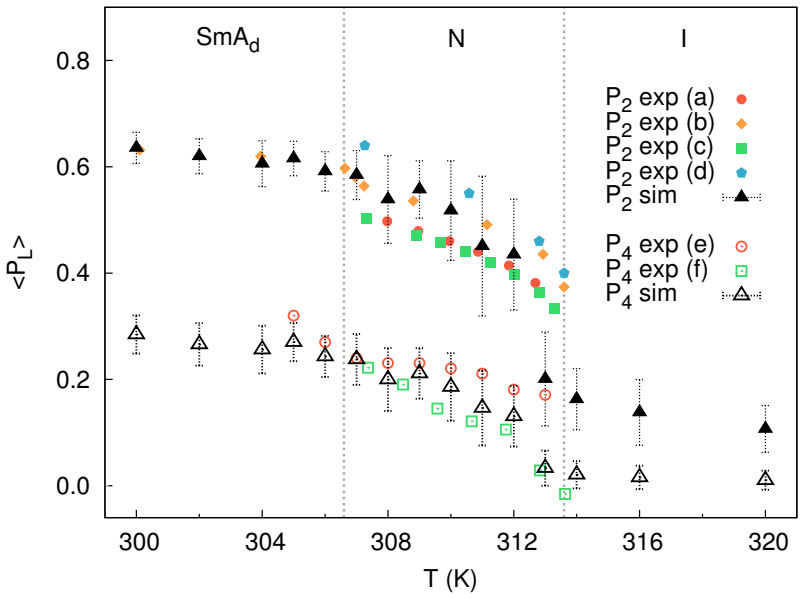

Figure 4.2: Orientational order parameters $\langle P_2 \rangle$ and $\langle P_4 \rangle$ of the simulated sample compared to different sets of experimental data as a function of temperature. Data from refractive index measurements in references[35–37] (a-c) and from polarised Raman spectroscopy measurements in references[11,38] (d-f).

Orientational order

In Figure 4.2 we report the orientational order parameter $\langle P_2 \rangle$ of the simulated samples as a function of temperature. It can be seen that at high temperatures the sample possesses a very low value of $\langle P_2 \rangle$, ranging from 0.1 to 0.2. Between 313 and 312 K we observe a steep rise of the order parameter, suggesting the spontaneous onset of a nematic phase. After the isotropic-nematic transition, $\langle P_2 \rangle$ increases from 0.4 to slightly less than 0.6 as we move toward the nematic-smectic transition.

Still in Fig. 4.2, the results obtained by our simulations can be compared with different sets of experimental data, in particular with birefringence and Raman depolarization spectroscopy measurements[11,35–37]. We notice that our simulated data are in good agreement with the average of the various, rather scattered experimental data sets.

The NI transition is characterized by considerable fluctuations of $\langle P_2 \rangle$, with a standard deviation comparable to the value of the order parameter itself (cf. the error bars in Fig. 4.2). This is due to the presence of order-disorder fluctuations

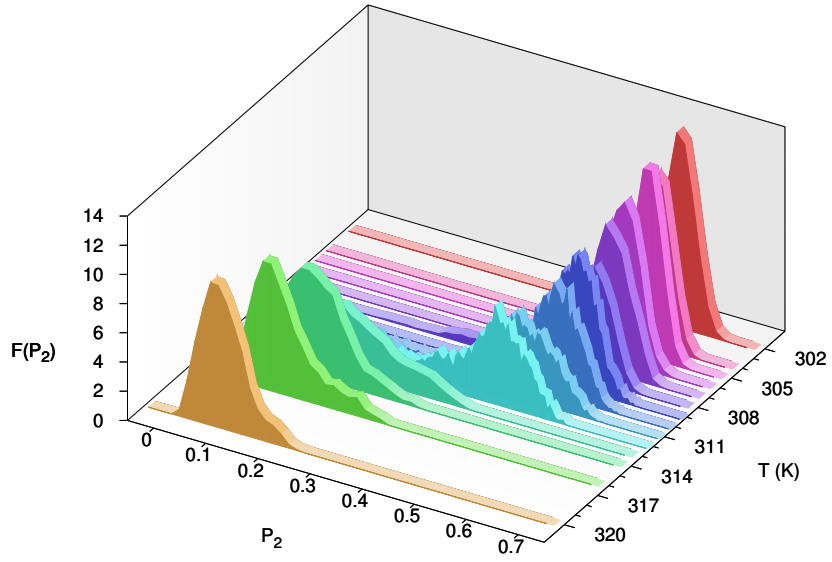

Figure 4.3: Distribution histograms of the instantaneous values of P_2 at different temperatures.

during the time evolution of the sample and is consistent with the weak first order nature of the NI transition. We arbitrarily choose to consider a phase as definitely "ordered" when it shows a $\langle P_2 \rangle$ greater than 0.3, hence locating T_{NI} between 312 and 313 K. This assumption can be verified by plotting histograms of the $\langle P_2 \rangle$ distribution at each temperature[19,39] (Fig. 4.3), allowing to easily spot the temperature at which the NI transition takes place. For temperatures above 313 K, it can be noticed how every sample possesses a broad distribution of $\langle P_2 \rangle$, with a peak close to 0, highlighting how most of the configurations in those samples possess isotropic $\langle P_2 \rangle$ values. On the other hand, below 312 K the peaks are sharper and shifted toward high values of the order parameter, as a consequence of the onset of ordered liquid crystalline phases such as the nematic and smectic ones. The sudden inversion of the population of molecules possessing high or low $\langle P_2 \rangle$ values taking place between 313 and 312 K confirms our estimate of the transition temperature, which is closer to the experimental value[40] of 313.6 K with respect to our previous simulation results of 317 K obtained on samples of 250 molecules[10]. This also indicates the importance of the sample size, which must be sufficiently large in order

to accurately locate phase transitions. Below 308 K, the order parameter is almost constant with temperature and its fluctuations become much smaller, thus presenting sharper distributions.
The value of $\langle P_4 \rangle$ at each temperature is compared in Fig. 4.2 with experimental data from Raman depolarization measurements[38]: it can be seen that the experimental trend is again well reproduced by simulations. Moreover, the profile of the fourth rank order parameter follows closely the one observed for $\langle P_2 \rangle$, dropping to zero above 312 K and thus confirming our previous estimate of the transition temperature.

Pair correlations

We start showing in Fig. 4.4 the radial distribution, $g_0(r)$, calculated here considering the center of charge of each molecule as the reference point (Fig.4.5). Fig. 4.4 shows the radial distributions of the smectic, nematic and isotropic phases as a function of intermolecular separation r. It can be seen that each phase has a liquid-like distribution, characterized by the absence of peaks in the long range region and tending to its asymptotic value of 1 for r greater than 30 Å. In the short range region though, each phase shows three distinct peaks, indicating the presence of local coordination shells. In particular, the first peak located at about 5 Å suggests the presence of quasi dimeric associations (as shown in Fig. 4.5) both in the isotropic and anisotropic phases, a common feature for systems composed of molecules bearing a strong terminal polar group. When the temperature is raised, the short range structure becomes less definite as shown by the radial distribution of the isotropic sample at 316 K.
Since we are particularly interested in the dipole organization we have then evaluated the first and second rank positional-orientational distribution $G_L(r)$ choosing as reference vectors $\hat{u}_I, \hat{u}_J$ the electric dipole unit vectors $\hat{\mu}_I, \hat{\mu}_J$ in order to obtain the first and second rank distributions $G_1^{\mu}(r)$ and $G_2^{\mu}(r)$:

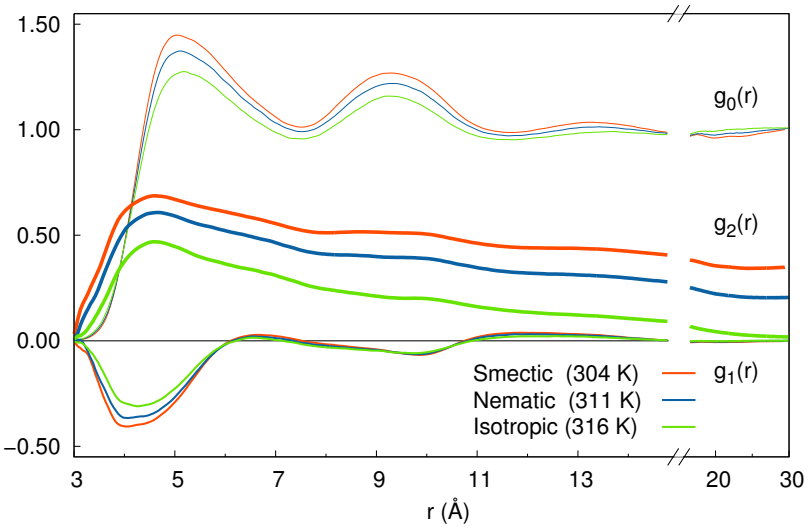

Figure 4.4: Variation of the 8CB dipole orientational correlation functions $g_1(r)$, $g_2(r)$ and of the radial distribution of centers of charge, $g_0(r)$ for samples at 304, 311 and 316 K (representing the smectic, nematic and isotropic phases, respectively).

$$G_1^{\mu}(r) = \langle \delta(r - r_{ij})(\hat{\mu}_i \cdot \hat{\mu}_j) \rangle_{ij} / \langle \delta(r - r_{ij}) \rangle_{ij} \tag{4.1}$$

$$G_2^{\mu}(r) = \langle \delta(r - r_{ij}) \left[\frac{3}{2}(\hat{\mu}_i \cdot \hat{\mu}_j)^2 - \frac{1}{2} \right] \rangle_{ij} / \langle \delta(r - r_{ij}) \rangle_{ij} \tag{4.2}$$

where r_{ij} is now the distance between the charge centres of the i and j molecules.

In particular, the $G_1^{\mu}(r)$ function shown in Fig. 4.4 allows to clarify the local structure around each 8CB molecule. In the short separation region, a negative value for $G_1^{\mu}(r)$ is expected, since the first neighbouring molecules are oriented in an antiparallel fashion, thus yielding a negative average of $\hat{\mu}_i \cdot \hat{\mu}_j$. At a slightly greater distance, a change of sign of $G_1^{\mu}(r)$ is observed, as molecules belonging to the next coordination shell are in turn antiparallel to the ones in the first shell (thus parallel to the reference molecule). Between 8 and 14 Å, we

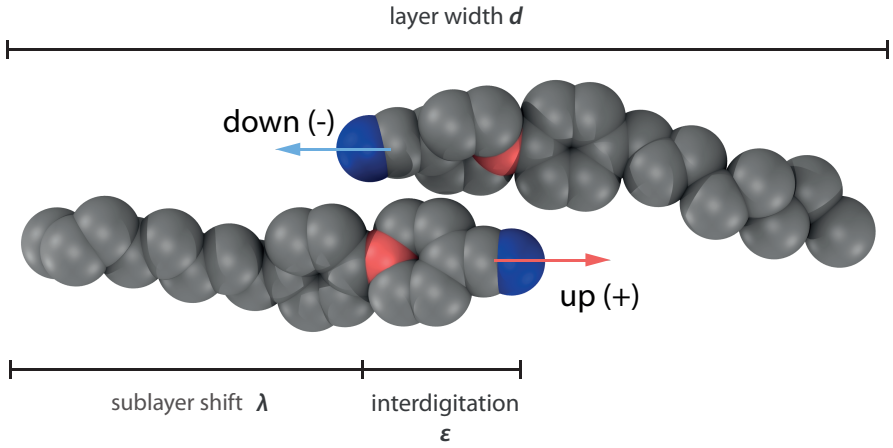

Figure 4.5: The typical positional and orientational arrangement of neighbouring molecules belonging to two different sublayers in the SmA_d phase. d is the layer spacing and $\varepsilon = d - 2\lambda$ is the interdigitation. The center of charge, which turns out to be pretty conformation independent, is located on the red colored carbon atom.

observe the same trend as described for the first and second neighbours, but less pronounced since the influence of the reference molecule gets weaker as the distance increases. For long separations, the value of $G_L(r)$ tends to the limit of the square of the order parameter of rank *L*, $\langle P_L \rangle^2$ as shown in[39,41]. Accordingly $G_1(r)$ tends asymptotically to 0 as the interaction with the reference molecular dipole becomes negligible, therefore leading to a random head-tail orientation of most distant molecules.

The $G_2(r)$ function corresponds to evaluating the relative order parameter P_2 of a molecule with respect to the orientation of a reference molecule as a function of their intermolecular distance. Fig. 4.4 shows the presence of a peak in the region $r \leq 5$ Å, corresponding to the short range orientational order arising from the packing interactions, in analogy with the behavior even found isotropic fluids[9,26,42]. At greater distances, in our case for $r > 30$ Å, $G_2(r)$ decreases and tends asymptotically to $\langle P_2 \rangle^2$, the square of the order parameter of the phase[39].

Smectic order parameter

It is well known that 8CB presents a smectic phase below 306.6 K[40]. To asses the validity of the force field developed in[10] also for these layered phases, we must determine whether the simulated sample is able to reproduce both the smectic-nematic transition temperature and properties such as the positional order parameter and layer spacing. It must be specified that in order to comply with the standard nomenclature found in literature for X-ray investigations of smectic phases, in this chapter bilayers are referred to as “layers” and monolayers to as “sublayers”.

To characterize the smectic phase of the simulated systems, it is important to correctly evaluate the positional organization to compare it with available experimental data. As of now, there is no standard method in literature to assess the positional order of smectic phases, thus we exploited 8CB simulated samples as a test bench to define a reliable protocol. Since we wish to assess the robustness of our results we have also studied, in addition to the N = 750 molecules sample at 300 K (which we will call system **a** from now on), three other larger bulk systems: **b**) N = 3000 at 300 K obtained starting from a free standing thin film, **c**) N = 3000 at 300 K obtained from an isotropic bulk sample and **d**) N = 3000 at 310K obtained by heating a replicated sample of **a**.

These additional systems allow us to investigate the effect of the sample size and preparation on the positional order and in particular, to consider the thermal history of the sample, i.e. how it was equilibrated before the onset of the smectic phase. This could be important also when trying to compare simulated properties to observed ones, since samples of smectics that present a nematic are usually experimentally prepared by cooling down a nematic sample which was previously aligned with an external field.

Going back to the description of positional order, we recall that for a uniaxial phase the probability of finding a molecule at a position z along the layer normal can be expanded in an orthogonal Fourier basis as:

$$P(z) \;=\; \frac{1}{d} + \frac{2}{d}\sum_{n=1}^{\infty} \tau_n \cos(q_n z) \tag{4.3}$$

where d is the layer spacing, $q_n \equiv 2\pi n/d$ and we have assumed the origin of the laboratory frame to be such that $P(z) = P(-z)$. As already reported in Chapter 3, τ_n is the nth positional order parameter, defined as:

$$\tau_n = \int_0^d P(z)\cos(q_n z)\,\mathrm{d}z = \langle \cos(q_n z)\rangle,\; n \geq 1 \tag{4.4}$$

where $\int_0^d P(z)\,\mathrm{d}z = 1$ and z gives the position of the center of mass of each molecule along the layer normal direction z, which is here assumed to be coincident with the phase director. This is appropriate for a smectic A and for our case as the smectic phase of 8CB is not found to be tilted either experimentally or in our simulations. As already described in Chapter 3, τ_n can be calculated with two different methods, I and II. We recall that The first method, a refinement of that used by De Gaetani and Prampolini[17] and Zhang et al[18], writes the positional order parameters as:

$$\tau_n = \sqrt{\langle \cos(q_n z)\rangle^2 + \langle \sin(q_n z)\rangle^2} \tag{4.5}$$

while the second method is based on the two particle density correlation function $g(z_{12})$:

$$g(z_{12}) \;=\; 1 + 2\sum_{n=1}^{\infty} (\tau_n)^2 \cos(q_n z_{12}) \tag{4.6}$$

In Table 4.1 we report the values of the main translational order parameter τ_1 for systems **a**, **b**, **c** and **d** obtained with the two methods. It can be seen that the *N*=750 molecules system **a** presents a lower τ_1 compared to the larger ones, while the smectic order in systems **b** and **c** is almost the same. The

influence of the history, size and shape of the sample on the layer spacing can be seen in Table 4.1, where we also report the time average of d for each system. System **b** features the value of d closest to the experimental ones of $d = 31.4$[22]-31.7 [43] Å, whilst in system **c** the layer spacing is lower. In system **a** we find a slightly higher value of d, together with an order of magnitude higher uncertainty, probably due to the low number of layers.

In Fig. 4.6 it can be seen that, in agreement with the results obtained from Method I, System **b** presents slightly higher layer spacing when compared to system **c**, once again highlighting the effect of the sample equilibration prior to the onset of the smectic phase. It can also be seen that system **a** features lower density oscillations and a higher value for the layer spacing. A flat $g(z_{12})$ trend can be observed for system **d**, suggesting the absence of positional order for the molecular centers of mass in the nematic sample at 310 K.

Comparing our results to those from other groups, we notice that the works from De Gaetani and Prampolini[17] and Zhang et al.[18] report a considerable discrepancy between the values of τ_1 calculated for small ($N < 1000$) and large ($N > 1000$) samples, while in our case the positional order parameter remains approximately the same regardless of the sample size (Table 4.2). This highlights that the correction we propose in Appendix A, which takes into account the effect of the finite size of the system and the choice of the sampling region, is important for a correct evaluation of the positional order parameter.

For samples with $N > 1000$, we see that our results are in agreement with the ones from the two other groups. For these large systems, the corrections we proposed play indeed a small role since the size of the sample reduces the influence of the spurious term discussed in Appendix A and it can be assumed that the layer normals in references[17,18] were close to one of the box axes. It must be noted that for both small and large systems, the value of the interlayer spacing d for our simulations is the closest to the experimental values[22,43]. while the value of τ_1 for all the large simulations is significantly lower than the experimental ones[44,45].

We can now exploit the positional order parameter obtained to discuss the on-

Table 4.1: Simulated values with respect to the temperature of: positional order parameter and layer spacing from $\tau_1(\delta)$ (Method I), positional order parameters from $g(z_{12})$ fit (Method II): τ_1 and $\tau_{1,\pm}$, interlayer distance d, shift between *up* and *down* sublayers λ, sublayer interdigitation ε

Sample	T (K)	N	$(\tau_1)_I$	d (Å)	$(\tau_1)_{II}$	$(\tau_1^{\pm})_{II}$	d_{gz} (Å)	λ (Å)	ε (Å)	d_{exp}[21]
a	300	750	0.13 ± 0.03	32 ± 1	0.12	0.28	32.3	14.4	3.6	31.2
b	300	3000	0.15 ± 0.01	31.3 ± 0.1	0.15	0.35	31.2	13.8	3.6	31.2
c	300	3000	0.15 ± 0.02	30.4 ± 0.2	0.14	0.33	30.4	13.5	3.4	31.2
d	310	3000	0.04 ± 0.01	26 ± 9	-	-	-	-	-	
	302	750	0.13 ± 0.02	32 ± 2	0.10	0.24	31.8	14.0	3.8	31.2
	304	750	0.12 ± 0.04	32 ± 2	0.10	0.23	32.3	14.2	4.0	31.2
	305	750	0.15 ± 0.03	32.5 ± 0.4	0.13	0.29	32.5	14.3	4.0	31.2
	306	750	0.13 ± 0.03	32.5 ± 0.9	0.11	0.25	32.6	14.3	3.9	
	307	750	0.12 ± 0.04	32 ± 1	0.11	0.24	32.6	14.3	4.0	
	308	750	0.10 ± 0.04	32 ± 2	0.07	0.16	31.9	14.1	3.7	
	309	750	0.10 ± 0.02	32 ± 2	0.07	0.17	31.8	14.0	3.7	
	310	750	0.08 ± 0.03	31 ± 3	0.07	0.16	31.9	14.1	3.7	
	311	750	0.04 ± 0.01	28 ± 5	0.05	0.11	31.6	14.0	3.5	

Table 4.2: Comparison of the positional order parameter τ_1, the layer spacing d and second rank orientational order parameter $\langle P_2 \rangle$ from the most recent computational and experimental work available in literature. All atom, core and *N* atoms refer to computations run on all atoms, on the phenyl core and on the nitrogen atom only respectively.

	N	*T* (K)	τ_1	d (Å)	$\langle P_2 \rangle$
This work (method I)	750	300	0.13 (all atom) 0.25 (core)	32	0.62
De Gaetani, Prampolini[17]	192	300	0.21 (all atom)	27	0.57
De Gaetani, Prampolini[17]	768	300	0.21 (all atom)	26	0.66
Zhang et al.[18]	256	300	0.21 (N atoms)	28	0.45
This work (method I)	3000	300	0.15 (all atom) 0.3 (core)	31.3	0.64
De Gaetani, Prampolini[17]	1536	300	0.14 (all atom)	27÷ 28	0.68
Zhang et al.[18]	1024	300	0.32 (N atoms)	28.5	0.49
Alexander et al.[44](neutron scattering)		293÷305	0.46 ÷ 0.57	31.5	
Kapernaum, Giesselmann[45](X rays)		292-309.5	0.64 ÷ 0.74		

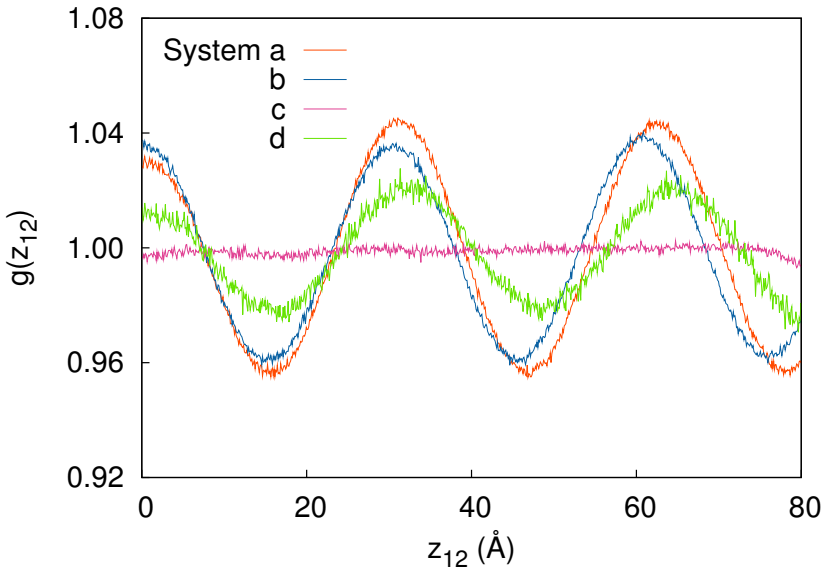

Figure 4.6: Pair density correlation function along the director $g(z_{12})$ for systems **a**, **b**, **c** and **d**.

set of the smectic phase, which experimentally occurs below 306.6 K[40] for 8CB. In Fig. 4.7 the $g(z_{12})$ functions for N = 750 samples at different temperatures are reported. At low temperatures the profile exhibits a clear sinusoidal trend, due to the presence of smectic layers. This behavior progressively disappears for samples at temperatures above 307 K. The trend is consistent with the one obtained for the values of τ_1 computed from method I and II (Table 4.1), which is gradually decreasing above 307 K and becomes negligible at 311 K. This result is in good agreement with the experimental smectic-nematic transition temperature of 306.6 K. It must be noted that in N = 750 sample, quite large smectic fluctuations are still present up to 311 K (Fig. 4.7 and Table 4.1) while for the N = 3000 sample we find a truly nematic phase already at 310 K (Fig. 4.6 and Table 4.1). This observation suggests that small size systems may favour positionally ordered phases above the smectic-nematic transition temperature. In any case, the presence of smectic fluctuations in the nematic temperature range is not surprising, as it has been already observed experimentally in several works[43–47]. Since no evident discontinuity for τ_1 is present while heating the sample, a second order nature for the smectic-nematic transition can be assumed.

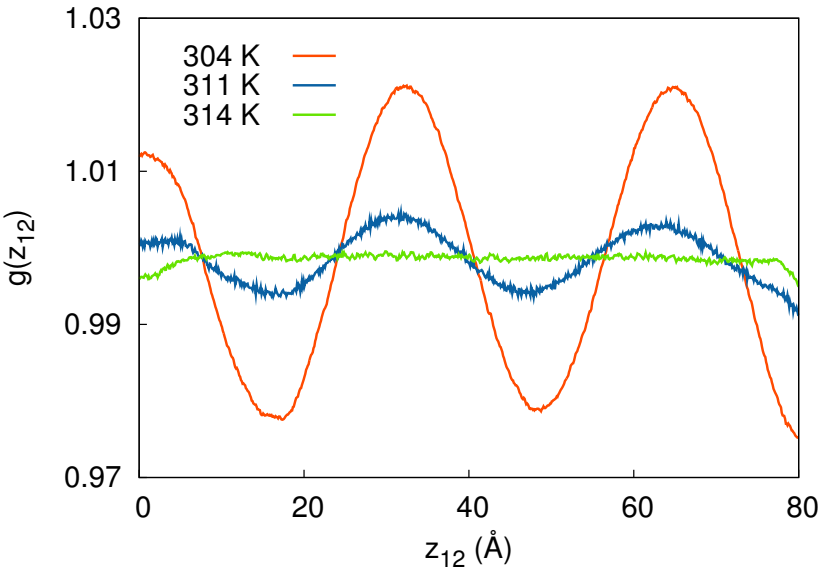

Figure 4.7: Density correlation $g(z_{12})$ along the z axis for samples at 304, 311 and 316 K (representing the smectic, nematic and isotropic phases, respectively).

Regarding the interlayer distance, we can observe that below 307 K the simulated samples feature a d of about 32 Å (Table 4.1), which is closer to the experimental value[43] of 31.7Å with respect to previous simulation studies[16–18]. Besides, the interlayer distance obtained from simulations remains constant in the temperature range of the smectic phase, in agreement with the trend observed through X-rays measurements for 8CB by Urban and coworkers[21] and, recently for other smectics[46].

Smectic A_d interdigitation

The smectic phase of 8CB, which belongs to the so-called SmA_d[48] category, is characterized by the presence of bilayers formed by two interdigitated sublayers of molecules oriented in opposite directions in order to optimize the interaction between the polar groups. In particular, 8CB bilayers are commonly described as $partial$, since the distance d between bilayers is lower than twice the molecular length l (about 1.4 times the length of one molecule for 8CB), differently from smectic types composed by single layers, where d is about as large as

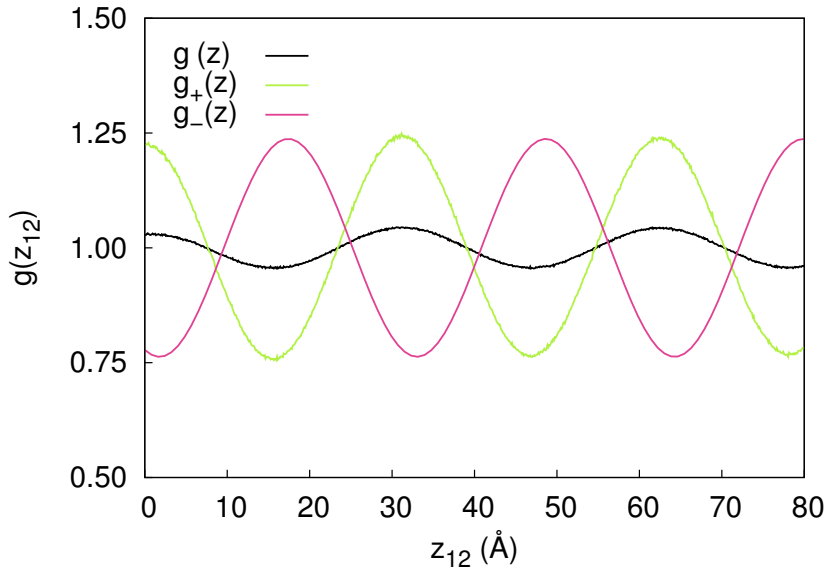

Figure 4.8: Comparison of *up* and *down* two particle correlation function $g_{\pm}(z_{12})$ with the one of the whole sample $g(z_{12})$ for system **a**. Here $g_{-}(z_{12})$ is a best fit function to the actual one which has been shifted of λ so that it yields the total $g(z_{12})$ when combined with $g_{+}(z_{12})$ (see Eq. 4.7).

l[48]. For a matter of convenience, we refer to molecules forming the sublayers either as *up(+)* or *down(-)* molecules, depending on whether their dipole moment is parallel or antiparallel to the arbitrarily chosen direction of the layer normal. The snapshot in Fig. 4.9 highlights the interdigitation between *up* and *down* (red and blue) molecules forming the bilayer of the simulated sample. We refer to the positional order parameter of the up or down pair correlation functions $g_{\pm}(z_{12})$ as $\tau_1^{\pm}$. Values of $\tau_1^{\pm}$ calculated by fitting the distribution profiles with the two particle correlation function (Eq. 3.75) are reported in Table 4.1. As shown in Fig. 4.8, both $g_{+}(z_{12})$ and $g_{-}(z_{12})$ present the same trend, but they are shifted by a phase factor $q_1\lambda$. Once the values of λ and d have been determined, the bilayer interdigitation ε can be estimated (see the geometric representation of these parameters in Fig. 4.5).

The total pair correlation function $g(z_{12})$ is then given by the superposition of the *up* and *down* waves, provided they are suitably shifted of $q_1\lambda$:

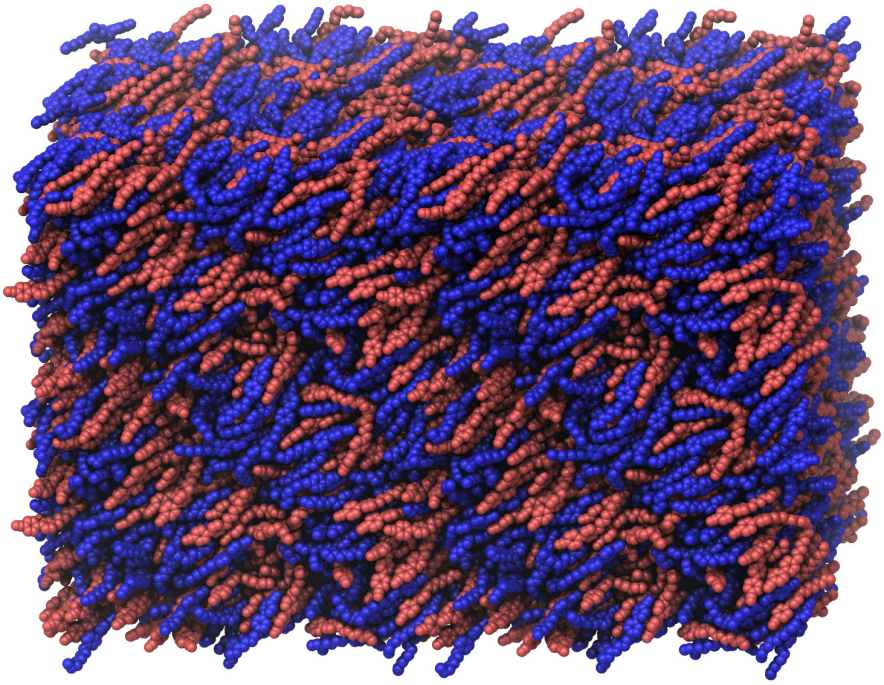

Figure 4.9: Layer interdigitation in system **c** (replicated twice along x, y and z axes). Red and blue colors represent parallel ("up") and antiparallel ("down") molecules.

$$\begin{aligned} g(z_{12}) &= \frac{1}{2}[g_+(z_{12}) + g_-(z_{12}+\lambda)] \\ &\approx 1 + (\tau_1^{\pm})^2\{\cos[q_1(z_{12}-\frac{\lambda}{2})] + \cos[q_1(z_{12}+\frac{\lambda}{2})]\}, \end{aligned} \tag{4.7}$$

Eq. 4.7 reproduces the pair correlation function of the whole sample (Fig. 4.8) which possesses a maximum located at $z_{12} = 0$. We then fitted $g_{\pm}(z_{12})$ with Eq. 3.75 obtaining the value of $\tau_1^{\pm}$, which was then used as a parameter in Eq. 4.7 to fit the total pair correlation function[49], obtaining the values of d, λ and hence the interdigitation ε, reported in Table 4.1. It can be seen that $\tau_1^{\pm}$ is roughly twice τ_1 and that its temperature trend closely follows the one of τ_1. In addition, it must be noted that not only the layer spacing d but also the interdigitation length ε (Fig.4.5) are rather constant with the temperature.

Table 4.3: Mixed order parameters $p_{L;n}$ compared to the products of the average order parameters $\langle P_L \rangle \tau_n$. The positional term τ_n and and the layer spacing d were computed according to procedure described in Appendix A (method I).

Sample	T (K)	N	$p_{2;1}$	$\langle P_2 \rangle \tau_1$	$p_{4;1}$	$\langle P_4 \rangle \tau_1$
a	300	750	0.13 ± 0.04	0.08 ± 0.02	0.08 ± 0.03	0.03 ± 0.01
b	300	3000	0.16 ± 0.01	0.09 ± 0.01	0.09 ± 0.01	0.041 ± 0.005
c	300	3000	0.15 ± 0.02	0.09 ± 0.01	0.08 ± 0.01	0.039 ± 0.006
d	310	3000	0.04 ± 0.02	0.017 ± 0.004	0.015 ± 0.008	0.004 ± 0.001
	302	750	0.14 ± 0.03	0.08 ± 0.02	0.08 ± 0.03	0.03 ± 0.01
	304	750	0.13 ± 0.05	0.07 ± 0.02	0.07 ± 0.03	0.03 ± 0.01
	305	750	0.16 ± 0.03	0.09 ± 0.02	0.09 ± 0.02	0.04 ± 0.01
	306	750	0.14 ± 0.03	0.08 ± 0.02	0.08 ± 0.02	0.03 ± 0.01
	307	750	0.13 ± 0.04	0.07 ± 0.02	0.07 ± 0.03	0.03 ± 0.01
	308	750	0.11 ± 0.04	0.06 ± 0.02	0.06 ± 0.04	0.02 ± 0.01
	309	750	0.10 ± 0.03	0.06 ± 0.02	0.05 ± 0.02	0.02 ± 0.01
	310	750	0.08 ± 0.03	0.04 ± 0.02	0.04 ± 0.02	0.012 ± 0.008
	311	750	0.03 ± 0.01	0.006 ± 0.002	0.014 ± 0.008	0.0007 ± 0.0009

Mixed order parameters

Although we have discussed orientational and positional order separately, it is clear that they can, at least in principle, be correlated. Even though various simulations of 8CB have appeared, we are not aware of the mixed orientational positional parameters $p_{L;n}$ introduced in Eq. 3.56, with $L > 0, n > 0$ being determined. Here we wish to provide such an evaluation and use it to test a simple approximation of the mixed parameters as product of the positional and orientational orders[27].

It is worth recalling that in the first molecular field theory of smectic A liquid crystals proposed by McMillan[50], which succeeded in qualitatively reproducing the features of smectic A phases, the internal energy of a single molecule was expressed in terms of the orientational and mixed positional-orientational order parameters and only afterwards, the theory was modified[51] with the introduction of a pure positional order parameter. The averaged internal energy of a single molecule for the coupled model was written by McMillan as:

$$U = -u_0 \left[\langle P_2 \rangle^2 + \alpha (p_{2;1})^2 + \gamma (\tau_1)^2 \right] /2 \tag{4.8}$$

where u_0, αu_0 and γu_0 are the strengths of the orientational, mixed and positional contributions, respectively. Kventsel et al.[27] proposed an alternative simplified theory for smectic A phases, where the mixed order parameter term $p_{2;1}$ was replaced by the product of the positional and orientational order parameter $\langle P_2 \rangle \tau_1$. This decoupled model has the advantage of making the numerical solution of the mean field problem much easier.

Thanks to computer simulations, we can now test if the approximations proposed in the theories were acceptable. In particular, here we can test whether the decoupled model for smectic A phases can describe also the interdigitated smectic A_d phase. In Table 4.3 we report the values of $p_{L;n}$ =$\langle P_L \cos(q_n z) \rangle$ (see Eq.3.56) (with $n = 1$ and $L = 2, 4$) for the system with *N* = 3000 and *N* = 750 molecules. It can be seen that for 8CB the orientational and positional order

are actually correlated, with the average of the product $p_{L;n}$ being roughly twice the product of the averages $\langle P_L \rangle \tau_n$. For comparison, we run the same calculation on smectic samples of α-sexithienyl (T6) obtained from a recent work of Pizzirusso et al.[4], revealing that for that system the positional and orientational order parameters are completely decoupled. These results suggest that the approximation of $p_{L;n} = \langle P_L \rangle \tau_n$ which has been used in the Kventsel et al. model[27] may not apply to 8CB smectic A$_d$ phase, while it seems to be suitable for simple smectic A phases such as the one of T6. This result points out once again to the important role of simulations, since mixed order parameters are not currently available from experimental measurements.

Comparison with experimental positional order

There are very few experimental determinations of positional order, indeed only perhaps a dozen or so, which is surprising considering the hundreds of papers highlighting the interest for smectics. Fortunately 8CB is one of the most studied cases. A first work was that of Leadbetter[52], which proposed a procedure for obtaining τ_1 from the first reflection peak in a macroscopically unoriented smectic polydomain. More recently, Kapernaum and Giesselmann[45] using X-ray found $\tau_1 = 0.64 \div 0.74$ in the interval T = 309.5-292 K, while Alexander et al.[44] using neutron scattering reported a value of τ_1 =0.46-0.57 in the region T= 293-305 K. The simulated results for the positional order appear significantly smaller than those obtained from the experimental ones. It is thus worth to examine more in detail some possible sources for this discrepancy and in particular how the positional order is extracted from scattering experiments.
We start writing the differential elastically scattered cross section per molecule as a sum taken over all the atomic centres and the intensity at scattering vector $\mathbf{q}$ will be proportional to the square of this total wave:

$$I(\mathbf{q}) = \left\langle \left| \sum_{i=1}^{N} \sum_{a \in i} A_{a,i}(\mathbf{q}) \right|^2 \right\rangle / N \tag{4.9}$$

$$= k \sum_{i,j=1}^{N} \sum_{\substack{a,b=1 \\ a \in i, b \in j}}^{M} a_{a,i}(q) a^*_{b,j}(q) \left\langle e^{i[\mathbf{q} \cdot (\mathbf{r}_{a,i} - \mathbf{r}_{b,j})]} \right\rangle \tag{4.10}$$

where k is a proportionality constant and the sum runs on the M atoms a, b belonging to each of the N molecules i and j and positioned at $\mathbf{r}_{a,i}$, $\mathbf{r}_{b,j}$. If we can assume the scattering factors $a_{a,i}(q)$ to be approximately the same for all the relevant atomic centres, then Eq. 4.10 simplifies to:

$$I(\mathbf{q}) = k|a(\mathbf{q})|^2 S(q) \tag{4.11}$$

where we have introduced the *structure factor* $S(q)$

$$S(q) = \frac{1}{N} \sum_{i,j=1}^{N} \sum_{\substack{a, \\ a \in i, b \in j}}^{M} \left\langle e^{i[\mathbf{q} \cdot (\mathbf{R}_{a,i} - \mathbf{R}_{b,j})]} \right\rangle$$

$$= 1 + S_s(q) + S_d(q) \tag{4.12}$$

and where the second and third term represent the single molecule ("self") and the pairwise (or "distinct") contributions:

$$S_s(q) = \frac{1}{N} \sum_{i=1}^{N} \sum_{\substack{a,b=1 \\ a \neq b \in i}}^{M} \left\langle e^{i[\mathbf{q} \cdot (\mathbf{R}_{a,i} - \mathbf{R}_{b,i})]} \right\rangle \tag{4.13}$$

and

$$S_d(q) = \frac{1}{N} \sum_{i, \substack{j=1 \\ i \neq j}}^{N} \sum_{a, \substack{b=1 \\ a \in i . b \in j}}^{M} \left\langle e^{i[\mathbf{q} \cdot (\mathbf{R}_{a,i} - \mathbf{R}_{b,j})]} \right\rangle \tag{4.14}$$

Writing the laboratory frame position of each atomic centre as

$$\mathbf{R}_{a,i} = \mathbf{O}_i + \mathbf{r}_{a,i} \tag{4.15}$$

where $\mathbf{O}_i$ is the position of the centre of mass of the i-th molecule and $\mathbf{r}_{a,i}$ the

position of atom a in the $i-th$ molecule fixed frame, we have

$$S_s(q) = \sum_{\substack{a,b=1 \\ a\neq b}}^{M} \left\langle e^{i[\mathbf{q}\cdot(\mathbf{r}_a - \mathbf{r}_b)]} \right\rangle \tag{4.16}$$

and

$$S_d(q) = \frac{1}{N} \sum_{\substack{i,\, j=1 \\ i\neq j}}^{N} \sum_{\substack{a,\, b=1 \\ a\in i, b\in j}}^{M} \left\langle e^{i[\mathbf{q}\cdot(\mathbf{O}_i - \mathbf{O}_j)]} e^{i[\mathbf{q}\cdot(\mathbf{r}_{a,i} - \mathbf{r}_{b,j})]} \right\rangle \tag{4.17}$$

It is clear that the only term containing information relevant for smectic positional order is $S_d(q)$, which depends on molecule-molecule distances. Thus here we only concentrate on the distinct contribution and in particular, if we now consider the vertical reflections from the smectic planes, $\mathbf{q} = (0,0,1)q_n$, $q_n \equiv \frac{2\pi n}{d}$ then

$$S_d(00n) = \frac{1}{N} \sum_{\substack{i,\, j \\ i\neq j}}^{N} \sum_{\substack{a,\, b=1 \\ a\in i, b\in j}}^{M} \left\langle e^{iq_n z_{ij}} e^{iq_n[\mathbf{z}\cdot(\mathbf{r}_{a,i} - \mathbf{r}_{b,j})]} \right\rangle \tag{4.18}$$

where $z_{ij} = z_i - z_j$

Repeated use of the Rayleigh expansion and of the transformation properties of Wigner rotation matrices (see Appendix 2) shows that, assuming a uniaxial smectic and effective uniaxial molecular symmetry

$$\begin{aligned} S_d(00n) &= \sum_{L,L'} c_{nLL'} \langle \cos(q_n z_{ij}) P_L(\cos\beta_i) P_{L'}(\cos\beta_j) \rangle_{ij} \\ &= c_{n00} < \cos(q_n z_{ij}) >_{ij} \\ &+ 2c_{n02} < \cos(q_n z_{ij}) P_2(\cos\beta_j) >_{ij} \\ &+ c_{n22} < \cos(q_m n_{ij}) P_2(\cos\beta_i) P_2(\cos\beta_j) >_{ij} + ... \end{aligned} \tag{4.19}$$

The first term is the only one retained in the classical formulation[52,53], assuming

$$\langle \cos(q_n z_{ij}) \rangle_{ij} = \langle \cos(q_n z_i) \rangle^2 \tag{4.20}$$

Thus for the first two reflections:

$$S_d(001) \approx c_{100} \tau_1^2 \tag{4.21}$$

$$S_d(002) \approx c_{200} \tau_2^2 \tag{4.22}$$

and so on. We see that the root of the difficulty in comparing the simulated data with those obtained from analyses of scattering data is first in the presence of the scaling factors c_{nJL} and then in the neglect of the mixed positional-orientational terms. Even assuming these to be negligible the determination of the proportionality factor is non trivial. In a first approach, it was assumed that a calculation could be performed in the limiting case of perfect order[52]. In a more recent method[45] a global fit to different temperatures was performed assuming a Haller type[54] dependence of the smectic order on temperature. In a third case absolute measurements were performed using small angle neutron scattering[44]. In all these cases it is clear that a number of assumptions are implied, and that additional terms, like the mixed order parameters that we have shown to be non negligible should at least in principle have to be considered. It might thus be that a more refined analysis of X-ray and neutron scattering data might be needed before a comparison between simulated and experimental data that can be considered decisive for the validation of the MD results should be attempted.

Translational diffusion

Given the anisotropic nature of the 8CB LC phase, it is of interest to study the dependence of translational diffusion tensor components D_{ii} as a function of the temperature, and hence in each different phase (in particular in the SmA_d

one). This can also be of help in order to validate the simulation results through the comparison with experimental data[55] also for the dynamic and only the structural aspects.

From simulations, D_{ii} can be calculated from the mean square positional displacements using the classical Einstein formula:

$$D_{ii} = \lim_{t\to\infty} \frac{\langle (R_i(0) - R_i(t))^2 \rangle}{2t}, \tag{4.23}$$

where R_i is the component of the molecular position vector of each molecule along the axis $i = x, y, z$ of the director frame. In practice, we assume that the asymptotic long time limit and the diffusive regime is reached for values of $t \gtrsim 10$ ns. The parallel and perpendicular diffusion coefficients $D_{\parallel}$ and $D_{\perp}$ correspond to D_{zz} and $(D_{xx} + D_{yy})/2$ respectively, while the isotropic diffusion coefficient D_{iso} was calculated as $(D_{xx} + D_{yy} + D_{zz})/3$.

The simulated and experimental isotropic diffusion coefficients follow an Arrhenius temperature dependence:

$$D_{iso} = D_0 e^{-E_a/kT}, \tag{4.24}$$

where D_0 is the diffusion coefficient for temperature $T \to \infty$ and E_a is the activation energy required for molecules to get over the potential barrier encountered while moving across the sample.

We perform a linear interpolation of the diffusion coefficients reported in Table 4.4, obtaining a simulated activation energy $E_{a,sim}$ = 34.02 kJ mol^{-1}, very close to the reported experimental value[55] $E_{a,exp}$ =34.12 kJ mol^{-1}, and a $D_{0,sim}$ =1.97$\times 10^{-4}$ m^2/s against the experimental value we extrapolated from the work of A. Maliniak and coworkers[55]($D_{0,exp} \sim$ 1.96$\times 10^{-5}$ m^2/s). The D_0 value obtained from UA simulations is thus roughly one order of magnitude higher than the one found experimentally. This is not surprising, as it is well known that for molecules modeled at the united atoms level of detail, the calculated diffusion coefficients are usually higher than experimental values[10,18] as a result of the

Table 4.4: Simulated values with respect to the temperature of: mass density ρ - nematic order parameter $\langle P_2 \rangle$ - average value of the length to breadth molecular aspect ratio l/w, calculated from the dimensions of the minimal rectangular box containing the molecule rotated in its inertial frame[1] - diffusion coefficients in $10^{-10}\ m^2/s$: isotropic coefficient D_{iso}, rescaled isotropic coefficient $D_{iso,r}$, parallel coefficient from rescaled isotropic through CM model $D_{\parallel,CM}$, perpendicular coefficient from rescaled isotropic through CM model $D_{\perp,CM}$.

T (K)	$\rho\ (g/cm^3)$	$\langle P_2 \rangle$	l/w	D_{iso}	$D_{\parallel}$	$D_{\perp}$
300	1.000	0.64	3.35	2.6	3.8	1.9
302	0.998	0.62	3.37	2.6	3.9	2.0
304	0.995	0.61	3.36	2.8	4.1	2.1
305	0.993	0.62	3.36	2.8	3.9	2.2
306	0.992	0.59	3.35	3.0	4.4	2.3
307	0.990	0.58	3.34	3.0	4.3	2.3
308	0.988	0.54	3.33	3.3	4.8	2.6
309	0.987	0.56	3.16	3.4	4.9	2.6
310	0.985	0.52	3.32	3.6	5.2	2.8
311	0.982	0.45	3.28	3.8	5.4	3.1
312	0.981	0.43	3.28	4.0	5.5	3.2
313	0.975	0.20	-	4.4	-	-
314	0.973	0.16	-	4.5	-	-
316	0.970	0.14	-	4.8	-	-
320	0.963	0.11	-	5.4	-	-

smoother molecular surface. It is however interesting to see if, even this feature of UA models prevents us from performing a comparison with the absolute values of experimental results, we can at least satisfactorily obtain the anisotropy and the temperature dependence of the translational diffusion tensor.
In particular, we tried two scaling procedures that, given a simulated diffusion coefficient, will return a rescaled one directly comparable to experimental values.
(i)The first, very simple, is based on introducing two empirical scaling factors:

$$\alpha = \frac{D_{0,exp}}{D_{0,sim}}, \quad \beta = \frac{E_{a,exp}}{E_{a,sim}}, \tag{4.25}$$

which in our case correspond to $\alpha = 0.1$ and $\beta = 1.01$, to be employed in the following expression:

$$D_{iso,r} = \alpha e^{(1-\beta)\frac{E_{a,sim}}{kT}} D_{iso,sim}, \tag{4.26}$$

where $D_{iso,r}$ is the simulation-rescaled isotropic diffusion coefficient. We applied Equation 4.26 not only to rescale the isotropic diffusion coefficient, but also to the components $D_{\parallel}$ and $D_{\perp}$ in the LC phase. It is worth noting that this approach based only on a rescaling of the isotropic diffusion coefficients might fail since, in particular, the Arrhenius equation does not necessarily hold when a liquid crystal phase is present, so that we do not necessarily expect $D_{\parallel}$ and $D_{\perp}$ in both nematic and smectic ranges to be represented by the equivalent of Eq. 4.24. However, as we can see from Fig. 4.10, in practice the agreement turns out to be quite good.

(ii) The second procedure, that tries to provide a more solid basis for scaling also the diffusion components, is based on the Chu and Moroi (CM) model[55,56], which allows to compute $D_{\parallel}$ and $D_{\perp}$ for nematic phases as a function of the scalar order parameter $\langle P_2 \rangle$, ignored in the previous approach, as follows:

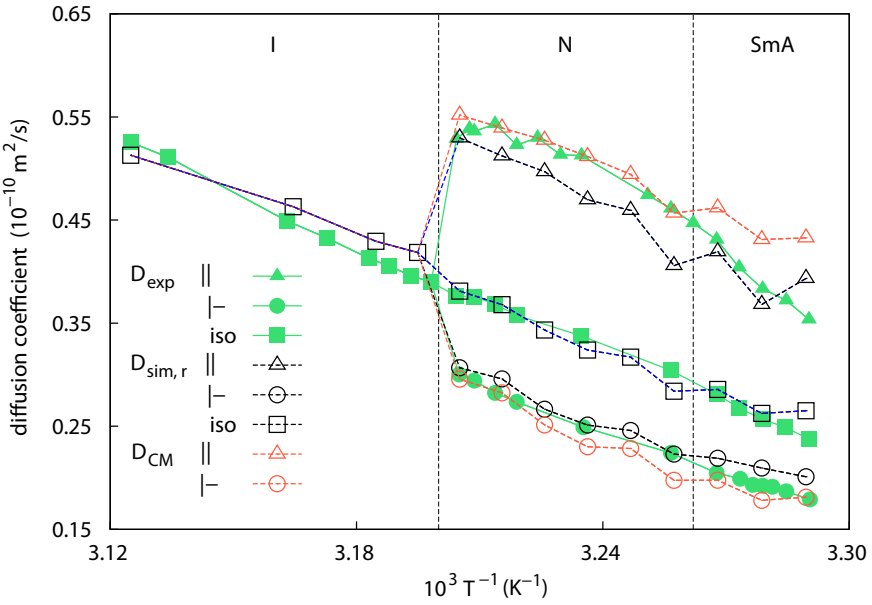

Figure 4.10: Arrhenius plot of simulation-rescaled and experimental[55] diffusion coefficients. Green filled symbols represent experimental values, blue empty symbols represent rescaled values from simulations, orange empty symbols represent values calculated with CM model. Dashed lines correspond to experimental transition temperatures.

$$D_{\parallel} = \langle D_{iso} \rangle \left[1 + 2\langle P_2 \rangle \frac{1-\xi}{2\xi+1} \right], \tag{4.27}$$

and

$$D_{\perp} = \langle D_{iso} \rangle \left[1 - \langle P_2 \rangle \frac{1-\xi}{2\xi+1} \right], \tag{4.28}$$

where $\xi = \pi w/(4l)$ is a geometrical factor for rod-like molecules of length l and section w. Through the CM model, once $D_{iso,sim}$, $\langle P_2 \rangle$ and ξ are determined from the simulation at each temperature, we can obtain rescaled parallel and perpendicular diffusion coefficients $D_{\parallel,CM}$ and $D_{\perp,CM}$ in the nematic phase using Eqs. 4.26-4.28. It is interesting to see how well the CM model will perform in calculating diffusion coefficients using only orientational order parameter even for samples in the smectic phase, where more complex models taking into account also positional order should in principle be better suited for the task[57].

In Fig. 4.10 we report a comparison between the two sets of simulation-rescaled diffusion coefficients and the experimental ones. As shown by the plots, once adequately rescaled, the diffusion coefficients of the simulated samples accurately follow the experimental trend. Moreover, it can be noticed that there is only a slight difference between the values of $D_{\parallel}$ and $D_{\perp}$ calculated from the simple rescaling with Eq. 4.26 and those predicted by the CM model, the latter method being more effective for $D_{\parallel}$.

Turning now to discussing the mobility results, we see first that, as expected for nematic phases, the diffusion along the director is faster compared to the perpendicular one. This behavior is inherited also in the smectic phase, without showing any evidence of discontinuity in correspondence of the smectic-nematic transition. This trend might seem surprising considering the idealized picture of a smectic phase as a set of stacked two dimensional fluid layers, as one would expect a lower diffusion along the director and thus across layers, due to the presence of an interlayer potential. On the other hand, it has been reported several times in previous experimental[58–60] and computational[4,15] studies that 8CB exhibits a smectic phase with a nematic-like diffusional behavior and it is comforting to see that this is also reproduced in our work.

4.4 Conclusions

We have investigated the liquid crystalline, nematic and smectic, phases of 4-n-octyl-4′-cyanobiphenyl with atomistic molecular dynamics simulations, by performing a progressive cooling of an isotropic sample. We observed the spontaneous onset of a smectic phase, in a sample composed by 750 molecules with periodic boundary conditions, which we thoroughly investigated and characterized by determining its density, orientational, positional and orientational-positional order parameters. The isotropic-nematic and the nematic-smectic transition temperatures were reproduced in very good agreement with experiment[40] (respectively within 2 K and 4 K) and a satisfactory agreement with birefringence[35–37] and polarised Raman data[11,38] was also found for the sec-

ond and fourth rank orientational order parameters $\langle P_2 \rangle$, $\langle P_4 \rangle$.

The determination of the mixed positional-orientational order parameters allowed us to evaluate for the first time the correlation between positions and orientations in smectic phases.

We have also proposed a general protocol for determining the positional order parameter τ_1 for smectic A phases from molecular dynamics simulations and we found that, for both *N*=750 and various larger, *N*=3000 molecules samples with different thermal histories, τ_1 is somewhat lower than the experimental values reported so far from X-ray and Neutron scattering measurements[44,45]. We then discussed in detail and obtained, to our knowledge for the first time, some explicit molecular expressions for the quasi-Bragg smectic reflection spots in terms of the order parameters, showing that the expressions typically used in the analysis can be somewhat oversimplified in that they neglect some contributions from mixed positional orientational order parameters. We consider this as a possible source of the apparent imperfect agreement between calculated and experimental τ_1 since on the other hand the layer spacing *d* exhibited by our samples is in very good agreement with the experimental X-ray values[21] .

As far as dynamics is concerned, we have evaluated the diffusion tensor components for molecular translations inside and across the smectic layers. Although the absolute values of the diffusion coefficients are roughly an order of magnitude larger than experiment, as usually found for united atoms models, we have shown that a simple rescaling can be used to closely reproduce the experimental temperature variation trend[55] of the diffusion tensor components. In particular, we have also observed that the diffusion coefficient across the layers is higher, up to a factor of two, than that for diffusion within the layer, as found experimentally for 8CB.

In summary, we can conclude that the force field developed in[10] is validated also for reproducing and predicting absolute values of structural data and, up to a scaling factor, translational diffusion for the smectic phase of 8CB. We trust our study will stimulate further investigations of the smectic positional and positional-orientational order parameters, that are key to a full understanding of

this important liquid crystal layered phase, but to date much less explored that their orientational counterparts.

4.5 Appendix: Explicit expression for scattering coefficients in smectic A

In this Appendix we derive an explicit expression for the distinct molecules contribution to the scattered intensity $S_d(q)$ in the particular case of reflections from the smectic A planes with $\mathbf{q} = (0, 0, 1)q_n$, $q_n \equiv \frac{2\pi n}{d}$. Assuming that the scattering vector is parallel to the director, $\mathbf{q}||\mathbf{d}$(see Eq.4.18), the scattering intensity becomes

$$S_d(00n) = \frac{1}{N} \sum_{i,\ \substack{j \\ i \neq j}}^{N} \sum_{a \in i, b \in j}^{M} \left\langle e^{iq_n z_{ij}} e^{iq_n \mathbf{z}\cdot\mathbf{r}_{a,i}} e^{-iq_n \mathbf{z}\cdot\mathbf{r}_{b,j}} \right\rangle \tag{4.29}$$

where $z_{ij} = z_i - z_j$.

We use the Rayleigh expansion

$$e^{i\mathbf{q}\cdot\mathbf{r}_{a,i}} = \sum i^L (2L+1) j_L(qr_{a,i}) D^L_{00}(\hat{\mathbf{q}} \cdot \hat{\mathbf{r}}_{a,i}) \tag{4.30}$$

with $j_L(qr)$ a spherical Bessel function[61]. Now, applying the closure relation of Wigner rotation matrices we have:

$$D^L_{00}(\hat{\mathbf{q}} \cdot \hat{\mathbf{r}}_{ai}) = \sum_m D^L_{0m}(d - r_{ai}) D^L_{m0}(q - d) \tag{4.31}$$

$$= \sum_m D^{L*}_{m0}(q - d) D^L_{m0}(r_{ai} - d) \tag{4.32}$$

$$= \sum_{m,p} D^{L*}_{m0}(q - d) \langle D^L_{mp}(M_i - d) \rangle D^L_{p0}(r_{ai} - M_i)$$

$$= \sum_{m,p} \delta_{m0} \langle D^L_{mp}(M_i - d) \rangle D^L_{p0}(r_{ai} - M_i)$$

$$= \sum_p \langle D^L_{0p}(M_i - d) \rangle D^L_{p0}(r_{ai} - M_i)$$

$$\tag{4.33}$$

where $(M_i - d)$ is the rotation from the lab (director) frame d to the $i-th$ molecule frame M_i and $(r_{ai} - M_i)$ the rotation from the molecular frame to scattering centre a. In particular, for our geometry we have used $D^{L*}_{m0}(0) = \delta(m0)$.

$$\begin{aligned}
&\langle\, e^{iq_n z_{ij}} e^{i\mathbf{q_n}\cdot\mathbf{r}_{a,i}} e^{i\mathbf{q_n}\cdot\mathbf{r}_{b,j}} \rangle = \sum i^{L+L'}(2L+1)(2L'+1) \\
&j_L(q_n r_{a,i}) j'_L(q_n r_{b,j}) \\
&\sum_{p,p'} D^L_{p0}(r_{ai} - M_i) D^{L'}_{p'0}(r_{bj} - M_j) \\
&\langle \cos(q_n z_{ij}) D^L_{0p}(M_i - d) D^L_{0p'}(M_j - d) \rangle
\end{aligned} \tag{4.34}$$

If the molecules are all identical, the position and orientations of the centres depend on internal geometry and we can just write $r_{a,i} = r_a$, $D^L_{p0}(r_{ai} - M_i) = D^L_{p0}(r_a - M)$ etc. Introducing a molecular scattering tensor of rank L:

$$A^{L,p}(q) = \sum_{a=1}^{M} i^L (2L+1) j_L(q r_a) D^L_{p0}(r_a - M) \tag{4.35}$$

we can write

$$\begin{aligned}
S_d(00n) = &\sum_{L,L'} \sum_{p,p'} A^{L,p}(q_n) A^{L',p'}(q_n) \\
&\langle \cos(q_n z_{ij}) D^L_{0p}(M_i - d) D^{L'}_{0p'}(M_j - d) \rangle_{ij}
\end{aligned} \tag{4.36}$$

where we have indicated the average over all particle pairs as $\langle [...] \rangle_{ij}$. Assuming an effective uniaxial molecular symmetry, invariance about a rotation

around the molecular axis gives $\delta_{p0}\delta_{p'0}$. Thus

$$S_d(00n) = \sum_{L,L'} A^{L,0}(q_n)A^{L',0}(q_n) \langle \cos(q_n z_{ij}) P_L(\cos\beta_i) P_{L'}(\cos\beta_j)\rangle_{ij} \tag{4.37}$$

where we have used the familiar notation $P_L(\cos\beta_i) \equiv D^L_{00}(M_i - d)$. We can thus write explicitly the coefficients in Eq.4.20 as:

$$c_{nLL'} = A^L(q_n)A^{L'}(q_n). \tag{4.38}$$

Bibliography

[1] R. Berardi, L. Muccioli, and C. Zannoni, "Can nematic transitions be predicted by atomistic simulations? A computational study of the odd–even effect," *ChemPhysChem*, vol. 5, p. 104, 2004.

[2] Y. Olivier, L. Muccioli, V. Lemaur, Y. H. Geerts, C. Zannoni, and J. Cornil, "Theoretical characterization of the structural and hole transport dynamics in liquid-crystalline phthalocyanine stacks," *J. Phys. Chem. B*, vol. 13, p. 14102, 2009.

[3] T. A. Papadopoulos, L. Muccioli, S. Athanasopoulos, A. B. Walker, C. Zannoni, and D. Beljonne, "Does supramolecular ordering influence exciton transport in conjugated systems? insight from atomistic simulations," *Chem. Sci.*, vol. 2, p. 1025, 2011.

[4] A. Pizzirusso, M. Savini, L. Muccioli, and C. Zannoni, "An atomistic simulation of the liquid-crystalline phases of sexithiophene," *J. Mater. Chem.*, vol. 21, p. 125, 2011.

[5] I. Cacelli, C. F. Lami, and G. Prampolini, "Force-field modeling through quantum mechanical calculations: Molecular dynamics simulations of

a nematogenic molecule in its condensed phases," *J. Comput. Chem.*, vol. 30, p. 366, 2009.

[6] J. Peláez and M. R. Wilson, "Atomistic simulations of a thermotropic biaxial liquid crystal," *Phys. Rev. Lett.*, vol. 97, p. 267801, 2006.

[7] C. Zannoni, "Molecular design and computer simulations of novel mesophases," *J. Mater. Chem.*, vol. 11, p. 2637, 2001.

[8] M. R. Wilson, "Molecular simulation of liquid crystals: progress towards a better understanding of bulk structure and the prediction of material properties," *Chem. Soc. Rev.*, vol. 36, p. 1881, 2007.

[9] I. Cacelli, L. De Gaetani, G. Prampolini, and A. Tani, "Liquid crystal properties of the *n*-alkyl-cyanobiphenyl series from atomistic simulations with *ab initio* derived force fields," *J. Phys. Chem. B*, vol. 111, p. 2130, 2007.

[10] G. Tiberio, L. Muccioli, R. Berardi, and C. Zannoni, "Towards in silico liquid crystals. realistic transition temperatures and physical properties for n-cyanobiphenyls via molecular dynamics simulations," *ChemPhysChem*, vol. 10, p. 125, 2009.

[11] S. J. Picken, "Measurements and values for selected order parameters," in *Physical Properties of Liquid Crystals, Vol. 1: Nematics* (D. A. Dunmur, A. Fukuda, and G. R. Luckhurst, eds.), ch. 2.2, p. 89, London: IEE, 2001.

[12] A. Sanchez-Castillo, M. A. Osipov, and F. Giesselmann, "Orientational order parameters in liquid crystals: A comparative study of X-ray diffraction and polarized raman spectroscopy results," *Phys. Rev. E*, vol. 81, p. 021707, 2010.

[13] A. Pizzirusso, M. Di Cicco, G. Tiberio, L. Muccioli, R. Berardi, and C. Zannoni, "Alignment of small organic solutes in a nematic solvent: The effect of electrostatic interactions," *J. Phys. Chem. B*, vol. 116, p. 3760, 2012.

[14] A. C. J. Weber, A. Pizzirusso, L. Muccioli, C. Zannoni, W. Meerts, C. de Lange, and E. Burnell, "Efficient analysis of highly complex nuclear magnetic resonance spectra of flexible solutes in ordered liquids by using molecular dynamics," *J. Chem. Phys.*, vol. 136, p. 174506, 2012.

[15] Y. Lansac, M. A. Glaser, and N. A. Clark, "Microscopic structure and dynamics of a partial bilayer smectic liquid crystal," *Phys. Rev. E*, vol. 64, p. 051703, 2001.

[16] A. J. McDonald and S. Hanna, "Atomistic simulation of a model liquid crystal," *J. Chem. Phys.*, vol. 124, p. 164906, 2006.

[17] L. De Gaetani and G. Prampolini, "Computational study through atomistic potentials of a partial bilayer liquid crystal: structure and dynamics," *Soft Matter*, vol. 5, p. 3517, 2009.

[18] J. Zhang, J. Su, and H. Guo, "An atomistic simulation for 4-cyano-4'-pentylbiphenyl and its homologue with a reoptimized force field," *J. Phys. Chem. B*, vol. 115, p. 2214, 2011.

[19] D. Frenkel and B. Smit, *Understanding Molecular Simulations: From Algorithms to Applications.* Academic Press, San Diego, 1996.

[20] A. Leadbetter, J. Frost, J. Gaughan, G. Gray, and A. Mosley, "Structure of smectic-a phases of compounds with cyano end groups," *J. Phys. France*, vol. 40, p. 375, 1979.

[21] S. Urban, J. Przedmojski, and J. Czub, "X-ray studies of the layer thickness in smectic phases," *Liq. Cryst.*, vol. 32, p. 619, 2005.

[22] T. Krentsel Lobko, O. Lavrentovich, and S. Kumar, "In-situ X-ray measurements of light-controlled layer spacing in a smectic- A liquid crystal," *Mol. Cryst. Liq. Cryst.*, vol. 304, p. 463, 1997.

[23] M. Martin and J. Siepmann, "Transferable potentials for phase equilibria. 1. united-atom description of n-alkanes," *J. Phys. Chem. B*, vol. 102, p. 2569, 1998.

[24] F. Chami, M. R. Wilson, and V. S. Oganesyan, “Molecular dynamics and EPR spectroscopic studies of 8CB liquid crystal,” *Soft Matter*, vol. 8, p. 6823, 2012.

[25] M. Hird, “Relationship between molecular structure and transition temperatures for calamitic structures in nematics,” in *Physical Properties of Liquid Crystals: Nematics* (D. Dunmur, A. Fukuda, and G. Luckhurst, eds.), vol. 25, p. 3, INSPEC, IEE, 2001.

[26] M. J. Cook and M. R. Wilson, “Simulation studies of dipole correlation in the isotropic liquid phase,” *Liq. Cryst.*, vol. 27, p. 1573, 2000.

[27] G. Kventsel, G. Luckhurst, and H. Zewdie, “A molecular field theory of smectic A liquid crystals - a simpler alternative to the McMillan theory,” *Mol. Phys.*, vol. 56, p. 589, 1985.

[28] W. D. Cornell, P. Cieplak, C. I. Bayly, I. R. Gould, K. M. Merz, D. M. Ferguson, D. C. Spellmeyer, T. Fox, J. W. Caldwell, and P. A. Kollman, “A second generation Force Field for the simulation of proteins, nucleic acids, and organic molecules,” *J. Am. Chem. Soc.*, vol. 117, p. 5179, 1995.

[29] J. Wang, P. Cieplak, and P. A. Kollman, “How well does a restrained electrostatic potential (RESP) model perform in calculating conformational energies of organic and biological molecules,” *J. Comput. Chem.*, vol. 21, p. 1049, 2000.

[30] J. Peláez and M. R. Wilson, “Molecular orientational and dipolar correlation in the liquid crystal mixture E7: a molecular dynamics simulation at a fully atomistic level,” *Phys. Chem. Chem. Phys.*, vol. 9, p. 2968, 2007.

[31] J. C. Phillips, R. Braun, W. Wang, J. Gumbart, E. Tajkhorshid, E. Villa, C. Chipot, R. D. Skeel, L. Kale, and K. Schulten, “Scalable molecular dynamics with "NAMD",” *J. Comput. Chem.*, vol. 26, p. 1781, 2005.

[32] H. J. C. Berendsen, J. P. M. Postma, W. F. van Gunsteren, A. D. Nola,

and J. R. Haak, “Molecular dynamics with coupling to an external bath,” *J. Chem. Phys.*, vol. 81, p. 3684, 1984.

[33] U. Essmann, L. Perera, M. L. Berkowitz, T. A. Darden, H. Lee, and L. G. Pedersen, “A smooth particle mesh Ewald method,” *J. Chem. Phys.*, vol. 103, p. 8577, 1995.

[34] A. Wuerflinger and M. Sandmann, “Equations of state for nematics,” in *Physical Properties of Liquid Crystals, Vol. 1: Nematics* (D. A. Dunmur, A. Fukuda, and G. R. Luckhurst, eds.), ch. 3.3, p. 151, London: IEE, 2001.

[35] D. A. Dunmur, A. Fukuda, and G. R. Luckhurst, eds., *Physical Properties of Liquid Crystals, Vol. 1: Nematics*, vol. 25 of *EMIS Datareview Series*. London: IEE, 2001.

[36] R. G. Horn, “Refractive indices and order parameters of two liquid crystals,” *J. Phys. France*, vol. 39, p. 105, 1978.

[37] I. Chirtoc, M. Chirtoc, C. Glorieux, and J. Thoen, “Determination of the order parameter and its critical exponent for nCB ($n = 5 - 8$) liquid crystals from refractive index data,” *Liq. Cryst.*, vol. 31, p. 229, 2004.

[38] H. F. Gleeson, C. D. Southern, P. D. Brimicombe, J. W. Goodby, and V. Görtz, “Optical measurements of orientational order in uniaxial and biaxial nematic liquid crystals,” *Liq. Cryst.*, vol. 37, p. 949, 2010.

[39] U. Fabbri and C. Zannoni, “A monte carlo investigation of the lebwohl - lasher lattice model in the vicinity of its orientational phase transition,” *Mol. Phys.*, vol. 58, p. 763, 1986.

[40] G. Luckhurst and G. W. Gray, eds., *The Molecular Physics of Liquid Crystals*. London: Academic Press, London, 1979.

[41] C. Zannoni, “Distribution function and order parameters,” in *The Molecular Physics of Liquid Crystals* (G. Luckhurst and G. Gray, eds.), p. 51, Academic Press, London, 1979.

[42] Y. Lansac, M. A. Glaser, and N. A. Clark, "Microscopic structure and dynamics of a partial bilayer smectic liquid crystal," *Phys. Rev. E*, vol. 64, p. 051703, 2001.

[43] M. Fukuto, O. Gang, K. J. Alvine, B. M. Ocko, and P. S. Pershan, "Wetting of liquid-crystal surfaces and induced smectic layering at a nematic-liquid interface: An X-ray reflectivity study," *Phys. Rev. E*, vol. 77, p. 031607, 2008.

[44] G. G. Alexander, S. M. King, R. M. Richardson, and H. Zimmermann, "Determination of the translational order parameter for smectic liquid crystals using small-angle neutron scattering," *Liq. Cryst.*, vol. 37, p. 961, 2010.

[45] N. Kapernaum and F. Giesselmann, "Simple experimental assessment of smectic translational order parameters," *Phys. Rev. E*, vol. 78, p. 062701, 2008.

[46] C. Zhang, M. Gao, N. Diorio, W. Weissflog, U. Baumeister, S. Sprunt, J. Gleeson, and A. Jakli, "Direct observation of smectic layers in thermotropic liquid crystals," *Phys. Rev. Lett.*, vol. 109, 2012.

[47] Y. G. J. Lau, R. M. Richardson, and R. Cubitt, "Smectic order induced at homeotropically aligned nematic surfaces: A neutron reflection study," *J. Chem. Phys.*, vol. 124, p. 234910, 2006.

[48] P. Pasini and C. Zannoni, *Advances in the Computer Simulations of Liquid Crystals*, p. 296. Kluwer Academic Publishers, 1998.

[49] *It is worth mentioning that an estimate of τ_1 can be obtained directly from $\tau_1^{\pm}$, knowing λ and d, by combining Eqs. 3.75 and 4.7:*

$$\tau_n = \tau_n^{\pm}\sqrt{\cos(\frac{\pi\lambda}{d})}, \tag{4.39}$$

.

[50] W. L. McMillan, “Simple molecular model for the smectic A phase of liquid crystals,” *Phys. Rev. A*, vol. 4, p. 1238, 1971.

[51] W. L. McMillan, “X-ray scattering from liquid crystals. i. cholesteryl nonanoate and myristate,” *Phys. Rev. A*, vol. 6, p. 936, 1972.

[52] A. Leadbetter, “Structural studies of nematic, smectic A and smectic C phases,” in *The Molecular Physics of Liquid Crystals* (G. Luckhurst and G. Gray, eds.), p. 285, Academic Press, London, 1979.

[53] J. Seddon, “Structural studies of liquid crystals by X-ray diffraction,” in *Handbook of Liquid Crystals. Low Molecular Weight Liquid Crystals II* (D. Demus, J. Goodby, G. Gray, H.-W. Spiess, and V. Vill, eds.), vol. 2B, p. 635, Wiley-VCH, 1998.

[54] I. Haller *Progr. Solid State Chem.*, vol. 10, p. 103, 1975.

[55] S. V. Dvinskikh, I. Furó, H. Zimmermann, and A. Maliniak, “Anisotropic self-diffusion in thermotropic liquid crystals studied by 1H and 2H pulse-field-gradient spin-echo nmr,” *Phys. Rev. E*, vol. 65, p. 061701, 2002.

[56] K. S. Chu and D. S. Moroi, “Self-diffusion in nematic liquid crystals,” *J. Phys. Colloques*, vol. 36, p. 99, 1975.

[57] F. Volino and A. J. Dianoux, “Application to self-diffusion in smectic phases,” *Mol. Phys.*, vol. 36, p. 389, 1978.

[58] S. Miyajima, A. F. McDowell, and R. M. Cotts, “Pulsed-field-gradient stimulated-spin-echo NMR study of anisotropic self-diffusion in smectic Ad liquid crystal CBOOA,” *Chem. Phys. Lett.*, vol. 212, p. 277, 1993.

[59] G. J. Krüger, H. Spiesecke, and R. V. Steenwinkel, “Nuclear magnetic relaxation and self diffusion in some liquid crystals showing smectic polymorphism,” *J. Phys. Colloques*, vol. 37, p. 123, 1976.

[60] M. P. Lettinga and E. Grelet, “Self-diffusion of rodlike viruses through smectic layers,” *Phys. Rev. Lett.*, vol. 99, p. 197802, 2007.

[61] M. Abramowitz and I. A. Stegun, *Handbook of Mathematical Functions*. Dover, N.Y., 1965.

Chapter 5

8CB freely suspended thin films

5.1 Introduction

One of the most fascinating and intriguing features of liquid crystals (LC) is their having features somehow intermediate between those of a disordered isotropic liquid and those of three dimensional crystals endowed with positional and orientational order. Thus, assuming for the moment that each mesogenic molecule can be considered as a rigid rodlike object with position $\mathbf{r}$ and orientation Ω (e.g. given by three Euler angles $\alpha\beta\gamma$[1] the probability $P(\mathbf{r}, \Omega)$ of finding a molecule at a certain position-orientation will be a constant density ρ in a liquid, a $P(\Omega)$ in a nematic LC, a periodic function in one dimension, $P(z, \Omega)$ in a layered smectic A (SmA) and a fully three dimensionally periodic function $P(\mathbf{r}, \Omega)$ belonging to some space group in a crystal. The student textbook picture of a SmA is that of an infinite regular stack of fluid layers with molecular preferred orientation (director $\mathbf{n}$) on average orthogonal to the layers and finally behaving as a 2D fluid in each layer.

Other categories of smectic exist where the molecules are tilted (smectic C) or where some local positional order around a given molecule, rather than decaying away experimentally as expected in a liquid, or surviving at arbitrary long distances like in a 2D crystal, decays with a slow, inverse power law of distance[2] behavior (smectic B, SmB).

This idealized picture is directly touching upon some fundamental aspects of

statistical mechanics, for instance the possibility of existing of a truly infinite order of the layers in 1D and the nature of a 2D fluid and its crystallization.

As for the 2D fluid nature of the layer, even when the director is perpendicular to the layer, as in SmA, the situation is far from obvious. The first issue is: what is the layer constituted of? The simplest answer would be of single molecules, so that the layer spacing would correspond to a molecular length, but this is not necessarily so, e.g. if the molecules have a strong head to tail interaction, like hydrogen bonds[3] or dipoles, forming quasi dimer pairs[4]. As it turns out this is the case for what is arguably the most well studied smectic LC i.e. 8CB (4-n-octyl-4'cyanobiphenyl) where a number of X-ray investigations[5,6] and atomistic computer simulations[7] have shown that the smectic A phase is strongly interdigitated and, in a way, the structure is more similar to a stack of bilayer formed by antiparallel pairs of molecules. In the case of 8CB the X-ray layer spacing is $d \approx 32$ Å as compared to a molecular length of ≈ 20 Å.

The simple 2D fluid picture is further challenged by experimental[8] and simulated[7] results concerning dynamics. Indeed in the ideal 2D fluid model corresponding to a stack of independent layers we would expect the diffusion coefficient for molecular movements inside the layer, $D_{\perp}$, to be much faster than that from one layer to the next, $D_{\parallel}$. In reality both measurements and simulations obtain for 8CB $D_{\parallel} > D_{\perp}$, hinting at a situation where layers are far less independent than expected, even if different smectics actually show the expected behavior. The possibility of smectic LC of forming thin freely suspended films formed by a small controlled number of layers[9] has prompted a variety of detailed experimental investigations of layering in smectics and of the nature of their phase changes as well of their similarity with transitions of 2D or 3D type as the number of layers increases. While these investigations are extremely useful and informative, very little has been done to investigate the problem at molecular level providing insight on the arrangement of molecules and quantifying local and overall positional and orientational order parameters.

Obtaining this level of detail represents an important objective that is not easy to achieve experimentally, given the dimensions of the samples involved and

the relative frail nature of the films.

Here we wish to tackle the problem for the first time with state of the art molecular dynamics simulations. We choose 8CB for which we have already developed and validated a reliable force field in Chapter 4. We simulated realistic thin films with a number of monolayers varying from 2 to 20 and determined their molecular organization.

5.2 Methods and Computational Details

Sample preparation

We ran one series of simulations with N=1500 8CB molecules and different cell section area to obtain thin films of different thickness. 8CB molecules were modelled at UA level of detail using the previously described modified AMBER-OPLS force field[10,11]. Simulations were run in NVT conditions using NAMD[12] with multiple step integration: bonded, van der Waals, and electrostatic interactions were calculated every 2, 4 and 4 fs, respectively. The samples were kept at the constant temperature of 300 K through a velocity rescaling thermostat. We have seen clearly in the simulation of bulk 8CB that the system tends to form antiparallel bilayers, making this bilayer the natural elementary film thickness unit.

In order to simulate a freely suspended film, 2D periodic boundary conditions were implemented by extending the simulation cell along the z axis thus leaving vacuum above and below the film. A 1:1 ratio between the x and y sides of the cell was kept in all simulations, obtaining a square planar section of area L^2. The Particle Mesh Ewald method was used to compute long range Coulomb interactions[13]. This setup required testing that no significant interaction was present between replicas along the z axis. We found that 50 Å of separation were sufficient to ensure the absence of unwanted interactions between periodic images.

To obtain systems each containing an almost exact number of smectic layers,

we adjusted the size of the cell section accordingly to the following relation:

$$L = \sqrt{\frac{2N \cdot A_{mol}}{n_l}} \tag{5.1}$$

Here, n_l is the desired number of monolayers, which we will simply name "layers" from now on, as a function of the area of the horizontal cell section L^2, N is the number of molecules in the sample and A_{mol} is the area occupied by a vertical 8CB molecule. Equation 5.1 shows that the theoretical number of layers is inversely proportional to the cell section area L^2. The determination of A_{mol} was carried out on a six bilayer sample through a trial and error procedure where small variations on L were imposed to find the value that maximizes the height of smectic peaks in the linear density profile. Then, from Equation 5.1 we found that a xy section area of 30.8 nm^2, corresponding to a lateral side of 62 Å, is the optimal one to accommodate the six bilayers at best.
NVT simulations at T=300 K were run for systems with $n_l = 1 - 12$, including also samples featuring a odd theoretical number of layers n_l (see Figure 5.1). Each simulation was run for at least 100 ns of production time. An additional series of NVT simulations on a 12 layer sample with temperatures ranging from 300 to 325 K was run to study the effects of having the free film on transition temperatures and to observe any variation on the 8CB phase diagram compared to the one obtained for bulk samples[7].
Finally, one additional system composed of N=12000 8CB molecules (n_L = 20, L = 136 Å) was simulated to determine the existence and extent of the positional order excess generated by the two vacuum interfaces.

5.3 Results and discussion

Surface tension

In the bulk of a liquid, each molecule is equally attracted by its neighbours, resulting in a strong cohesive force. Conversely, molecules lying on the surface

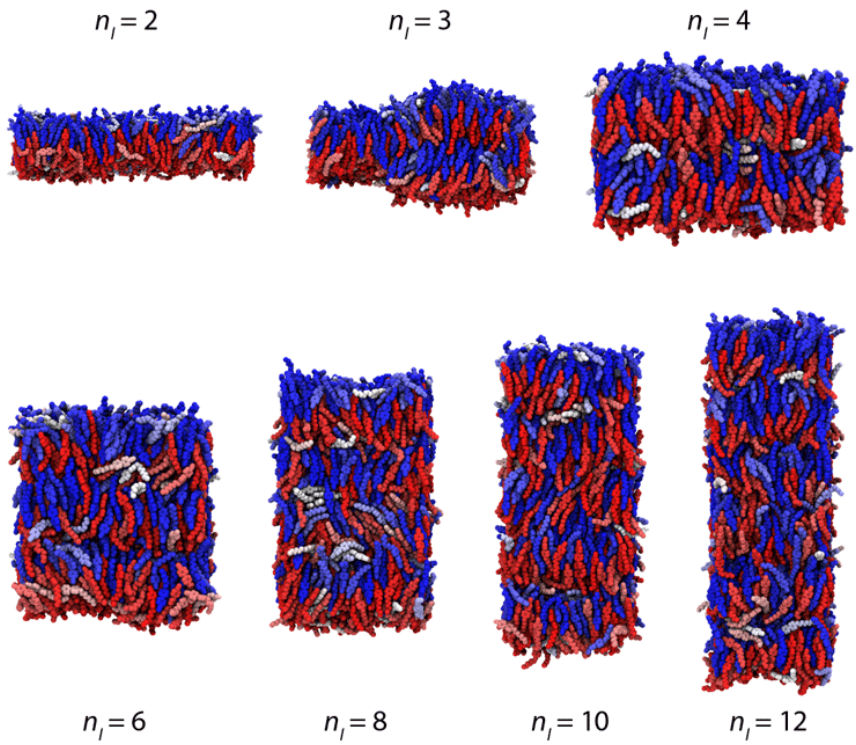

Figure 5.1: Equilibrated configurations at 300 K of films with different thickness.

experience an imbalance of forces that usually leads to the molecules being pulled toward the rest of the liquid. Thus, the system possesses a surface excess energy, defined as the energy difference between the bulk sample and one with any surface exposed to a different phase. At constant temperature, volume, and number of particles, the surface tension γ can be defined as the derivative of the Helmoltz free energy F with respect to the surface area A:

$$\gamma = \left(\frac{\partial F}{\partial A}\right)_{T,V,N} \tag{5.2}$$

Obtaining a rough estimate of the surface tension from simulations is fairly straightforward since the average value of the potential energy for every system is known. In fact, if we neglect entropy effects, surface energies can be simply calculated as the difference between the average potential energy of each film U_{film} and the one of the bulk U_{bulk}. For 8CB molecules modeled with our alkyl cyanobiphenyl force field[14], such energy corresponds to 53 kcal/mol (at 300 K and 1 atm). The ratio between such excess energy and twice the surface area

Table 5.1: Number of molecules N, calculated number of layers n_l (Eq. 5.1), horizontal cell side L, excess potential energy per molecule of the film with respect to the bulk U_s, surface tension γ and average order parameter $\langle P_2 \rangle$.

N	n_l	L(Å)	U_s (kcal/mol)	$\gamma(mN/m)$	$\langle P_2 \rangle$
1500	2	152	37.38	843.65	0.65 ± 0.01
-	3	124	0.75	25.3	0.61 ± 0.02
-	4	107	0.45	20.3	0.65 ± 0.01
-	5	96	0.55	31.1	0.56 ± 0.02
-	6	88	0.30	20.3	0.65 ± 0.02
-	7	81	0.39	30.7	0.59 ± 0.02
-	8	76	0.21	19.2	0.64 ± 0.02
-	9	72	0.28	28.6	0.61 ± 0.02
-	10	68	0.18	20.7	0.64 ± 0.02
-	11	65	0.21	26.3	0.61 ± 0.02
-	12	62	0.14	19.2	0.64 ± 0.02
12000	20	136	0.10	22.6	0.61 ± 0.01

of each film (since free standing films have two interfaces with the vacuum) returns the surface tension:

$$\gamma = \frac{U_{film} - U_{bulk}}{2L^2} \tag{5.3}$$

In Table 5.1, the values of the potential energy for systems with different number of layers n_l are reported. The film featuring just one bilayer (n_l=2) has a much higher value of potential energy compared to the other samples, therefore suggesting that such system may be very unstable. This is in agreement with the fact that the thinnest film which can be prepared experimentally is at least two bilayers thick[15]. It can be seen in Table 5.1 that the potential energy of the system decreases as the number of layers increases. This is because the more layers are added, the less significant the fraction of molecules on the surface becomes, compared to the total number of molecules. It can also be observed that simulated samples possessing a odd n_l show a higher value of potential energy, indicating that they are less stable than the ones with even n_l. It is worth noting that as (odd) n_l increases, the "stress" on the smectic structure arising from the excess/lack of molecules can be distributed more efficiently, eventually becoming negligible for high n_l. In this case a comparison

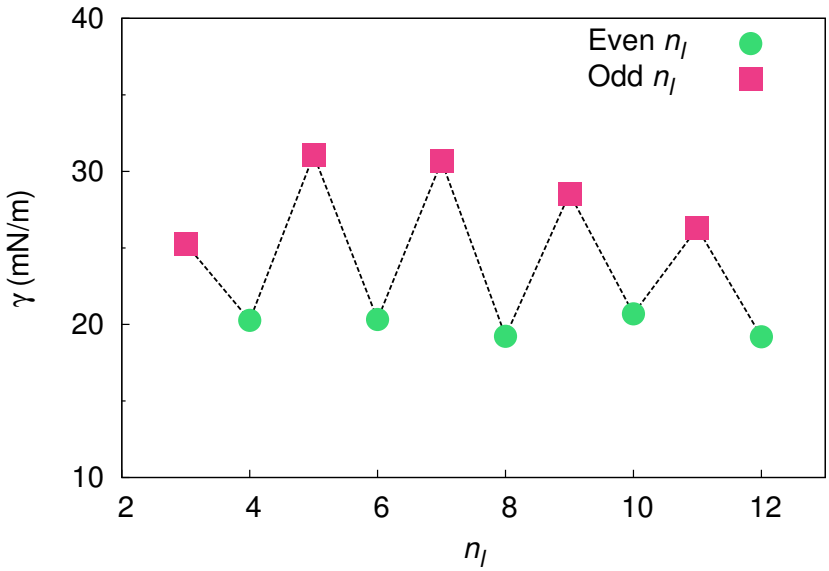

Figure 5.2: Surface tension γ as a function of the number of theoretical layers n_l for N=1500 samples.

with experiments cannot be performed due to the impossibility of drawing stable films with odd n_l. This is due to the unavoidable presence of menisci[16], which acts as a buffer for the excess/lack of molecules created when trying to arbitrary set the surface/volume ratio, i.e. extend or reduce the thickness of the film in a continuous manner.

In Figure 5.2, the trend of the surface tension is reported for both samples with even and odd n_l. Experimental measures show that for thin films with n_l up to 200 the surface tension can be considered constant with respect to the thickness[17]. Also the surface tension of simulated systems with even n_l shows a constant trend, with an average value of 20 $\pm$ 1 mN/m. This is not too far from experimental measurements, which range from 24 to 30.9 mN/m depending on the technique[18–21]. It should also be considered that entropic effects, which are not included in our evaluation of the surface tension, should increase the actual value of the simulated γ, as the interface with vacuum is more ordered than the bulk 8CB (see below). It turns out that samples featuring a odd n_l possess a higher value of γ than those with even n_l but, as mentioned above, we expect such difference to decrease as systems with a high n_l are progressively considered. A special reference must be made for the sample

with $n_l = 3$, for which we observe a value of γ lower than expected. Differently for all the other films with a odd n_l, where the excess of molecules promotes the formation of $(n_l+1)/2$ bilayers, in this system no inner layers can form and thus we observe to two coexisting regions with one and two bilayers, respectively (see snapshot in Figure 5.1). This contributes to lowering the overall potential energy of the sample, resulting then in a lower value of surface tension.

Orientational order

To provide a quantitative measure of the degree of orientational order in 8CB films we calculated the second moment of the single molecule orientational distribution, usually referred to as $\langle P_2 \rangle$. This order parameter has been computed, as described in Chapter 3, by building and diagonalizing a ordering matrix $\mathbf{Q}$[22]:

$$\mathbf{Q}(t) = \frac{1}{2N} \sum_{i=1}^{N} \left[3\hat{u}_i(t) \otimes \hat{u}_i(t) - \mathbf{I} \right], \tag{5.4}$$

where $\hat{u}_i$ is the chosen reference molecular axis, in this case being the principal inertial axis of the molecule, and $\mathbf{I}$ is the identity matrix. Instantaneous values of P_2 of each configuration are obtained by taking the largest eigenvalue of the $\mathbf{Q}$ matrix and then are averaged over the production trajectory. In Figure 5.3 and in Table 5.1 we report the values of $\langle P_2 \rangle$ as a function of the number of layers in the sample. For systems with even n_l, it can be seen that $\langle P_2 \rangle$ does not depend on the number of layers and coincides with the value found in bulk. Samples featuring a odd value of n_l (with $n_l > 5$) instead show an increasing trend of the order, as the excess of molecules not fitting within a whole bilayer can be better distributed over several ones at increasing n_l. The system with n_l=3 needs a special mention, as it is characterized by the coexistence of two distinct regions featuring one and two bilayers respectively, allowing for a higher order, comparable to samples with a even n_l. A better understanding of the orientational order in smectic thin films can be obtained by studying how it is related to the peculiar spatial organization of smectic bilayers. With this purpose, we report

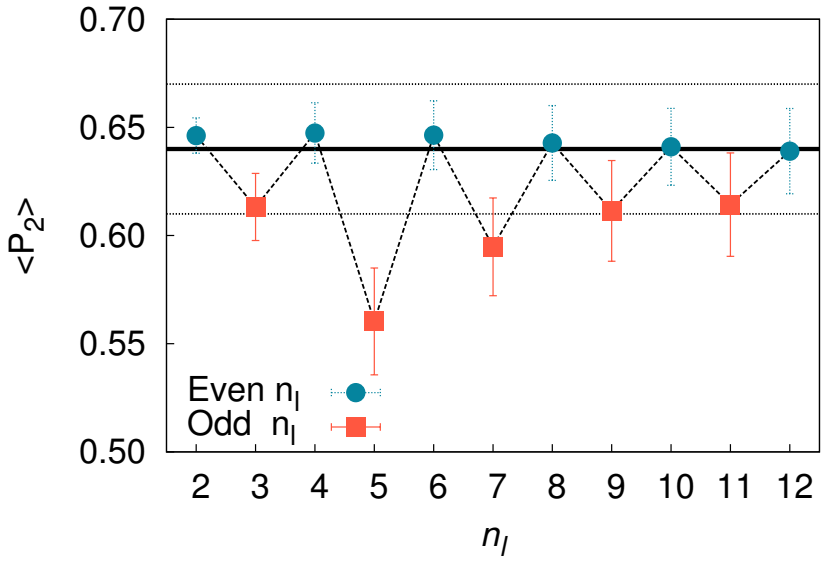

Figure 5.3: Average second rank order parameter $\langle P_2 \rangle$ as a function of the number of theoretical layers in the film. The black line corresponds to the bulk average $\langle P_2 \rangle$ within its standard deviation (dotted lines) for a sample of 750 molecules[7].

in Figure 5.4 the trend of the local orientational order along the layer normal, $P_2(z)$, whose profiles have been built by computing this order parameter for each molecule through the second rank Legendre polynomial and averaging the histogram of all the configurations:

$$P_2(z) = \frac{3}{2}\langle \hat{u}_i \cdot \hat{z} \rangle - \frac{1}{2} \tag{5.5}$$

where $\hat{u}_i$ is the reference axis of the single molecule and $\hat{z}$ is the normal to the surface, in this case coincident with the phase director. It can be seen in Figure 5.4 that the orientational order is not constant along z, and that the profile resembles the one observed for the density $\rho(z)$ in the smectic phase, with each peak located in correspondence of the bilayer center, while a steep decreasing of the order parameter is observed at the interstitial space between two adjacent layers. For systems with even values of n_l up to 12, no relevant dependence of the peak height as a function of the number of layers is observed, resulting in the constant trend of $\langle P_2 \rangle$, previously shown in Figure 5.3. A special reference needs to be made again for the n_l = 20 sample, where inner

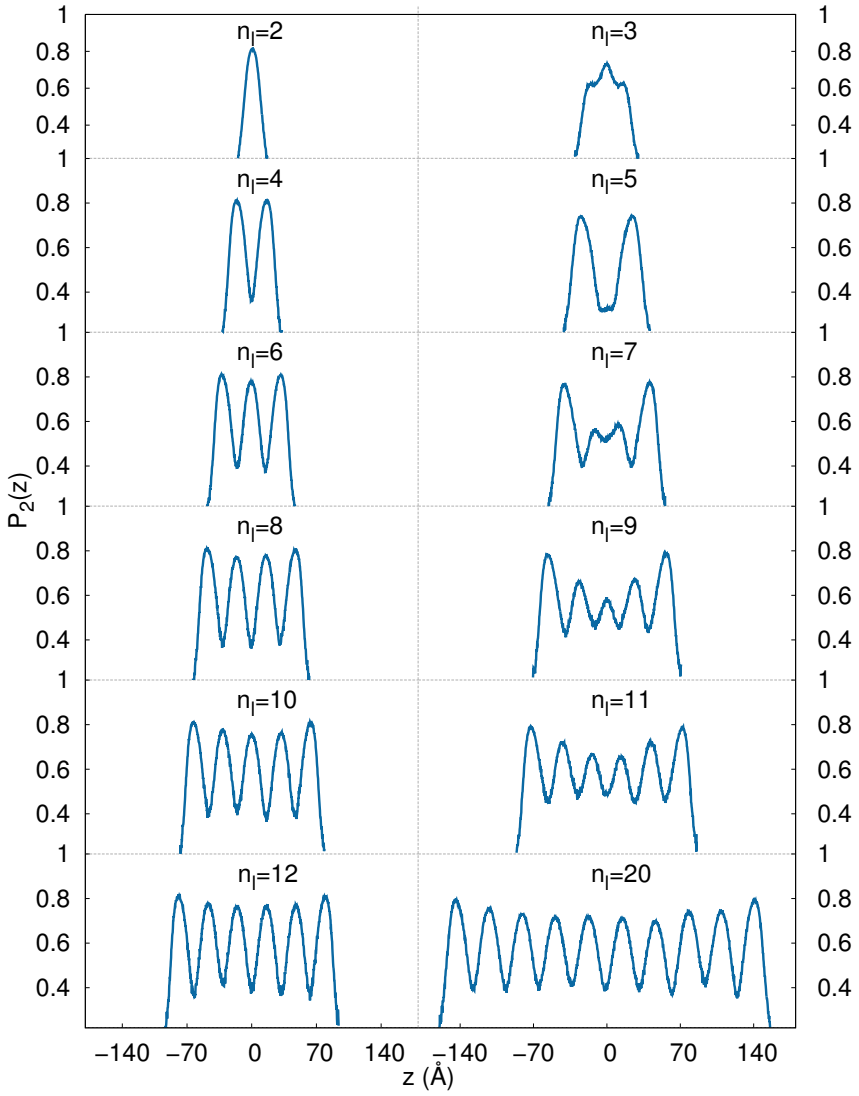

Figure 5.4: Second rank order parameter $P_2(z)$ as a function of the position along the layer normal.

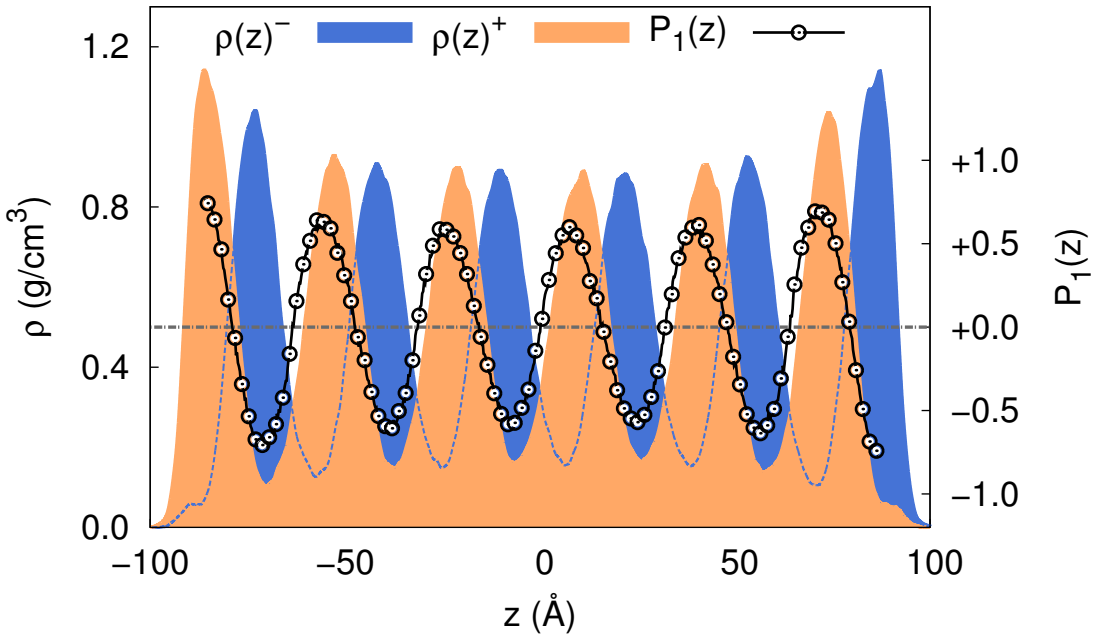

Figure 5.5: Density profiles of the layers $\rho(z)^{\pm}$ and polar order parameter $P_1(z)$ as a function of z for the $n_l = 12$ sample.

layers show a slightly lower orientational order compared to the external ones. Samples with odd n_l feature lower peaks for the internal layers or no peaks at all in the case of n_l=5 layers (Figure 5.4). As the sample thickness increases, the disorder originating from the excess of molecules can be better distributed among the layers and thus we observe gradually higher internal peaks, thus the increasing trend of the average order parameter in Figure 5.3. Again, the system with n_l=3 is an exception to this trend and features a value of $\langle P_2 \rangle$ higher than expected in the center of the film and a lower value at the surface.

More details about the orientational order within the layers can be obtained from the first order parameter profiles along the normal to the interface $P_1(z) = \hat{u}_i \cdot \hat{z}$. Such a profile is reported in Figure 5.5 for the $n_l = 12$ sample, together with the density profiles of the individual layers $\rho(z)^-$ and $\rho(z)^+$, corresponding to molecules with $P_1 > 0$ or < 0, respectively. It can be seen that each change of sign of $P_1(z)$ is located in correspondence of the positions z at which $\rho(z)^+$ and $\rho(z)^-$ cross. It is also evident from the density profile that peaks corresponding to the outside layers facing vacuum are much taller than their inner counterparts, suggesting the presence of a net surface dipole moment for thin

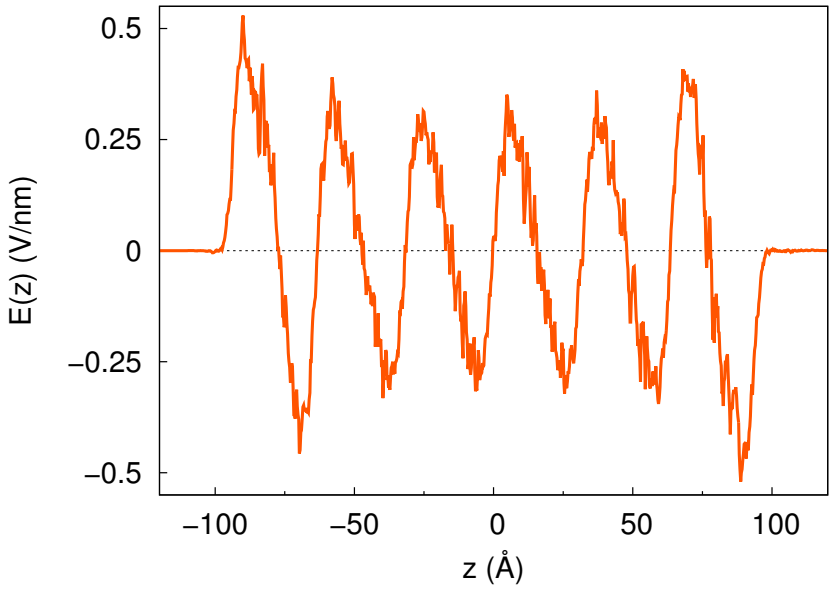

Figure 5.6: Electric field $E(z)$ along z axis for the $n_l = 12$ sample.

films. This can be confirmed by plotting the electric field profile $E(z)$ along z axis (Figure 5.6), which can be obtained from the integration of Gauss's law in differential form (also known as 1st Maxwell's equation) $\nabla \cdot \vec{E} = \delta/\varepsilon_0$:

$$E(z) = \frac{1}{\varepsilon} \int_0^z \delta(z')\, dz' \tag{5.6}$$

where δ is the charge density calculated from the simulation. Similarly to $P_1(z)$, $E(z)$ features peaks of opposite signs, as molecules of each sublayers are pointing in opposite directions. The extent of the oscillation though is sensibly higher at the two outside interfaces, as well as showing an enhanced asymmetry between peaks belonging to the same bilayer, revealing to the presence of a local net dipole. This net dipole is of course pointing in opposite directions for the two top and bottom layers, so that the electric field and the electrostatic potential are zeroed outside the thin film.

Positional order

At a temperature below 306.6 K, 8CB is known to rearrange forming a smectic phase called SmA_d, characterized, as mentioned before, by the presence

of bilayers each composed by two interdigitated layers of molecules that are oriented in opposite directions in order to optimize the interaction between the cyano polar groups.

For a layered phase such as the SmA_d one, the structural periodicity can be expressed in terms of the positional order parameters τ_n[23,24]:

$$P(z) = \frac{1}{d} + \frac{2}{d}\sum_{n=1}^{\infty} \tau_n \cos(q_n z) = \frac{\rho(z)}{\rho_0} \cdot \frac{1}{d} \tag{5.7}$$

where d is the layer spacing, $q_n \equiv 2\pi n/d$, $\tau_n \equiv \langle \cos(q_n z) \rangle$ is the nth order parameter, $\rho(z)$ is again the number density profile and ρ_0 is the average density. As already reported in Chapter 4, the smectic phase of 8CB is adequately described in terms of the first order τ_1 parameter only, which we will generically refer to as τ, while higher order terms can be neglected. At an interface with vacuum, such positional order is enhanced, as molecules align homeotropically exposing their alkyl chains to a air or vacuum surface[25–27]. The homeotropic disposition of molecules at the interface minimizes the molecular cores exposed to the surface and the loss of attractive interactions with the neighbours, and promotes the formation of layers along the direction perpendicular to the surface across the whole sample. Smectic films experimentally show considerable oscillations in the density profile along the direction normal to the layers, and usually a higher positional order parameter at the interface compared to the bulk phase[28]. In Figure 5.7 we show the density profiles along the direction normal to the interface of all simulated samples. It can be observed that for each film only a $n_l/2$ (even n_l) or a $(n_l + 1)/2$ (odd n_l) number of peaks is present, as the systems are actually constituted by bilayers and not monolayers. Furthermore, the density oscillation for the two external bilayers exposed directly to the vacuum is higher compared to the internal ones. For systems with even n_l, the decay of oscillations towards the center of the film can be noticed exclusively for the minima of density profiles, while the maxima remain substantially constant for all films with n_l up to 12 layers. Conversely, a decreasing trend also for the maxima can be found for the 20 layer film.

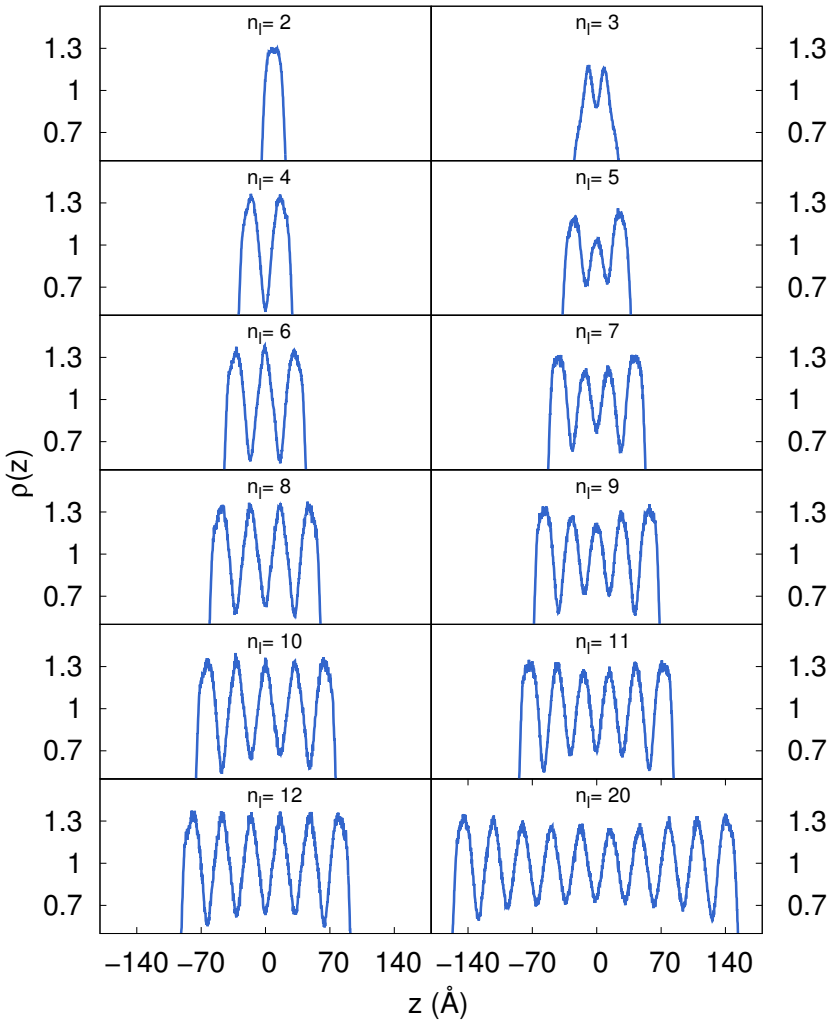

Figure 5.7: Density profiles $\rho(z)$ along the z axis for samples ranging $n_l =$ from 2 to 20.

In Table 5.2 we report the local values of τ for the bilayers of each film, which were determined by measuring the projection on the y axis of the distance between maxima and minima of each peak in $\rho(z)$. Values of τ found in thin films are overall higher than that of the bulk ($\sim$ 0.15). Moreover, the highest values of τ are found for the external bilayers in all samples. For systems with even n_l only a minimum lowering of positional order is found for the internal layers, which is instead more pronounced in systems with odd n_l.

The bilayer spacing d was determined from the peak half width at $\rho_0 = 1$ g/cm^3 in the $\rho(z)$ profiles, and values for each layer are reported in Table 5.3. It can be observed that internal peaks feature a value of d of $\sim$ 32 Å, very close to the bulk values[7], while the external ones are much larger, with a width oscillating between 36 and 40 Å. A similar value for the bilayer spacing is found by measuring the distance between sign changes in $P_1(z)$ profiles (Figure 5.5). Systems with odd n_l show a much more prominent dependence of the positional order on the distance from the interfaces. In particular, internal bilayers feature a much lower order parameter compared to systems with even n_l, going as low as $\tau = 0.12$ (Table 5.2). In these systems, we can also observe a reduction of the layer spacing (Table 5.3) of $\sim$ 3 Å. This reduction is explained by the previous observation that the real number of bilayers for odd n_l samples is always integer and equal to $(n_l + 1)/2$.

While density profile oscillations of bulk systems can be accurately described by Equation 5.7, this is not the case for thin films, as in these systems the order parameter is not constant through the sample. Picano et al.[29] derived a model where the variation of positional order is explicitly taken into account with an excess term τ_{exc}:

$$P(z) = \frac{1}{d} + \frac{2}{d}\sum_{n=1}^{\infty}[\tau_n^{exc}(z) + \tau_n^c]\cos(q_n z) \tag{5.8}$$

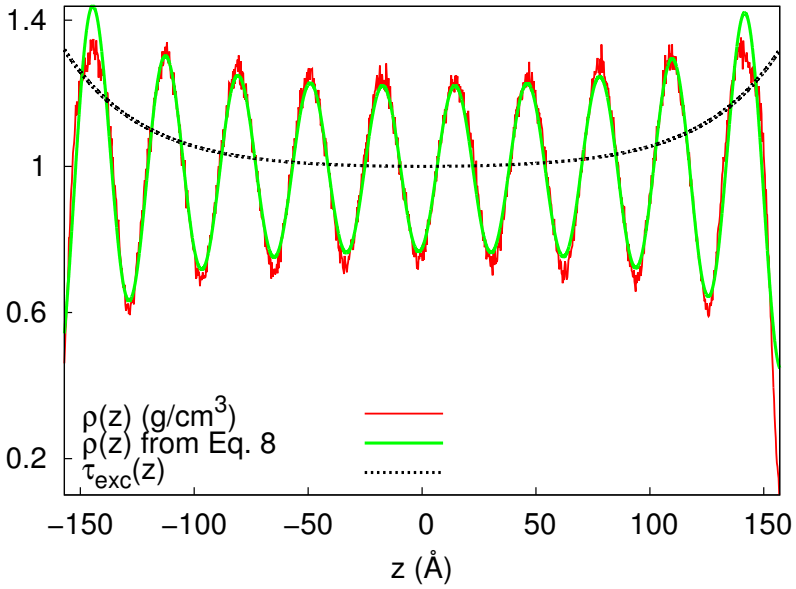

Figure 5.8: Fit of the density profile along the z axis for the $n_l = 20$ layer film through Equation 5.8. The dashed black line represent the excess of τ as a function of the distance from the center of the sample.

The surface induced excess is defined as:

$$\begin{aligned} \tau_{exc}(z) &= \tau(z) - \tau_c \\ &= \frac{\tau_{surf}}{\cosh\left(\dfrac{h}{\sqrt{2}\,\xi}\right)} \cosh\left(\frac{\sqrt{2}\,z}{\xi}\right) \end{aligned} \tag{5.9}$$

where ξ is the correlation length, h is the film thickness and τ_c is the smectic order parameter for the bulk of the film, were the surface induced order is negligible. Here, two assumption are made: the first is that the positional order decays exponentially and symmetrically moving away from the interface, as imposed by the hyperbolic cosine term, recalling that $\cosh = \frac{1}{2}(e^x + e^{-x})$, and the second is that the studied film is thick enough to have a central region where surface induced order is not significant.

Since it was not possible to obtain the convergence of the fit of the density profile $\rho(z)$ using Equation 5.8 on smaller samples (N=1500), probably because their thickness is comparable to the correlation length ξ, we attempted to fit the $\rho(z)$ of largest sample (N=12000, n_l = 20). In Figure 5.8 we report the nor-

malized density profile of this sample together with the fit performed through Equation 5.8 and the trend of $\tau_{exc}(z)$. The fitting function reproduces only approximately the amplitude of $g(z)$ oscillations. The density profile of the two outmost bilayers is in fact overestimated. It can also be seen that the minima and maxima of the density oscillation are not symmetric, the former decreasing more steeply compared to the latter. This behaviour cannot be accounted by Equation 5.8, as the cosine term oscillates symmetrically around the mean value of density. Additionally, Equation 5.8 considers the layer spacing to be constant and independent of the distance of the interface, while for our model this is not the case, as discussed above. Nevertheless, through this exercise we obtain an estimate of the correlation length ξ, which from the fit is in the order of magnitude of a few nanometers ($\sim$ 5 nm, with τ_{surf} set to 0.17).

Table 5.2: Positional order parameter of each couple of bilayers, measured from the projection of the distance between maxima and minima of each peak on the y axis in $\rho(z)$ profiles, for both systems with even and odd n_l. Pairs of layers are numbered progressively from $l = 1$ for the innermost ones to $l = n_l/4$ if $n_l/2$ is even, and from $l = 0$ to $l = (n_l - 2)/4$ if it is odd.

n_l	$\tau_{l=0}$	$\tau_{l=1}$	$\tau_{l=2}$	$\tau_{l=3}$	$\tau_{l=4}$	$\tau_{l=5}$
4		0.20				
5	0.08	0.13				
6	0.19	0.18				
7		0.12	0.16			
8		0.18	0.18			
9	0.12	0.16	0.17			
10	0.16	0.17	0.18			
11		0.14	0.17	0.17		
12		0.17	0.18	0.18		
20		0.13	0.14	0.15	0.17	0.18

Table 5.3: Layer spacing of each couple of bilayers, measured from the peak half width at $\rho_0 = 1$ in the $\rho(z)$ profiles, for both systems with even and odd n_l. Pairs of layers are numbered progressively from $l = 1$ for the innermost ones to $l = n_l/4$ if $n_l/2$ is even and from $l = 0$ to $l = (n_l - 2)/4$ if it is odd.

n_l	$d_{l=0}$	$d_{l=1}$	$d_{l=2}$	$d_{l=3}$	$d_{l=4}$	$d_{l=5}$
4		37.3				
5	13.3	33.2				
6	32.0	36.8				
7		27.3	35.2			
8		31.8	37.0			
9	28.2	29.3	36.0			
10	31.8	32.0	37.1			
11		29.5	30.2	36.1		
12		31.3	32.1	37.0		
20		33.2	32.4	32.3	32.0	36.1

Temperature dependence of the order in a 8CB thin film

The presence of a surface, other than leading to a higher positional order and inducing a homeotropic alignment of layers, exerts a major influence also on the transition temperatures of the LC phase. In fact, smectic films can also exist above the bulk smectic-nematic transition T_{SmN}, forming metastable systems called presmectic films[30]. Such films maintain the lamellar structure typical of smectics, but the amplitude of density oscillations along the layer normal becomes much weaker toward the center of the film as temperature is increased. Another phenomenon peculiar to these systems is the so called thinning transition[31–33], consisting in a successive spontaneous layer-by-layer disruption occurring as the film is heated. Experiments show that for a certain temperature T there exists a maximum film thickness $n_l(T)$ above which the film thins spontaneously, whereas films thinner than such threshold number of layers are stable[17]. Thinning transitions can be observed even below the bulk transition temperature if an external field perpendicular to the layer normal is applied to the film[34]. It must be noted that in the case of 8CB, thinning temperatures cannot be experimentally determined for systems composed by less than ten layers. This is due to the fact that the thinning temperature exceeds

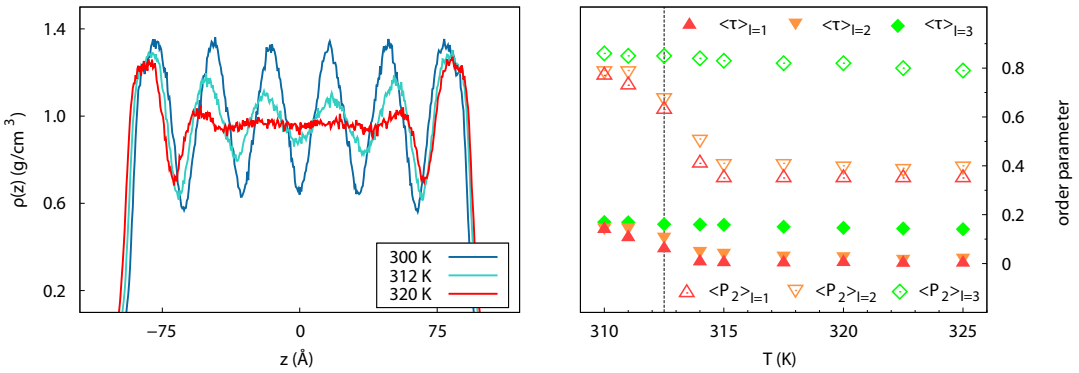

Figure 5.9: On the left, density profiles of the six layer film along the z axis at 300, 312 and 320 K. On the right, second rank average order parameter $\langle P_2 \rangle$ and average positional order parameter τ for layer pairs $l = 1, 2, 3$ as a function of temperature. The black vertical dashed line represents the T_{NI} of the bulk sample.

the nematic-isotropic liquid transition temperature, thus the meniscus melts and the formation of droplets of isotropic liquid occurs, eventually leading to the film breakage[29].

In order to verify whether our model system is able to reproduce any of the previous experimental observations, we ran a series of simulations on the sample with n_l=12 by heating it progressively from 310 to 325 K. In Figure 5.9 we report the corresponding density profile along the layer normal $g(z)$ as a function of temperature. The inner bilayers are numbered as $l = 1$, with the external one $l = 3$ and the one in between $l = 2$. It can be seen that as the sample is heated into the nematic temperature range (310-312.5 K), density oscillations decrease in its middle, while bilayers on the surfaces remain well defined, in agreement with experimental observations. The transition can be studied more in detail in Figure 5.9 by observing the trend of $\langle P_2 \rangle$ and of τ for each bilayer, determined as explained in the previous section. It can be noted that above 314 K the orientational order drops below 0.3, which is the threshold under which we consider a sample as orientationally isotropic. While the external bilayers ($l = 3$) experience only a slight loss of positional order as the temperature is increased, those with $l = 1, 2$ show a substantial decay of τ between 311 and 315 K. For bilayers with $l = 1$ the order parameter decreases much more quickly than for those with $l = 2$, even though we cannot safely state that the

system would undergo a layer-by-layer thinning transition if the meniscus was present. It is worth noting that even after 314 K, where we find an isotropic value of orientational order parameter ($\langle P_2 \rangle$ lower than 0.3), the value of $\tau_{l=3}$ is still comparable with the ones of the bulk sample. The simultaneous reduction of positional and orientational order might indicate the loss of nematic phase for very thin films like the one studied in this work, though we cannot exclude its presence in a very narrow temperature range.

5.4 Conclusions

We studied 8CB freely suspended smectic thin films by fixing the surface area and the total number of molecules in order to obtain samples with both even and odd number of theoretical layers. In the second case, we observed that if the number of molecules is intermediate between the optimal one for forming $(n_l - 1)/2$ and $(n_l + 1)/2$ bilayers, $(n_l + 1)/2$ bilayers are formed, with a substantial increase of the surface tension and a decrease of the order in the inner layers. In the case of n_l=3, where no inner bilayers can form, regions with one and two layers coexist. The first bilayer at the interface with vacuum has a higher positional and orientational order, and largest spacing with respect to the bulk, while inner layers are only weakly influenced. We also measured the characteristic length of propagation of the surface induced ordering, and it turned out to be of about 5 nanometers. The surface induced order translates also in an increased temperature stability of the smectic phase for each layer, depending on its position with respect to the surface, with the innermost portion of the sample becoming isotropic at higher temperatures than the outer ones.

Bibliography

[1] P.-G. De Gennes and J. Prost, *The physics of liquid crystals*, vol. 23. Clarendon press Oxford, 1993.

[2] J. M. Kosterlitz and D. J. Thouless, “Ordering, metastability and phase transitions in two-dimensional systems,” *J. Phys. C: Solid State Phys*, vol. 6, no. 7, p. 1181, 1973.

[3] S. Nenon, R. Mereau, S. Salman, F. Castet, T. Van Regemorter, S. Clima, D. Beljonne, and J. Cornil, “Structural and electronic properties of the ttf/zno (10–10) interface: insights from modeling,” *J. Phys. Chem. Lett.*, vol. 3, no. 1, pp. 58–63, 2011.

[4] R. Dbrowski, J. Janik, J. Janik, and K. Otnes, “A neutron scattering study of dimerization and pairing of molecules in liquid crystal mixtures,” *Liq. Cryst.*, vol. 3, no. 4, pp. 443–452, 1988.

[5] S. Urban, J. Przedmojski, and J. Czub, “X-ray studies of the layer thickness in smectic phases,” *Liq. Cryst.*, vol. 32, pp. 619–624, 2005.

[6] A. Leadbetter, J. Frost, J. Gaughan, G. Gray, and A. Mosley, “The structure of smectic A phases of compounds with cyano end groups,” *J. Phys. France*, vol. 40, no. 4, pp. 375–380, 1979.

[7] M. F. Palermo, A. Pizzirusso, L. Muccioli, and C. Zannoni, “An atomistic description of the nematic and smectic phases of 4-n-octyl-4’ cyanobiphenyl (8CB),” *J. Phys. Chem*, vol. 138, pp. 204901–204916, 2013.

[8] S. V. Dvinskikh, I. Furó, H. Zimmermann, and A. Maliniak, “Anisotropic self-diffusion in thermotropic liquid crystals studied by 1H and 2H pulse-field-gradient spin-echo nmr,” *Phys. Rev. E*, vol. 65, p. 061701, 2002.

[9] P. Oswald and P. Pieranski, *Smectic and columnar liquid crystals: concepts and physical properties illustrated by experiments*. CRC Press, 2005.

[10] W. D. Cornell, P. Cieplak, C. I. Bayly, I. R. Gould, K. M. Merz, D. M. Ferguson, D. C. Spellmeyer, T. Fox, J. W. Caldwell, and P. A. Kollman, “A second generation force field for the simulation of proteins, nucleic acids, and organic molecules,” *J. Am. Chem. Soc.*, vol. 117, p. 5179, 1995.

[11] J. Wang, P. Cieplak, and P. A. Kollman, “How well does a restrained electrostatic potential (RESP) model perform in calculating conformational energies of organic and biological molecules?,” *J. Comput. Chem.*, vol. 21, p. 1049, 2000.

[12] J. C. Phillips, R. Braun, W. Wang, J. Gumbart, E. Tajkhorshid, E. Villa, C. Chipot, R. D. Skeel, L. Kale, and K. Schulten, “Scalable molecular dynamics with NAMD,” *J. Comput. Chem.*, vol. 26, pp. 1781–1802, 2005.

[13] U. Essmann, L. Perera, M. L. Berkowitz, T. A. Darden, H. Lee, and L. G. Pedersen, “A smooth particle mesh Ewald method,” *J. Chem. Phys.*, vol. 103, pp. 8577–8593, 1995.

[14] G. Tiberio, L. Muccioli, R. Berardi, and C. Zannoni, “Towards in silico liquid crystals. realistic transition temperatures and physical properties for n-cyanobiphenyls via molecular dynamics simulations,” *ChemPhysChem*, vol. 10, p. 125, 2009.

[15] T. Stoebe, P. Mach, and C. C. Huang, “Surface tension of free-standing liquid-crystal films,” *Phys. Rev. E*, vol. 49, pp. 3587–3590, 1994.

[16] K. Harth, B. Schulz, C. Bahr, and R. Stannarius, “Atomic force microscopy of menisci of free-standing smectic films,” *Soft Matter*, vol. 7, pp. 7103–7111, 2011.

[17] P. Oswald and P. Pieranski, *Smectic and Columnar Liquid Crystals*, ch. VIII.2. Taylor & Francis Group, 2005.

[18] R. Stannarius and C. Cramer, “Self-supporting bubbles of thermotropic smectic liquid crystals,” *Europhys. Lett.*, vol. 42, p. 43, 1998.

[19] M. Eberhardt and R. B. Meyer, “Tensiometer for free standing smectic films,” *Rev. Sci. Instrum.*, vol. 67, p. 2846, 1996.

[20] H. Schüring, C. Thieme, and R. Stannarius, “Surface tensions of smectic liquid crystals,” *Liq. Cryst.*, vol. 28, p. 241, 2001.

[21] F. Schneider, “A novel method for measuring the surface tension of free standing smectic films,” *Rev. Sci. Instrum.*, vol. 73, p. 114, 2002.

[22] D. Frenkel and B. Smit, *Understanding Molecular Simulations: From Algorithms to Applications.* Accademic Press, San Diego, 1996.

[23] W. L. McMillan, “Simple molecular model for the smectic A phase of liquid crystals,” *Phys. Rev. A*, vol. 4, p. 1238, 1971.

[24] R. G. Marguta, E. M. del Río, and E. de Miguel, “Revisiting McMillan’s theory of the smectic A phase,” *J. Phys.: Condens. Matter*, vol. 18, p. 10335, 2006.

[25] B. D. Swanson, H. Stragier, D. J. Tweet, and L. B. Sorensen, “Layer-by-layer surface freezing of freely suspended liquid-crystal films,” *Phys. Rev. Lett.*, vol. 62, pp. 909–912, 1989.

[26] O. M. Roscioni, L. Muccioli, R. G. D. Valle, A. Pizzirusso, M. Ricci, and C. Zannoni, “Predicting the anchoring of liquid crystals at a solid surface: 5-cyanobiphenyl on cristobalite and glassy silica surfaces of increasing roughness,” *Langmuir*, vol. 29, pp. 8950–8958, 2013.

[27] A. Pizzirusso, R. Berardi, L. Muccioli, M. Ricci, and C. Zannoni, “Predicting surface anchoring: molecular organization across a thin film of 5CB liquid crystal on silicon,” *Chem. Sci.*, vol. 3, pp. 573–579, 2012.

[28] M. Fukuto, O. Gang, K. J. Alvine, B. M. Ocko, and P. S. Pershan, “Wetting of liquid-crystal surfaces and induced smectic layering at a nematic-liquid interface: An X-ray reflectivity study,” *Phys. Rev. E*, vol. 77, p. 031607, 2008.

[29] F. Picano, P. Oswald, and E. Kats, “Disjoining pressure and thinning transitions in smectic-A liquid crystal films,” *Phys. Rev. E*, vol. 63, p. 021705, 2001.

[30] P. G. De Gennes, “Interactions between solid surfaces in a presmectic fluid,” *Langmuir*, vol. 6, no. 9, pp. 1448–1450, 1990.

[31] W. H. de Jeu, “Structure and fluctuations of smectic membranes,” *Rev. Mod. Phys.*, vol. 75, pp. 181–235, 2003.

[32] T. Stoebe, P. Mach, and C. C. Huang, “Unusual layer-thinning transition observed near the smectic-A–isotropic transition in free-standing liquid-crystal films,” *Phys. Rev. Lett.*, vol. 73, no. 10, pp. 3587–3590, 1994.

[33] T. Kranjc and S. Zumer, “Layer-thinning transitions near the smectic-A-isotropic transition in liquid-crystal films,” *J. Chem. Phys.*, vol. 105, pp. 5242–5245, 1996.

[34] M. S. S. Pereira, M. L. Lyra, and I. de Oliveira, “Field-induced layer thinning transition on free-standing smectic films,” *Phys. Rev. Lett.*, vol. 103, p. 177801, 2009.

Chapter 6

Development of a polarizable force field for 4-n-pentyl-4'cyanobiphenyl

6.1 Introduction

Current-generation force fields for molecular dynamics simulations, such as OPLS[1,2], CHARMM[3], AMBER[4], MMFF[5], GROMOS[6] employ fixed charges, pairwise additive models to describe the interaction between atoms and molecules. While treating the electrostatic interactions in terms of fixed, atom-centered charges may be appropriate for low-dielectric constant mediums, real physical systems polarize strongly when placed in a high-dielectric medium like water. To implicitly incorporate the effect of polarization in static charge force fields, a common method is to fit partial charges to quantum-mechanically calculated electrostatic potentials that are, however, known to overestimate molecular dipole moments, such as the Hartree-Fock one. The resulting partial charges will be enhanced as they were computed for the gas phase and thus are intended to reproduce the effect of electronic polarization in the condensed phase. While this approximation may hold true for homogeneous systems like bulk phases, it fails to describe the molecular behaviour in the

proximity of interfaces between phases with different dielectric properties. Also, static charges FF provide a poor description of systems under the presence of electric fields, where the effects of molecular polarization and induced dipoles become relevant. These are typical scenarios for LC commercial applications, as in display devices where LC molecules are aligned by means of an electric field, or recently in the development of biosensors[7,8], where LC are interfaced with water and exposed to the presence of charged species such as ions that generate weak electric fields. Atomistic modeling of these systems could lead to a better, rational design of these devices, revealing more details on the mechanisms and phenomena lying behind their functioning at the molecular level of detail. In order to do so, a proper modeling of the involved chemical species is necessary, and the use of polarizable force field is of course the natural choice for this kind of challenge. While many polarizable FFs for water[9], alcohols[10,11], ethers[12], biological molecules such as nucleic acids[13] and lipids[14], and also inorganic species like ions[15] have been recently developed, an atomistic force field for the LC phase is still missing in literature to our knowledge. Here, we wish to develop the first polarizable force field for the popular LC 4-n-pentyl-4'cyanobiphenyl (5CB). This would allow a more realistic simulation of LC interfaces as well as a better reproduction of the effects of electric field on the LC phase. The FF will be developed employing the common shell model, also know as Drude oscillator model, by targeting relevant properties such molecular polarizability, density, bulk orientational order parameter, diffusion and dielectric constant.

6.2 Theory and methods

Model

The force field developed here is closely related to the previous non polarizable version reported in reference[16]. Also in this case, the molecule has been modeled at the united atom level of detail, thus hydrogen and carbon atoms in each

terminal methyl, phenyl and methylene bridge have been treated as a single interaction center. As for the description of inter and intra molecular interaction, we employed the classical and relatively simple AMBER-like functional form of the potential[17]:

$$\begin{aligned} U_{total} &= \sum_{bonds} K_r(r - r_{eq})^2 + \\ &\quad \sum_{angles} K_\theta(\theta - \theta_{eq})^2 + \\ &\quad \sum_{dihed} \sum_{n=0}^{6} V_n \left[1 + \cos(n\phi + \gamma)\right] + \\ &\quad \sum_{atoms}^{i<j} \left\{ 4\sqrt{\epsilon_i \epsilon_j} \left[\left(\frac{\sigma_i + \sigma_j}{2r_{ij}} \right)^{12} - \left(\frac{\sigma_i + \sigma_j}{2r_{ij}}^{6} \right) \right] + U_{elec} \right\} \end{aligned} \tag{6.1}$$

Due to the explicit treatment of induced polarization effects, the electrostatic term U_{elec} is slightly more complex than the typical Coulomb interaction term included in classic static charge functional form. According to the classical Drude oscillator model, the description of the induced polarization has been introduced by attaching an almost massless charged particle (the “shell”) to each polarizable atom (“core”). The electrostatic term U_{elec} in Equation 6.1 thus can be expressed as:

$$\begin{aligned} U_{elec} &= \sum_{i<j}^{N} \frac{q_i q_j}{(r_i - r_j)} + \sum_{i<j}^{N,N_D} \frac{q_{i,D} q_j}{(r_{i,D} - r_j)} + \\ &\quad \sum_{i<j}^{N_D} \frac{q_{i,D} q_{j,D}}{(r_{i,D} - r_{j,D})} + \frac{1}{2} \sum_{i}^{N_D} k_D (r_{i,D} - r_i)^2 \end{aligned} \tag{6.2}$$

Each atom then comprises two sites, a positively charged core with charge $q^{atom} - q_D^{atom}$ and a Drude particle of mass 0.4 amu carrying a negative charge q_D^{atom}. The small mass assigned to the Drude particle is necessary to allow the use of a computationally inexpensive dual-Langevin scheme for the relaxation of the Drude particle positions between each integration step, in order

to minimize the Coulomb interactions[18]. This technique allows to avoid the computationally expensive self-consistent field regime[19]. As in other recent polarizable models for several diverse compounds[9,12,15,20,21], the spring force constant was set to k_D = 1000 kcal. The huge magnitude of the spring force constant k_D is chosen to ensure a very short displacement between the Drude particle and the core atom, in order to satisfy the point-dipole approximation for the induced dipole associated with the atom-Drude pair. The induced dipole arising from the displacement of the Drude particle is defined as $q_D^2\mathbf{E}/k_D$, with q_D^2/k_D corresponding to the atomic polarizability α. The determination of the atomic polarizabilities for the parametrization of the force field can therefore be reduced to the determination of partial charges on the Drude particle-core atom pairs in a single step.

As typically done for standard static charge FF, Interaction between 1–2 and 1–3 core charges pairs are neglected as they are included in the bonding term of the potential energy function. Interactions of the Drude oscillators with core charges are not computed for 1–2 and 1–3 pairs while those between Drude oscillators of adjacent atoms are included but shielded by the so-called Thole damping function[22,23] S_{ij}, which reads:

$$S_{ij}(r_{ij}) \quad = \quad 1 - \left(1 + \frac{(a_i + a_j)r_{ij}}{2(\alpha_i\alpha_j)^{1/6}} e^{-(a_i+a_j)r_{ij}/(\alpha\ _i\alpha_j)^{1/6}}\right) \tag{6.3}$$

where r_{ij} is the distance between the Drude particle and 1-2 or 1-3 core atoms, α_i and α_j are the values of the atomic isotropic polarizabilities and a_i and a_j are the Thole damping parameters that regulate the strength of the damping function. A unique value for all the atoms of the Thole screening factor was also employed.

Parametrization strategy

The parametrization of the polarizable force field was carried out in three steps. First, we had to determine the optimal atomic polarizabilities that would lead to

a good reproduction of the ab-initio polarizability tensor. We initially performed an ab-initio geometry optimization of one 5CB molecule in vacuum, from which the output geometry was used as input for the determination of the atomic charges and of the polarizability tensor.

We then proceeded with the determination of the charges of the atom cores and Drude particles q_{core} and q_D, as they determine the polarizability of the atoms once the force k_D constant is specified. Starting values of polarizabilities were taken from reference[23] and were then manually tuned to reproduce the isotropic value and the anistropy of the molecular polarizability. To do so, we carried out short MD simulations at low temperature (10 K) on a single 5CB molecule. The coordinates of the atoms were the same of the ones obtained from ab-initio calculations and were not allowed to change during these simulations by keeping the core atoms fixed. LJ parameters for the atom cores were not altered from the previous non polarizable model at this stage, as their values do not influence the outcome of these simulations. In fact, Drude particles have null LJ parameters values and thus do not interact with atom cores. Several values for the Thole screening factor have been tested in order to find the one that best reproduces the anisotropy of the polarizability tensor.

Four simulations for each tentative set of charges were run: one where no external electric field was applied to the system, and other three where an electric field of the same intensity was applied in the x, y and z direction, respectively. This let us evaluate the induced dipole of the molecule exposed to the electric field and thus to derive the polarizability tensor. With this procedure, we computed the polarizability tensor for each tentative set of charges and iterated until agreement between the ab-initio values and the ones obtained from MD simulations was reached.

The second step in the development of the force field was the re-parametrization of the dihedral potentials. An accurate reproduction of the potential describing the interaction arising from torsional forces in LC molecules is of paramount importance, as they influence the overall shape of the molecule and thus have a major impact on the transition temperatures and phase behaviour of the result-

ing model. As very little experimental data exists for dihedral potentials, accurate potential profiles were obtained by running ab-initio scans of the potential energy upon change of the phenyl-phenyl, phenyl-alkyl and alkyl-alkyl dihedral angles. Parameters of the dihedral angles were then adjusted to reproduce the obtained ab-initio data in our molecular mechanics force field. To do so, we simulated an isolated 5CB molecule and scanned the potential energy of the dihedral angles through Adaptive Biasing Force (ABF) calculations[24,25]. As the thermalization of a single isolated molecule can be cumbersome due to risk of encountering the so called "flying ice cube" problem[26], we preferred to run the simulation in gas phase by adding a few Argon atoms to the simulation box, ensuring a better exchange of kinetic energy by frequent collisions with the target molecule. Once again, at this stage the Lennard Jones parameters were not altered from the previous non polarizable model, even though contribution of the Van der Waals forces on the dihedral angles might be not negligible. The potential profiles obtained from the ABF scans were then fitted in order to find the parameters that best reproduce the ab-initio potentials. Several iterations were necessary to obtain the final set of parameters.

The last step involved the tuning of the Lennard Jones parameters. We started from the AMBER force field parameters and modified them to reproduce the experimental values for the density, orientational order parameter and diffusion as a function of temperature.

Computational Details

All QM calculations were performed using the Gaussian 03 program[27]. The geometry optimization, the determination of charges and of the polarizability tensor were carried out using the PBE0 hybrid functional[28] with triple z basis set (PBE1PBE//TZVP keyword). The effective charges on each atom were computed through the common ESP method), where a least squares fitting algorithm is used to derive a set of atom-centered point charges which best reproduce the electrostatic potential of the molecule. Polarizability was obtained

by specifying the keyword “Polar” in the Gaussian 03 input, so that the program outputs both the isotropic value of polarizability and the polarizability tensor components.

All MD simulations in this work were performed with NAMD engine[29] versions 2.9 and 2.10. NAMD employs the Brunger-Brooks-Karplus method, which is an extension of the Verlet algorithm, for the integration of the Langevin equations. NVT MD simulations for the determination of the optimal charges of core and Drude particles were run on a single 5CB molecule for a total simulation time of 10 ps (Δt = 0.1 fs), which is enough for allowing the relaxation of the position of Drude particles. Temperature was kept at 10 K, through use of the dual stochastic Langevin thermostat, with Drude bond temperature set to 1 K and a damping factor of 1 ps^{-1}. Core atoms were kept fixed at the geometry employed for ab-initio calculations. A quartic restraining potential (with $k_D = 40000$) on the Drude bond length was applied if its length exceeded 0.2 Å. The cutoff radius for the Lennard-Jones interactions was set to 10 Å, with the switching function taking effect at 9.5 Å, while the pair list was maintained for atoms within 13 Å and updated every 20 steps.

MD simulations for the determination of the dihedral potential profiles were run with a timestep Δt of 0.1 fs at a temperature T=300 K and for a simulation time of 10 ns each. The simulated system comprised a single 5CB molecule in 100 argon atoms with a cubic cell with side of 100 Å. The scans of the dihedral potential profiles were carried out using the Adaptive Biasing Force method implemented in NAMD with a resolution of 1 degree and estimating the average force in each bin over 10000 samples.

MD simulations for the determination of Lennard-Jones parameters were run on samples of N=250 5CB molecules in a range of temperature between 295 and 320 K. Integration timestep Δt was set to 1 fs (half of the one used for the non polarizable FF), three-dimensional periodic boundary conditions were used and long range electrostatic interactions were computed through the Particle Mesh Ewald method[30]. Samples were kept at constant pressure through the Berendsen barostat[31] and the cell sides were allowed to fluctuate isotropically

during the simulation. A starting configuration for all the temperatures was generated through the Packmol program[32] and equilibrated at 320 K in order to start from a orientationally disordered system.

6.3 Force Field parametrization

Ab-initio and Drude model polarizability

Atomic polarizabilities and the resulting charges (see Table 6.2) have been tuned with the following criterion apt to increase the molecular polarizability anisotropy: atoms lying on the main inertia axis of the 5CB phenyl core (N1, C2, C3 C6, C9 and C12) have been given higher values while the remaining aromatic carbons were made less polarizable. Atomic polarizabilities for the carbon atoms in the alkyl chain were not altered from reference[33]. Several values for the Thole screening factor were tried, and we found that setting it to 0.8 for all atom lead to the best reproduction of the anisotropy of the polarizability tensor.

Isotropic value of the molecular polarizability α_{iso} were obtained as the trace of the tensor while the anisotropy ε was computed as:

$$\varepsilon = \frac{\alpha_{xx} - \frac{1}{2}(\alpha_{yy} + \alpha_{zz})}{\alpha_{xx} + \alpha_{yy} + \alpha_{zz}} \tag{6.4}$$

Ab-initio and Drude model polarizability tensors, as well as the isotropic value and anisotropy of the molecular polarizability are reported in Table 6.1. It can be seen that the values of the diagonal elements obtained with the Drude model are close to the ab-initio values, and also the order of their magnitude is respected. This leads to values of isotropic polarizability and anisotropy very close to the ones obtained from ab-initio computations. The value of α_{iso} of our model, of 216.5 Bohr^3, is also very close to the experimental one of 220.06 Bohr^3 [34].

	α_{xx}	α_{yx}	α_{zx}
α_{xx}	363.5	13.3	18.1
α_{xy}	13.3	175.8	-13.3
α_{xz}	18.1	-13.3	141.2
α_{iso}	226.8		
ε	0.301		

	α_{xx}	α_{yx}	α_{zx}
α_{xx}	345.2	6.7	8.7
α_{xy}	6.5	159.8	-2.8
α_{xz}	8.4	-2.8	144.5
α_{iso}	216.5		
ε	0.297		

Table 6.1: On the left, polarizability tensor from ab-initio computations. On the right, optimized polarizability tensor from the Drude polarizable model with the charges reported in Table 6.2.

atom name	$q_{atom}(e)$	α (a_0)	$q_{core}(e)$	$q_D(e)$
N1	-0.689852	1.300000	+1.288773	-1.978625
C2	0.964540	2.500000	+3.708399	-2.743859
C3	-1.010128	2.500000	+1.733731	-2.743859
C4	0.286636	1.500000	+2.412020	-2.125384
C8	0.296844	1.500000	+2.422228	-2.125384
C5	0.228056	1.500000	+2.353440	-2.125384
C7	0.211004	1.500000	+2.336388	-2.125384
C6	-0.293712	2.500000	+2.450147	-2.743859
C9	-0.429548	2.500000	+2.314311	-2.743859
C10	0.184556	1.500000	+2.309940	-2.125384
C14	0.197316	1.500000	+2.322700	-2.125384
C11	0.273064	1.500000	+2.398448	-2.125384
C13	0.265292	1.500000	+2.390676	-2.125384
C12	-0.861300	2.500000	+1.882559	-2.743859
C15	0.373056	2.500000	+3.116915	-2.743859
C16	0.043848	1.660000	+2.279714	-2.235866
C17	-0.071572	1.660000	+2.164294	-2.235866
C18	0.042224	1.660000	+2.278090	-2.235866
C19	-0.010208	1.810000	+2.324492	-2.334700

Table 6.2: Final values of the atomic charge q_{atom}, atomic polarizability α, atom core charge q_{core} and the respective Drude particle charge q_D for the 5CB polarizable molecule with a Thole screening factor of 0.8.

Dihedral parametrization

Potentials for the three dihedral angles in the molecule can be found in Figure 6.1. In each plot we report the ab-initio results of the potential scan (again with G03 using a PBE0 hybrid functional with triple z basis set), the potential applied in the force field and the resulting dihedral potential shape. The parameters for the three angles can be found in Table 6.3. It can be seen that the ab-initio potentials are well reproduced by the newly parametrized force field with only minor deviations for the phenyl-alkyl angle.

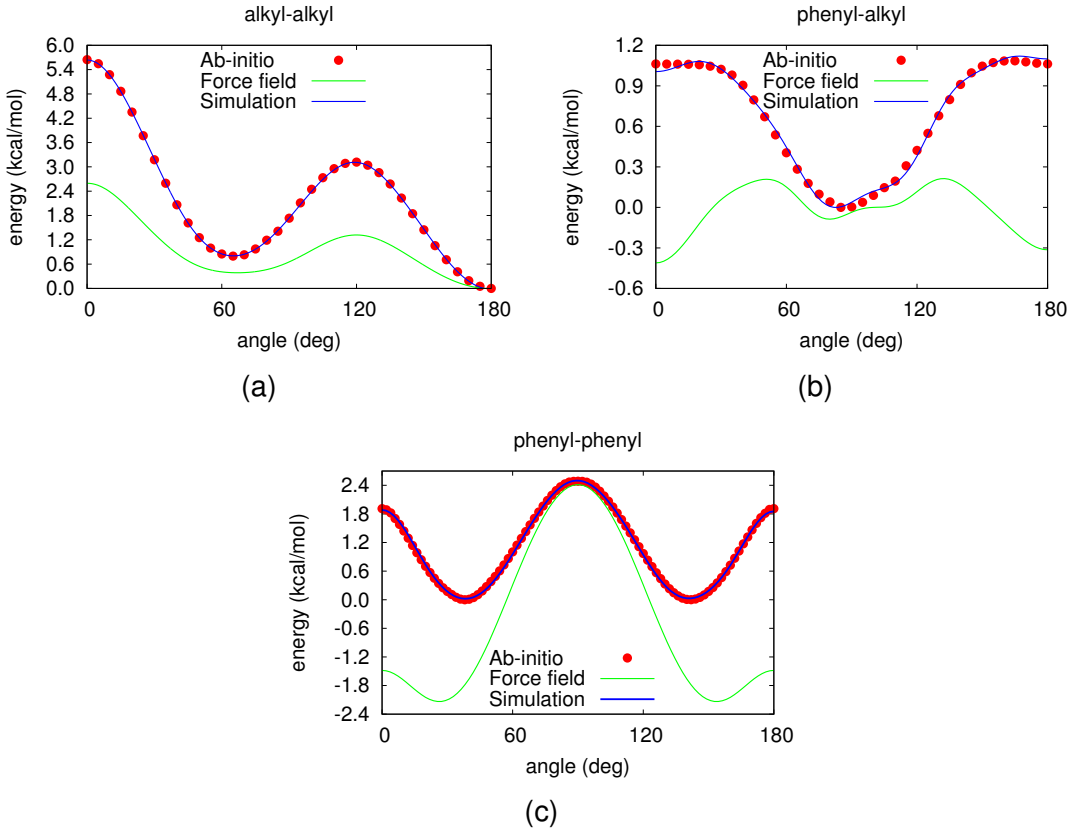

Figure 6.1: Dihedral potential profiles for the re-parametrized dihedral angles. Red points represent the profile obtained through ab-initio PBE0/TZVP calculations, green line is the potential applied in the force field and the blue line is the effective potential felt by atoms resulting from the sum of the dihedral potential and VdW and charge interactions with neighbouring atoms and Argon atoms.

atom types	K_ϕ (kcal/mol)	n	delta (°)	dihedral description
X CD CD X	14.4000	2	180	aromatic with implicit hydrogen
X CD CG X	7.2000	2	180	aromatic with a single implicit hydrogen
NY CY CG CD	0.0000	1	180	free rotation around CN group
X CG CG X	-0.5910	2	0	rotation around phenyl-phenyl bond
X CG CG X	0.2745	4	0	
X CG CG X	0.0536	6	0	
X CG CG X	0.0134	8	0	
X CM CM X	0.0764	1	0	rotation around aliphatic carbons
X CM CM X	1.5700	3	0	
X CM CM X	0.0725	4	0	
X CM CM X	0.0592	5	0	
X CM CM X	0.0722	6	0	
X CG CM X	-0.0594	2	0	rotation around phenyl-alkyl bond
X CG CM X	-0.1012	4	0	

Table 6.3: Dihedral parameters for the polarizable 5CB molecule. K_ϕ is the dihedral force constant in kcal/mol, n is the multiplicity, delta is the phase. X symbol in the atom type column represents any atom linked to the previous or following atom type.

Lennard Jones parametrization

The assessment of the right set of LJ parameters is of paramount importance as a proper description of the interaction potential between atom types deeply influences the reproduction of fundamental ensemble properties. Here, we started from the widely used AMBER UA force field[4], which we reparametrized aiming to reproduce some target experimental properties such as density and ordering transition temperatures. Several sets of tentative parameters have been tested by running MD simulation at least 100 ns long on systems made of N=250 5CB molecules. The final set of parameter is reported in Table 6.4 together with the original AMBER parameters. It is not surprising that the optimal epsilons are strongly reduced with respect to the original ones for non-polarizable force fields. In fact, with the introduction of Drude particles, a substantial part of the van der Waals interactions is now explicitly described by the electrostatic ones, and then it should be subtracted from the generic Lennard-Jones term to avoid double counting. The small increase in van der Waals radii is instead justified by a corresponding decrease of the effective atomic radius due to the large charges present on core and shell particles.

atom type	ε_{AMBER}	ε_{mod}	σ_{AMBER}	σ_{mod}
CM	-0.1094	-0.0656	2.058	2.072
CG	-0.0860	-0.0516	1.908	1.921
CD	-1.1114	-0.0668	1.996	2.009
CQ	-0.1494	-0.0896	2.058	2.072
CY	-0.2100	-0.1260	1.908	1.921
NY	-0.1700	-0.1020	1.824	1.836
rescaling		0.60		1.0066

Table 6.4: Original LJ parameters ε_{AMBER}, σ_{AMBER} and final reparametrized values for polarizable 5CB ε_{mod}, σ_{mod}.

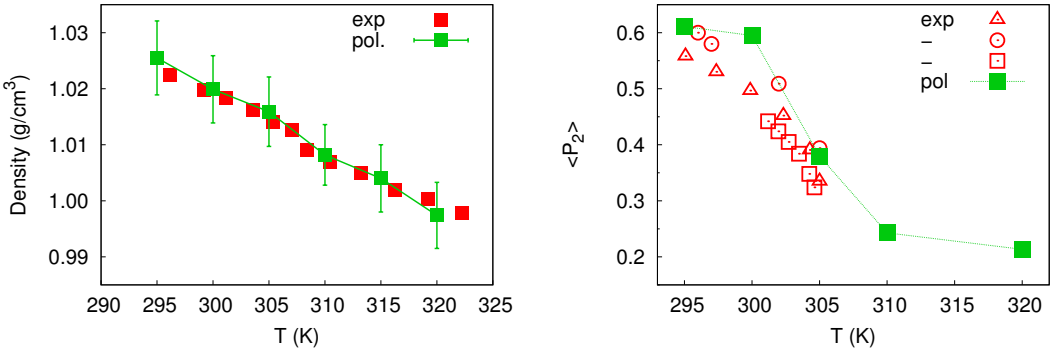

(a) (b)

Figure 6.2: On the left, values of density for the experimental and the simulated sample with polarizable 5CB molecules as a function of the temperature T. On the right, second rank orientational order parameter $\langle P_2 \rangle$ (see Chapter 3) as a function of the temperature for the simulated sample, compared with experimental data obtained through several techniques[35–39].

In Figure 6.2 we report the comparison between experimental and simulated target properties (with the final set of LJ parameters) density, second rank orientational order parameter $\langle P_2 \rangle$ (see Chapter 3) of 5CB as a function of the temperature. It can be seen that regardless of the small size of the samples, the new polarizable model for 5CB reproduces very well all the three target properties, yielding a very accurate density profile (less than 1% error at the extremes of the temperature range), a correct nematic-isotropic transition temperature at about 305 K and diffusion coefficients very close to the experimental ones.

6.4 Force Field validation

Here we report the result obtained from a serie of simulations on a sample made of 750 5CB molecules. MD runs were carried out employing the same parameters reported for the N=250 sample used in the parametrization of LJ parameters.

Density

In Figure 6.3 we report the density of the polarizable and non polarizable 5CB as a function of the temperature against the experimental data[40]. It can be seen that the simulation results closely follow the experimental values, with a discrepancy which is lower than 1% at the extremes of the simulated temperature range.

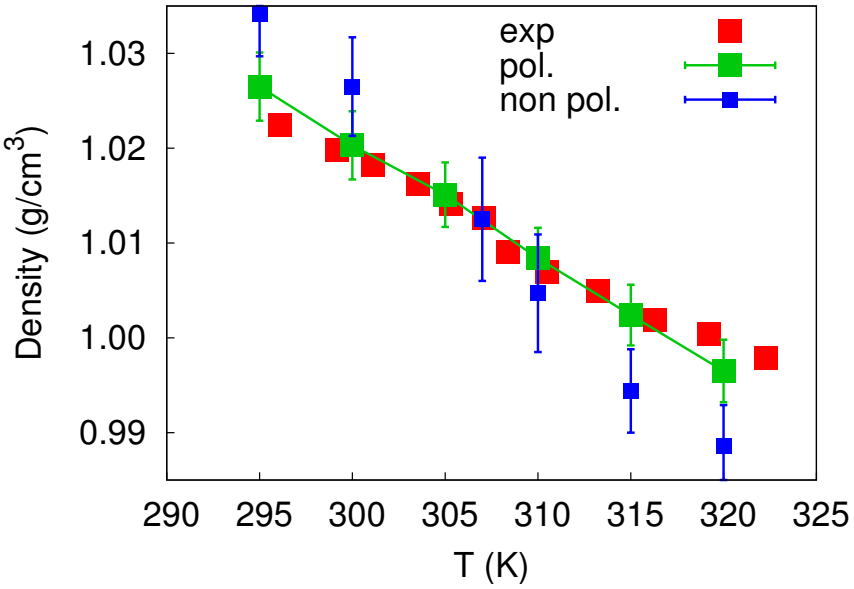

Figure 6.3: Comparison between simulated results from both the polarizable and non polarizable models (in green and blue, respectively), and experimental 5CB mass density (red).

Orientational order

In Figure 6.4 we report several snapshots of the sample at different temperatures, where molecules are color coded according to their orientation. It can be seen that under 305 K the orientation of the molecules is homogeneous, indicating that they are all oriented approximately in the same direction and thus suggesting the presence of a nematic phase. At T > 305 K, it can be noticed that the orientation of the molecules is random, suggesting that above that temperature the sample is isotropic. Thus we can conclude that the nematic-isotropic transition temperature (T_{NI}) for the 5CB polarizable model is approxi-

mately between 305 and 310 K, in very good agreement with the experimental T_{NI} of 305 K.

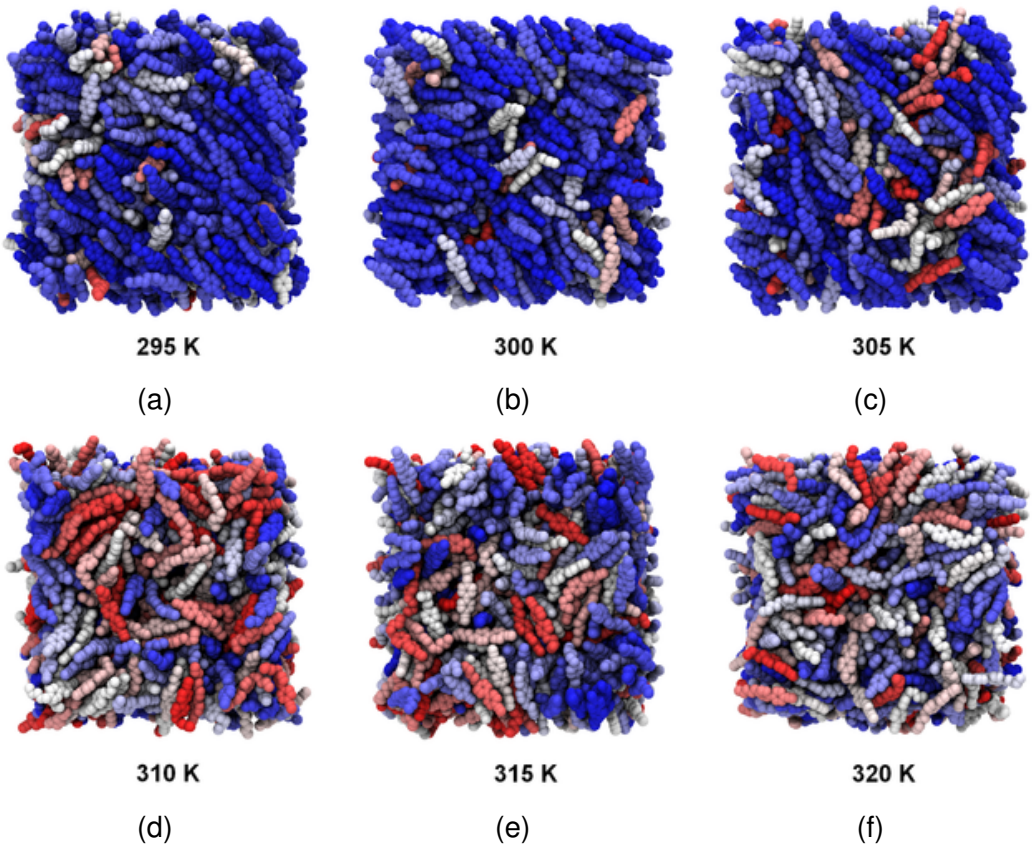

Figure 6.4: Snapshots of the simulated sample of polarizable 5CB at increasing temperature. Molecules are color-coded according to their orientation (blue: parallel to the director, red: perpendicular).

The transition from the nematic phase to the isotropic can be more carefully appreciated by studying the second rank orientational order parameter $P_2(\cos\beta)$, where β is the angle between molecules and the phase director, computed as reported in Chapter 3, following the common procedure for liquid crystals[41]. In Figure 6.5a we report the evolution of $P_2(t)$, which is the value of the instantaneous order parameter for each configuration plotted against the simulation time. It can be seen that samples at temperature T < 305 K show a constant high value of P_2, around 0.6, suggesting the presence of a stable nematic phase. On the other hand, samples at T > 305 K feature isotropic values (P_2 < 0.3) through all the simulation time, indicating the lack of orientational order and thus the presence of a isotropic phase. At T = 305 K it can be seen

that $P_2(t)$ oscillates between high and low values of P_2, a common behaviour found at the transition temperature[42]. The influence of the temperature on the orientational order of 5CB can be better studied by plotting $\langle P_2 \rangle$, i.e. the value of the configurational average of P_2. $\langle P_2 \rangle$ is reported as a function of temperature in Figure 6.5b and against the experimental data obtained from several techniques[35–39]. Error bars for the simulated data represent the standard deviation of the average P_2. It can be seen that the results obtained for the polarizable 5CB accurately describe the average trend of the experimental data, with high values of $\langle P_2 \rangle$ close to 0.6 at low temperatures, indicating the presence of a nematic LC phase, a phase transition at about 305 K and a isotropic phase at T > 310 K, as denoted by the low value of $\langle P_2 \rangle$ of approximately 0.1.

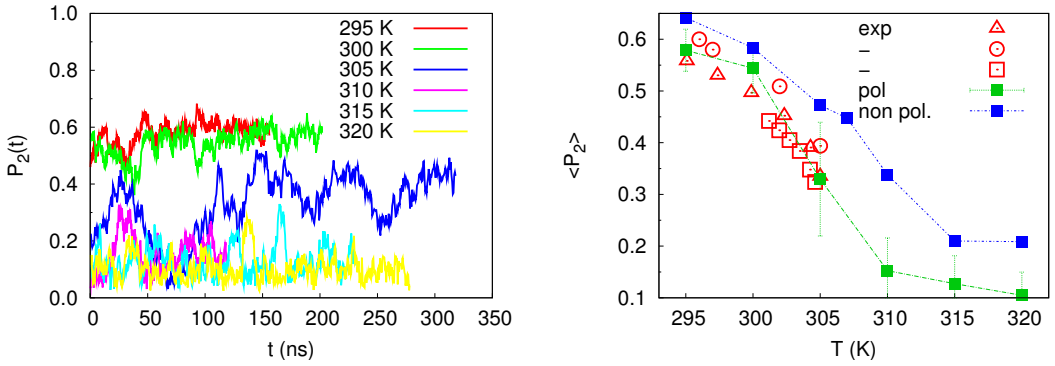

(a) (b)

Figure 6.5: Figure a: trend of instantaneous $P_2(t)$ as a function of trajectory time for all the simulated temperatures. Figure b: Average simulated order parameters $\langle P_2 \rangle$ for the inertia tensor axis of 5CB as a function of temperature. $\langle P_2 \rangle$ for both the non polarizable[16] and polarizable model are reported in green and blue, respectively, and plotted against data obtained from several experimental techniques[35–39] (in red).

Pair correlations

In order to inspect the local structure of 5CB liquid phase, we computed the pair radial distribution function $g_0(r)$, which describes the relative variation of the density as a function of the distance from a reference particle:

$$g_0(r) \quad = \quad \frac{1}{4\pi r^2 \rho_N} \left\langle \delta(r - r_{IJ}) \right\rangle_{IJ} \tag{6.5}$$

where r_{ij} is the distance between the center of mass of the i and j molecules.

In Figure 6.6a we report $g_0(r)$ for the samples of polarizable 5CB at several temperatures. Common to all of them is the presence of a first peak at $\sim$ 6 Å, corresponding to the presence of a first coordination shell. The peak is much higher at low temperatures though, suggesting a more organized local structure for the nematic phase. The LC phase features the presence of further short range structures, as denoted by the two peaks at 10 and 14 Å. These two peaks disappear at higher temperatures merging into a single, large peak. Beyond 15 Å, it can be seen that $g_0(r)$ tends to the asymptotic value of 1, a common feature for liquid phases indicating the absence of long range ordering. In Figure 6.6b we also compare $g_0(r)$ of the nematic and isotropic phases for both samples of polarizable and non polarizable 5CB. Both samples feature a similar local structure, with the presence of the first peak at 6 Å and the two long range peaks at 10 and 14 Å. Such organization is remarkably more pronounced for the polarizable force field, with the height of the first peak being about 30% times higher than the non polarizable one.

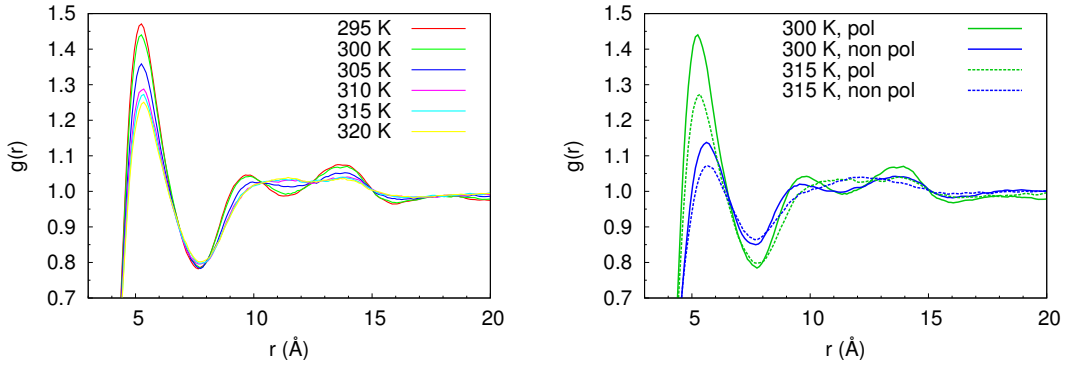

(a) (b)

Figure 6.6: Figure 6.6a: radial distribution function $g_0(r)$ (Equation 6.5 for samples composed of polarizable 5CB molecules at different temperatures. Figure 6.6b: $g_0(r)$ in the nematic (300 K) and isotropic (315 K) phases for samples composed by polarizable e non polarizable 5CB molecules.

To analyze the dipole organization in the LC phase, we have evaluated the first and second rank orientational distribution functions, $G_1^{\mu}(r)$ and $G_2^{\mu}(r)$, which were obtained by choosing the electric dipole unit vectors $\hat{\mu}_I, \hat{\mu}_J$ as reference:

$$G_1^{\mu}(r) = \langle \delta(r - r_{ij})(\hat{\mu}_i \cdot \hat{\mu}_j) \rangle_{ij} / \langle \delta(r - r_{ij}) \rangle_{ij} \tag{6.6}$$

$$G_2^{\mu}(r) = \langle \delta(r - r_{ij}) \left[\frac{3}{2}(\hat{\mu}_i \cdot \hat{\mu}_j)^2 - \frac{1}{2} \right] \rangle_{ij} / \langle \delta(r - r_{ij}) \rangle_{ij} \tag{6.7}$$

where r_{ij} is now the distance between the charge centres of the i and j molecules.

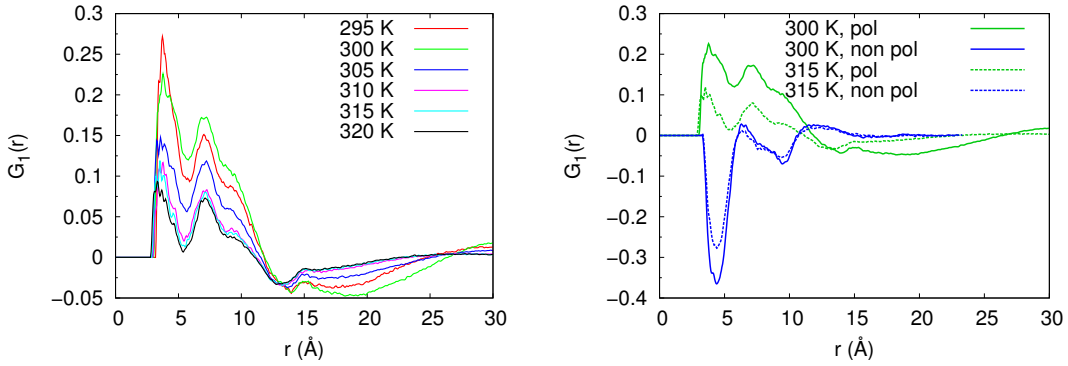

(a) (b)

Figure 6.7: Figure 6.7a: first rank orientational distribution function $G_1^{\mu}(r)$ (Equation 6.6) for samples of polarizable 5CB at different temperatures. Figure 6.7b: comparison between the $G_1^{\mu}(r)$ of nematic and isotropic phases of both polarizable and non polarizable 5CB samples.

In Figure 6.7a the $G_1^{\mu}(r)$ for samples of polarizable 5CB is reported at different temperatures. The trend for all temperature shows that, quite surprisingly, dipoles are more likely to be oriented in the same direction at short range, as suggested by the presence of two positive peaks within 10 Å. Such alignment becomes less pronounced as the temperature is raised, in agreement with the isotropic nature of the LC phase above 305 K. At long range, the orientation of the dipoles becomes random for both nematic and isotropic samples, with $G_1^{\mu}(r)$ tending to 0. The behaviour of the polarizable 5CB in terms of dipole orientation is at variance with the one found for the non polarizable 5CB model in both nematic and isotropic phases, as highlighted by the negative peak at 4 Å in Figure 6.7b.

This result might be deceiving as one could think that indeed molecules of polarizable 5CB align in a parallel fashion at short range. It must be specified, though, that while for the non polarizable 5CB the dipole orientation coincides with the orientation of the molecule, the same cannot be said for the polarizable model. In fact, it could be that while the permanent dipoles are antiparallel, this might not be the case for the induced ones. To test this assumption, we chose the CN bond as reference (since the core of the 5CB molecule is rigid and the permanent dipole is collinear with the CN bond) and computed the trend of the P_1^{CN} as a function of, in this case, the distance between two CN bonds (Figure

6.8).

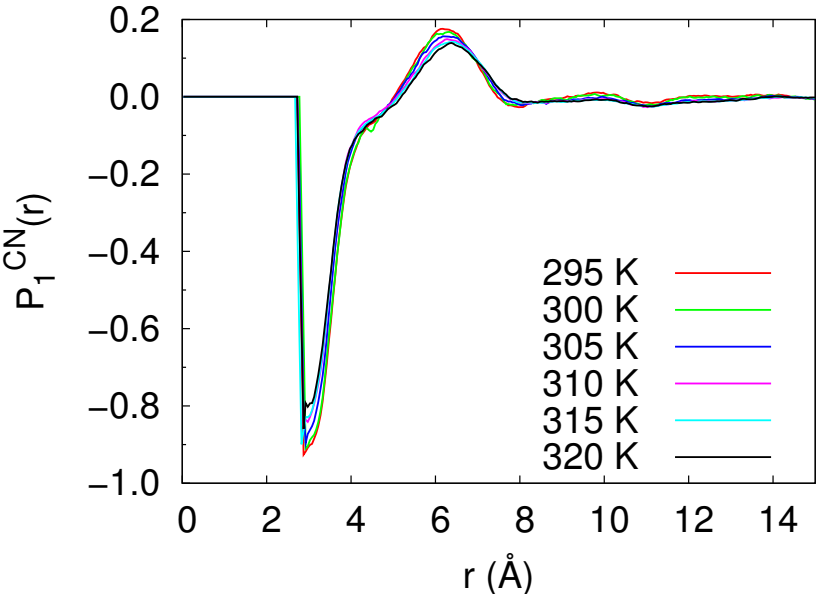

Figure 6.8: First rank orientational distribution function for the CN bond $P_1^{CN}(r)$ for samples of polarizable 5CB at different temperatures.

It can be seen for all temperatures that at short range, between 2 and 5 Å from the reference CN bond, the first neighbouring molecules are oriented in an antiparallel fashion, thus yielding negative values of $P_1^{CN}(r)$. A region with a positive peak of $P_1^{CN}(r)$ follows between 5 and 8 Å, as molecules lying in the next coordination shell are parallel to the reference molecule, in order to maximize the interaction with the antiparallel molecules in the first region. It can also be noted that the intensity and shape of both the negative and positive peaks remain almost unchanged as the temperature is raised. At larger r, the orientation of the molecules becomes again random for both nematic and isotropic samples, with $P_1^{CN}(r)$ tending to 0. These results confirm that polarizable 5CB molecules still align antiparallel to each other at short range, in agreement with the results obtained for the non polarizable 5CB, but that the total dipoles of the molecules are instead slightly parallel to each other, perhaps due to the orientation of the induced dipole.

In Figure 6.9a the $G_2^{\mu}(r)$ for samples of polarizable 5CB is reported at different temperatures. $G_2^{\mu}(r)$ shows the relative P_2 of molecules in respect of the

orientation of a reference molecule as a function of the intermolecular distance.

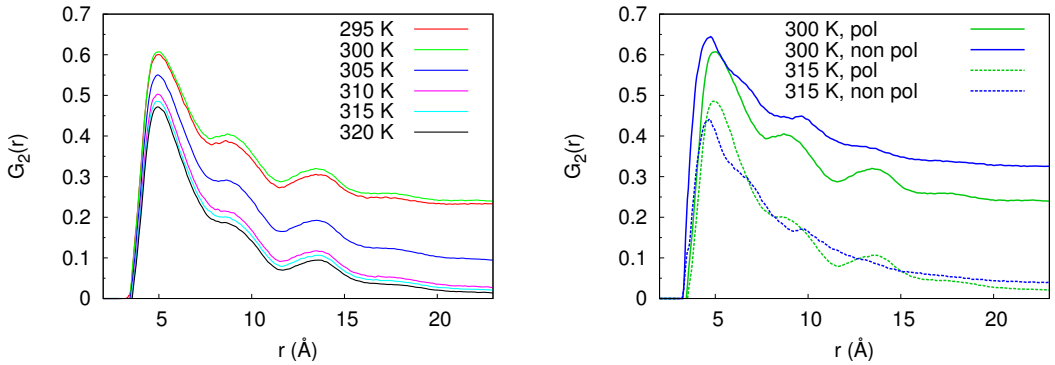

(a) (b)

Figure 6.9: Figure 6.9a: second rank orientational distribution function $G_2^{\mu}(r)$ (Equation 6.7) for samples of polarizable 5CB at different temperatures. Figure 6.9b: comparison between the $G_2^{\mu}(r)$ of nematic and isotropic phases of both polarizable and non polarizable 5CB samples.

At $r \sim 5$ Å, $G_2^{\mu}(r)$ features a peak representing the short range orientational order arising from the molecular packing. Figure 6.9a shows the presence of two further orientational coordination shells (plateaus at 9 and 13 Å), after which the order parameter decreases asymptotically to the value of $\langle P_2 \rangle^2$ of the phase. Peaks at 5, 9 and 13 Å are also found to a lesser extent in the isotropic phase, even though the value of P_2 is of course lower. The trend of $G_2^{\mu}(r)$ can be again compared between the polarizable and non polarizable 5CB samples in Figure 6.9b. It can be noted that samples composed of non polarizable 5CB molecules, while possessing a higher absolute order in the nematic phase, feature less pronounced orientational coordination shells, thus with a $G_2^{\mu}(r)$ decaying more smoothly to the value of $\langle P_2 \rangle^2$ of the phase. Nonetheless, the first peak representing the short range packing of molecules is found for both models at ~ 5 Å.

Experimentally, 5CB is found to show only a nematic phase at T < 305 K and a isotropic phase at higher temperatures. Thus we do not expect the presence of positional order in our simulated samples, and in order to test such statement we computed both the smectic and the hexagonal order parameters, both described in Chapter 3. In agreement with the experimental findings, both order parameters were found to be null both in the nematic and isotropic phase.

Translational diffusion

In Figure 6.10 we report the isotropic diffusion coefficient D_{iso} of the polarizable and non polarizable models as a function of the temperature, computed from the mean square positional displacements using the classical Einstein formula:

$$D_{ii} = \lim_{t\to\infty} \frac{\langle (R_i(0) - R_i(t))^2 \rangle}{2t}, \tag{6.8}$$

where R_i is the component of the molecular position vector of each molecule along the axis $i = x, y, z$ of the director frame, assuming that the asymptotic long time limit and the diffusive regime is reached for values of $t \gtrsim 10$ ns. While the trend of simulated data for both models is comparable to the experimental one[43], the absolute values for the polarizable 5CB are a factor two higher, which is a very good improvement compared to the ten times faster diffusion for the old non polarizable force field.

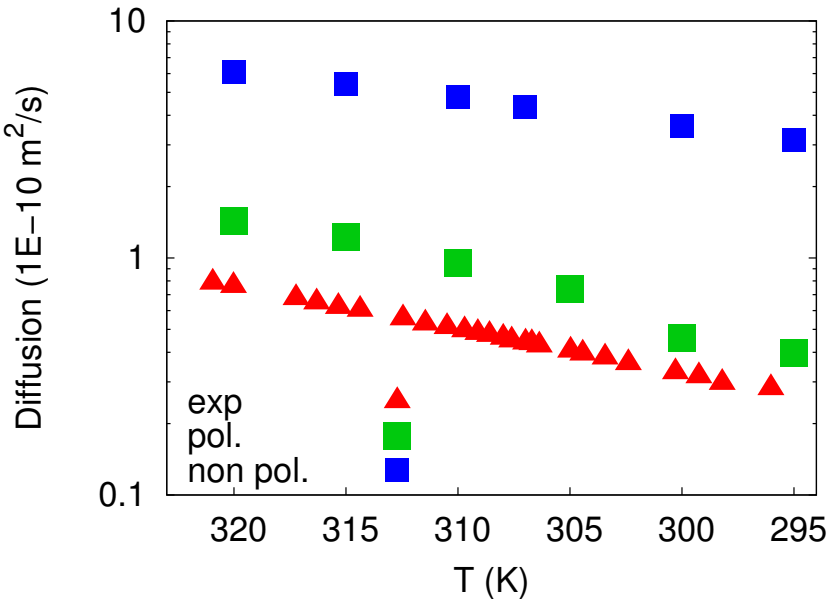

Figure 6.10: Isotropic diffusion coefficient D_{iso} of the polarizable and non polarizable models as a function of the temperature, plotted against the experimental values[43].

6.5 Conclusions

We have developed a new set of parameters for a polarizable, united-atom force field for the fifth homologue of the n-alkyl cyanobiphenyls family starting from non polarizable parameters of the popular AMBER FF and we have extensively validated it through molecular dynamics simulations. Explicit treatment of the polarization has been obtained through the use of the Drude oscillator model, and we reported a close agreement between the ab-initio values of isotropic polarizability and anisotropy and the ones obtained for our model.

We have shown that density, nematic-isotropic transition temperature, orientational order parameter, translational diffusion are in very good agreement with the experimental data available in literature. In particular, the present force field has shown a net improvement over the previous non polarizable force field, particularly in terms of translational diffusion, which is now only less than twice faster compared to the experimental one, against the almost ten times faster diffusion found for the non polarizable force field.

The absence of antiparallel alignment found in the first rank positional-orientational pair correlation function of the total dipole is still subject of investigation and longer simulations need to be performed to accurately evaluate the dielectric constant of the simulated samples.

More in general, we have shown that polarizable force fields might allow even more realistic simulations of liquid crystals phases, at the cost of a twofold increase of computational time. The higher computational requirements can be justified in favour of a better reproduction of interfacial phenomena and a more accurate description of LC behaviour in presence of charged species such as ions or more broadly speaking in presence electrical fields. The newly developed FF should be easily transferable to other homologues of the cyanobiphenyl serie through the reparametrization of the atomic charges only and could be tested to verify whether it is able to reproduce the odd-even effect and the smectic arrangement of molecules for 8CB.

Bibliography

[1] W. L. Jorgensen and J. Tirado-Rives, "The OPLS potential functions for proteins. energy minimizations for crystals of cyclic peptides and crambin," *J. Am. Chem. Soc.*, vol. 110, pp. 1657–1666, 1988.

[2] W. L. Jorgensen, D. S. Maxwell, and J. Tirado-Rives, "Development and testing of the OPLS all-atom force field on conformational energetics and properties of organic liquids," *J. Am. Chem. Soc.*, vol. 118, no. 45, pp. 11225–11236, 1996.

[3] A. D. MacKerel Jr., C. L. Brooks III, L. Nilsson, B. Roux, Y. Won, and M. Karplus, *CHARMM: The Energy Function and Its Parameterization with an Overview of the Program*, vol. 1, pp. 271–277. John Wiley and Sons: Chichester, 1998.

[4] J. Wang, R. M. Wolf, J. W. Caldwell, P. A. Kollman, and D. A. Case, "Development and testing of a general AMBER force field," *J. Comput. Chem.*, vol. 25, no. 9, pp. 1157–1174, 2004.

[5] T. A. Halgren, "Merck molecular force field. i. basis, form, scope, parameterization, and performance of MMFF94," *J. Comput. Chem.*, vol. 17, no. 5-6, pp. 490–519, 1996.

[6] N. Schmid, A. P. Eichenberger, A. Choutko, S. Riniker, M. Winger, A. E. Mark, and W. F. Van Gunsteren, "Definition and testing of the gromos force-field versions 54a7 and 54b7," *Eur. Biophys. J.*, vol. 40, no. 7, pp. 843–856, 2011.

[7] Y. Bai and N. L. Abbott, "Recent advances in colloidal and interfacial phenomena involving liquid crystals," *Langmuir*, vol. 27, no. 10, pp. 5719–5738, 2011.

[8] I. H. Lin, D. S. Miller, P. J. Bertics, C. J. Murphy, J. J. de Pablo, and N. L. Abbott *Science*, vol. 332, p. 1297, 2011.

[9] G. Lamoureux, E. Harder, I. V. Vorobyov, B. Roux, and A. D. MacKerell, "A polarizable model of water for molecular dynamics simulations of biomolecules," *Chem. Phys. Lett.*, vol. 418, no. 1-3, pp. 245–249, 2006.

[10] V. M. Anisimov, I. V. Vorobyov, B. Roux, and A. D. MacKerell, "Polarizable empirical force field for the primary and secondary alcohol series based on the classical Drude model," *J. Chem. Theory Comput.*, vol. 3, no. 6, pp. 1927–1946, 2007.

[11] X. He, P. E. M. Lopes, and A. D. MacKerell, "Polarizable empirical force field for acyclic polyalcohols based on the classical Drude oscillator," *Biopolymers*, vol. 99, no. 10, pp. 724–738, 2013.

[12] C. M. Baker and J. MacKerell, Alexander D., "Polarizability rescaling and atom-based Thole scaling in the CHARMM Drude polarizable force field for ethers," *J. Mol. Model*, vol. 16, pp. 567–576, 2010.

[13] C. M. Baker, V. M. Anisimov, and A. D. MacKerell, "Development of CHARMM polarizable force field for nucleic acid bases based on the classical Drude oscillator model," *J. Phys. Chem. B*, vol. 115, no. 3, pp. 580–596, 2011.

[14] J. Chowdhary, E. Harder, P. E. M. Lopes, L. Huang, A. D. MacKerell, and B. Roux, "A polarizable force field of dipalmitoylphosphatidylcholine based on the classical Drude model for molecular dynamics simulations of lipids," *J. Phys. Chem. B*, vol. 117, no. 31, pp. 9142–9160, 2013.

[15] H. Yu, T. W. Whitfield, E. Harder, G. Lamoureux, I. V. Vorobyov, V. M. Anisimov, A. D. MacKerrel Jr., and B. Roux, "A polarizable model of water for molecular dynamics simulations of biomolecules," *J. Chem. Theory Comput.*, vol. 6, pp. 774–786, 2010.

[16] G. Tiberio, L. Muccioli, R. Berardi, and C. Zannoni, "Towards in silico liquid crystals. realistic transition temperatures and physical properties for

n-cyanobiphenyls via molecular dynamics simulations," *ChemPhysChem*, vol. 10, pp. 125–136, 2009.

[17] S. J. Weiner, P. A. Kollman, D. A. Case, U. C. Singh, C. Ghio, G. Alagona, S. Profeta, and P. Weiner, "A new force field for molecular mechanical simulation of nucleic acids and proteins," *J. Am. Chem. Soc.*, vol. 106, pp. 765–784, 1984.

[18] W. Jiang, D. J. Hardy, J. C. Phillips, A. D. MacKerell, K. Schulten, and B. t. Roux, "High-Performance Scalable Molecular Dynamics Simulations of a Polarizable Force Field Based on Classical DRude Oscillators in NAMD," *J. Phys. Chem. Lett.*, vol. 2, pp. 87–92, 2010.

[19] G. D'Avino, L. Muccioli, C. Zannoni, D. Beljonne, and Z. G. Soos, "Electronic Polarization in Organic Crystals: A Comparative Study of Induced Dipoles and Intramolecular Charge Redistribution Schemes," *J. Chem. Theory Comput.*, vol. 10, pp. 4959–4971, Nov. 2014.

[20] V. M. Anisimov, G. Lamoureux, I. V. Vorobyov, N. Huang, B. Roux, and A. D. MacKerell, "Determination of Electrostatic Parameters for a Polarizable Force Field Based on the Classical DRude Oscillator," *J. Chem. Theory Comput.*, vol. 1, pp. 153–168, 2004.

[21] A. Savelyev and A. D. MacKerell, "All-atom polarizable force field for dna based on the classical Drude oscillator model," *J. Comput. Chem.*, vol. 35, pp. 1219–1239, 2014.

[22] B. Thole, "Molecular polarizabilities calculated with a modified dipole interaction," 1981.

[23] P. T. van Duijnen and M. Swart, "Molecular and atomic polarizabilities: Thole's model revisited," *J. Phys. Chem. A*, vol. 102, no. 14, pp. 2399–2407, 1998.

[24] E. Darve, D. Rodríguez-Gómez, and A. Pohorille, "Adaptive biasing force

method for scalar and vector free energy calculations," *J. Chem. Phys.*, vol. 128, no. 14, p. 144120, 2008.

[25] J. Henin, G. Fiorin, C. Chipot, and M. L. Klein, "Exploring multidimensional free energy landscapes using time-dependent biases on collective variables," *J. Chem. Theory Comput.*, vol. 6, no. 1, pp. 35–47, 2010.

[26] S. C. Harvey, R. K.-Z. Tan, and T. E. Cheatham, "The flying ice cube: Velocity rescaling in molecular dynamics leads to violation of energy equipartition," *J. Comput. Chem.*, vol. 19, no. 7, pp. 726–740, 1998.

[27] M. J. Frisch, G. W. Trucks, H. B. Schlegel, G. E. Scuseria, M. A. Robb, J. R. Cheeseman, J. A. Montgomery, Jr., T. Vreven, K. N. Kudin, J. C. Burant, J. M. Millam, S. S. Iyengar, J. Tomasi, V. Barone, B. Mennucci, M. Cossi, G. Scalmani, N. Rega, G. A. Petersson, H. Nakatsuji, M. Hada, M. Ehara, K. Toyota, R. Fukuda, J. Hasegawa, M. Ishida, T. Nakajima, Y. Honda, O. Kitao, H. Nakai, M. Klene, X. Li, J. E. Knox, H. P. Hratchian, J. B. Cross, V. Bakken, C. Adamo, J. Jaramillo, R. Gomperts, R. E. Stratmann, O. Yazyev, A. J. Austin, R. Cammi, C. Pomelli, J. W. Ochterski, P. Y. Ayala, K. Morokuma, G. A. Voth, P. Salvador, J. J. Dannenberg, V. G. Zakrzewski, S. Dapprich, A. D. Daniels, M. C. Strain, O. Farkas, D. K. Malick, A. D. Rabuck, K. Raghavachari, J. B. Foresman, J. V. Ortiz, Q. Cui, A. G. Baboul, S. Clifford, J. Cioslowski, B. B. Stefanov, G. Liu, A. Liashenko, P. Piskorz, I. Komaromi, R. L. Martin, D. J. Fox, T. Keith, M. A. Al-Laham, C. Y. Peng, A. Nanayakkara, M. Challacombe, P. M. W. Gill, B. Johnson, W. Chen, M. W. Wong, C. Gonzalez, and J. A. Pople, "Gaussian 03, Revision C.02." Gaussian, Inc., Wallingford, CT, 2004.

[28] C. Adamo and V. Barone, "Toward reliable density functional methods without adjustable parameters: The PBE0 model," *J. Chem. Phys.*, vol. 110, no. 13, 1999.

[29] J. C. Phillips, R. Braun, W. Wang, J. Gumbart, E. Tajkhorshid, E. Villa,

C. Chipot, R. D. Skeel, L. Kale, and K. Schulten, “Scalable molecular dynamics with "NAMD",” *J. Comput. Chem*, vol. 26, p. 1781, 2005.

[30] U. Essmann, L. Perera, M. L. Berkowitz, T. A. Darden, H. Lee, and L. G. Pedersen, “A smooth particle mesh Ewald method,” *J. Chem. Phys*, vol. 103, p. 8577, 1995.

[31] H. J. C. Berendsen, J. P. M. Postma, W. F. van Gunsteren, A. Di Nola, and J. R. Haak, “Molecular dynamics with coupling to an external bath,” *J. Chem. Phys.*, vol. 81, pp. 3684–3690, Oct. 1984.

[32] L. Martinez, R. Andrade, E. G. Birgin, and J. M. Martinez, “Packmol: A package for building initial configurations for molecular dynamics simulations,” *. Comput. Chem.*, vol. 30, no. 13, pp. 2157–2164, 2009.

[33] S. M. Ryno, S. R. Lee, J. S. Sears, C. Risko, and J.-L. Brèdas, “Electronic polarization effects upon charge injection in oligoacene molecular crystals: Description via a polarizable force field,” *J. Phys. Chem. C*, vol. 117, no. 27, pp. 13853–13860, 2013.

[34] D. Demus and T. Inukai, “Calculation of molecular, dielectric and optical properties of 4ij-n-pentyl-’ -cyano-biphenyl(5CB),” *Liq. Cryst.*, vol. 26, no. 9, pp. 1257–1266, 1999.

[35] I. Chirtoc, M. Chirtoc, C. Glorieux, and J. Thoen, “Determination of the order parameter and its critical exponent for nCB (n=5 8) liquid crystals from refractive index data,” *Liq. Cryst.*, vol. 31, no. 2, pp. 229–240, 2004.

[36] G. Luckhurst, D. A. Dunmur, and A. Fukuda, *Physical properties of liquid crystals: nematics*. No. 25, IET, 2001.

[37] R. G. Horn, “Refractive indices and order parameters of two liquid crystals,” *J. Phys. France*, vol. 39, no. 1, pp. 105–109, 1978.

[38] S. J. Pickens, *Physical properties of liquid crystals: nematics*. No. 25, IET, 2001.

[39] B. M. Fung, J. Afzal, T. L. Foss, and M. H. Chau, “Nematic ordering of 4 n alkyl 4’ cyanobiphenyls studied by carbon 13 NMR with off magic angle spinning,” *J. Chem. Phys.*, vol. 85, pp. 4808–4814, Nov. 1986.

[40] A. Wuerflinger and M. Sandmann, *Physical properties of liquid crystals: nematics*. No. 25, IET, 2001.

[41] D. Frenkel and B. Smit, *Understanding Molecular Simulations: From Algorithms to Applications.* Academic Press, San Diego, 1996.

[42] M. F. Palermo, A. Pizzirusso, L. Muccioli, and C. Zannoni, “An atomistic description of the nematic and smectic phases of 4-n-octyl-4’ cyanobiphenyl (8CB),” *J. Chem. Phys.*, vol. 138, p. 204901, 2013.

[43] S. V. Dvinskikh, I. Furó, H. Zimmermann, and A. Maliniak, “Anisotropic self-diffusion in thermotropic liquid crystals studied by 1 H and 2 H pulse-field-gradient spin-echo NMR,” *Phys. Rev. E*, vol. 65, no. 6, p. 061701, 2002.

Chapter 7

Molecular dynamics simulations of liquid crystal-water solutions interfaces

7.1 Introduction

The average orientation of a nematic at the interface with water depends on the material, and for cyanobiphenyls with pure water it is planar, i.e. parallel to the interface itself. Numerous studies have recently shown that nematic liquid crystal (LC) phases can vary their direction of alignment when interfaced with aqueous solutions in the presence of ions or other species in the water[1]. This change of alignment is easily detectable since it changes the optical properties of the LC in a very obvious way and thus can be exploited to amplify events happening at the molecular scale close to the interface and employed in the design of sensing devices apt to reveal the presence of specific categories of compounds, such as biological ones[2].

In this chapter, we describe the characterization of these interfaces through molecular dynamics computer simulations in order to study the mechanism lying behind the alignment of LCs when interfaced with water solutions. Molecules were modeled at the atomistic resolution[3], with the LC phase consisting of 4-

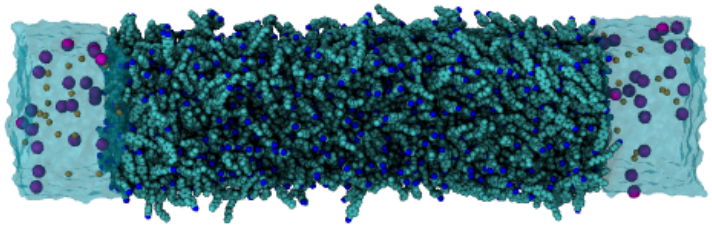

Figure 7.1: Snapshot of the LC-water interface studied in this project.

n-pentyl-4' cyanobiphenyl (5CB) and water solutions containing simple species such as monovalent ions, which are ubiquitous in all biological systems. We focused our attention mainly on the iodide ion I^-, since it is the only anion of the halide series that is experimentally found to homeotropically align 5CB with respect to the water interface[4]. The most credited hypothesis is that the driving force behind the alignment process is the onset of an electric field generated by the ions migrating from the aqueous to the LC phase[2].

7.2 Methods and computational details

To study this phenomenon, we run simulations on samples composed by 1000 5CB molecules and 5000 water molecules. A generic snapshot of the system can be seen in Figure 7.1. The simulated systems had a cell cross-section of 25 nm^2 and a cell height of 30 nm (with the LC phase extending for about 20 nm). Simulations were run in NVT conditions using NAMD[5] with multiple step integration: bonded, van der Waals and electrostatic interactions were calculated every 1, 2 and 4 fs respectively. The samples were kept at the constant temperature of 300 K through velocity rescaling. Simulations were run with periodic boundary conditions and long range electrostatic interactions were computed through the Particle Mesh Ewald method[6]. Each systems was simulated for a average production time of 100 ns.

7.3 Simulations and results

Pure water and 2 M NaI solution with original parameters

First, we simulated two systems, one with pure water and one with 2 M NaI solution. Water molecules were represented with the TIP3P model[7], Na^+ and I^- parameters were taken from ref[8] while for the 5CB liquid crystal phase, we took advantage of the non polarizable united atoms force field recently developed in our group which was validated for the nematic phase of cyanobiphenyls[9]. In Figure 7.2 we report the perpendicular and planar component of the director $\mathbf{n}$, which is the vector describing the average direction of the molecules in the LC phase, for the two systems. It can be seen that for both systems the director shows a planar alignment, with the component $n_\perp$ perpendicular to the interface and to the simulation box axis close to 0.

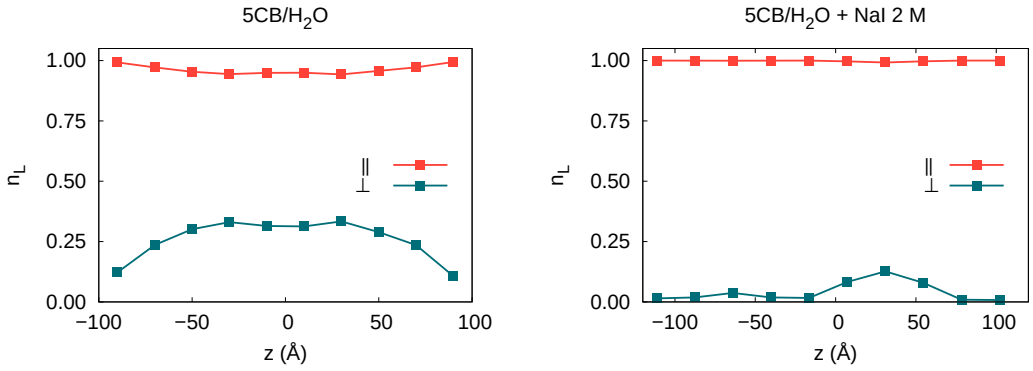

Figure 7.2: Perpendicular and planar components $n_\perp$ and $n_\parallel$ of the LC phase director for 5CB interfaced with pure water (on the left) and with a 2 M NaI solution (on the right).

10 M NaI solution and increased-size I^-

As said above, the alignment process is believed to be driven by the onset of an electric field generated by the ions migrating from the aqueous to the LC phase. Since the 2 M NaI solution did not yield the expected homeotropic alignment, we hypothesized that: a) the I^- concentration at the interface was too low to generate an electric field strong enough to align the LC phase; b) the model

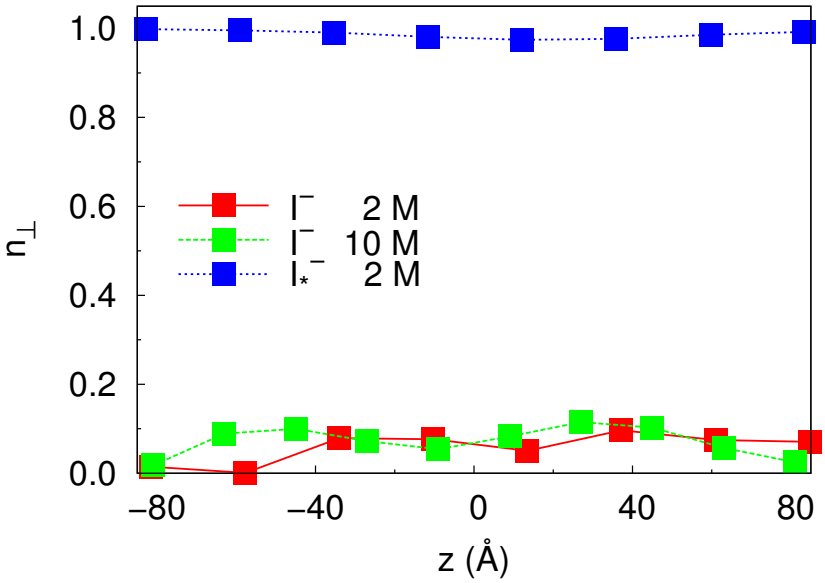

Figure 7.3: Perpendicular component of the LC phase director for 5CB interfaced with a 2 M NaI solution (red), a 10 M NaI solution (green) and a 2 M NaI solution with the increased radius for the anion (blue).

for I^- employed herein had a low affinity for the LC-water interface and thus did not migrate into the LC phase. In order to test these assumptions, we run two additional simulations, one where we increased the concentration of NaI to 10 M, and one where the radius of the iodide ion was increased of about 40%, keeping a 2 M concentration.

In Figure 7.3 we report the director component of the LC phase for the two simulations. It can be seen that the increase of ion concentration still leads to a planar orientation of the LC phase. On the other hand, the system with the increased ion affinity for the interface shows a homeotropic alignment of the LC phase.

To further investigate these results, we report in Figure 7.5 the linear density profiles for the three NaI systems studied until now. Density profiles were aligned with respect to the 5CB-water interface. In order to determine the exact position of the interface, we employed the sigmoid Boltzmann function to fit the density profile of the water phase:

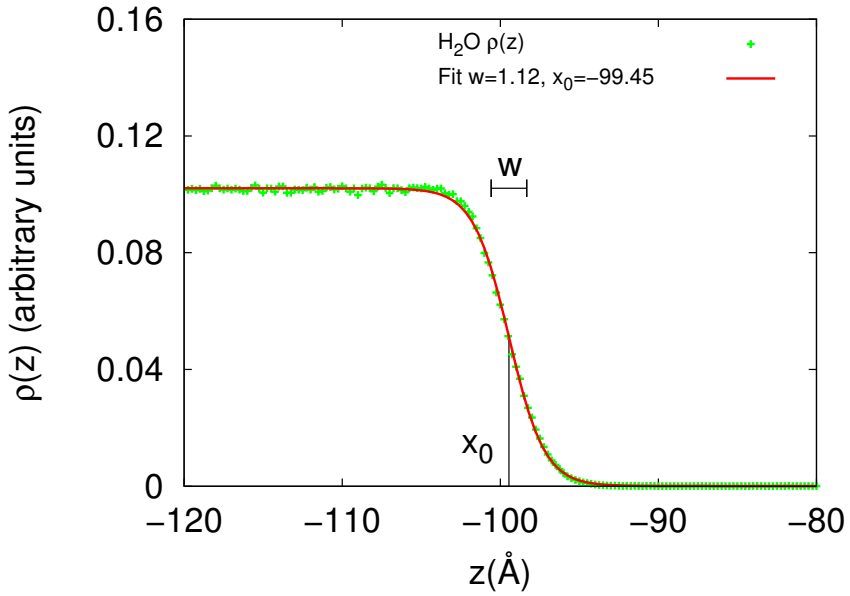

Figure 7.4: Density profile $\rho(z)$ in arbitrary unites of water at the interface with 5CB (green points). Sigmoid fit function employed to estimate the position of the interface x_0 (red line). x_0 is the position of the interface and w is the interface width obtained from the fit.

$$y = A_2 + \frac{(A_1 - A_2)}{1 + e^{[(x-x_0)/w]}}, \tag{7.1}$$

where A_1 and A_2 are the top and bottom asymptotic values, respectively, x_0 is the position of the interface and w is the width of the interface. In Figure 7.4 we report the density profile of water in the 2 M NaI sample, and it can be seen that the sigmoid function fits well the interface density profile of water. Therefore, the density profiles of I^- for the three samples were aligned by centering them at x_0 = 0.

It can be observed that no diffusion of the ions within the LC phase is detected for the simulations run with the original ion parameters, regardless of the NaI concentration. The system featuring the I^- with increased radius instead shows a significant penetration of both the anion and cation within the LC phase, with the formation of an electric double layer. This confirms the assumption that the migration of the ions in the LC phase is of key importance in order to trigger its homeotropic alignment.

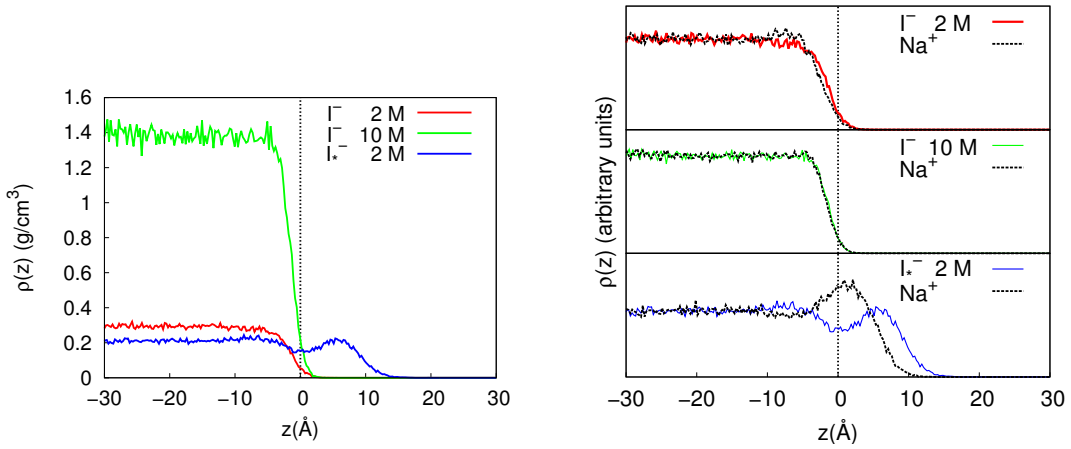

(a) (b)

Figure 7.5: In Figure a, density profile along the normal to the interface $\rho(z)$ the 2 M NaI solution (red), a 10 M NaI solution (green) and a 2 M NaI solution with the increased radius for the anion (blue). In Figure b, density profiles in arbitrary units of both cation and anion (Na^+). The vertical dashed line represents the LC–water interface, with 5CB on the right and water on the left

The MD technique also allows to extract the charge density profiles from the simulation trajectory by diving the sample in regions of equal width, summing all the charges within each region and eventually diving by the volume of the sampled portion of the sample. From the charge density profiles, we can compute the electric field and potential raising from the ion distributions at the interfaces for the three samples. The electric field $E(z)$ and potential $V(z)$ along an arbitrary direction z can be obtained starting from the Poisson equation in one dimension:

$$\frac{\partial^2 \phi(z)}{\partial z^2} = -\frac{\rho(z)}{\varepsilon_0 \varepsilon_r}\,, \tag{7.2}$$

which can be integrated to obtain the electric field $E(z)$:

$$E(z) = \int_{z0}^{z} \frac{\rho(z)}{\varepsilon_0 \varepsilon_r}\, dz\,. \tag{7.3}$$

In turn, the electric field can be integrated to obtain the potential profile $V(z)$:

$$V(z) = -\int_{z0}^{z} E(z)\, dz\,. \tag{7.4}$$

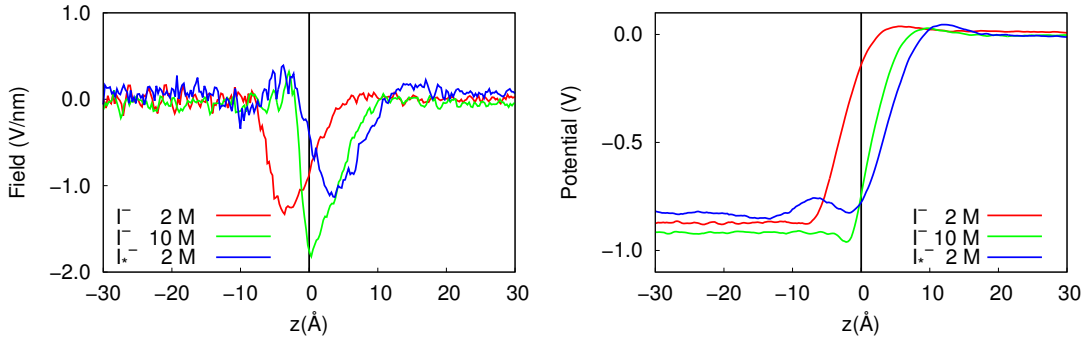

Figure 7.6: On the left, total electric field profile for the 2 M NaI sample (original parameters), 10 M NaI sample (original parameters) and the 2 M NaI sample (modified parameters) along the direction normal to the interface z. On the right, total electric potential profiles for the three systems along z.

In Figure 7.6 we report the $E(z)$ and $V(z)$ profiles along the normal to the interface. It can be seen that the the 2 M NaI sample with the original parameters features a negative peak within the water phase, thus no electric field gradient is present within the LC phase, preventing the onset of the homeotropic alignment. The 10 M sample instead, features a much deeper negative peak, with a minima located exactly at the interface and we observe a gradient of electric field also within the LC phase. In the 2 M sample of NaI with the modified parameters for the I^- we find that the negative peak is completely shifted within the LC phase, although the peak intensity is smaller than in the 10 M sample. This suggests that the presence of a gradient with the negative peak within the LC phase is mandatory in order to observe the onset of homeotropic alignment of 5CB molecules. Again in Figure 7.6, the resulting electric potential derived from the field profiles can be found. We can observe that in all samples, positively charged ions are stabilized in the water phase, as $V(z)$ assumes a negative value, while the negative ones are favoured in the LC phase and that there is a potential barrier of up to 1 V across the interfacial region. The three profiles differ in that $V(z)$ for the sample with modified parameters is slightly

more shifted towards the LC phase, thus extending the region in the LC phase where cations can still be stabilized and therefore favouring the onset of an electric double layer.

Accordingly, it can be seen in Figure Fig. 7.7, where we report also the partial contribution to the total $E(z)$, that the 2 M NaI sample with modified parameters differentiates itself from all the others as it shows a positive peak in the ion contribution within the LC phase (Fig. 7.7b). While with the original parameters the cumulative contribution of water and ions to the total electric field is negative at the interface, the sample with modified parameters is the only one featuring a positive peak beyond the interface (Fig. 7.7c). Moreover, the onset of homeotropic alignment of the LC phase determines an increment of the negative field generated by 5CB, which is larger than the one found for all the other samples with a planar orientation of the LC molecules with respect to the interface.

Unfortunately, we succeeded in reproducing the homeotropic alignment of the LC phase only by employing unphysical parameters for the I^- ion, i.e. increasing the LJ radius, suggesting a difficulty of classical force fields with static charges[7–9] in reproducing the homeotropic alignment observed experimentally.

System fully described with polarizable models

Since this phenomenon relies on electrostatic interactions, a proper description of the induced polarization on 5CB, arising from the perturbation of the electronic structure of the LC molecules in response to the electric field generated by the ions, might be fundamental to reproduce the experimental homeotropic alignment. Therefore we parametrized a united atom polarizable model of 5CB, where the effect of the electronic polarizability was simulated through the use of Drude particles[10], and then proceeded with simulating a system fully described with polarizable models. Details on the model, on its parametrization and its validation are reported in Chapter 6.

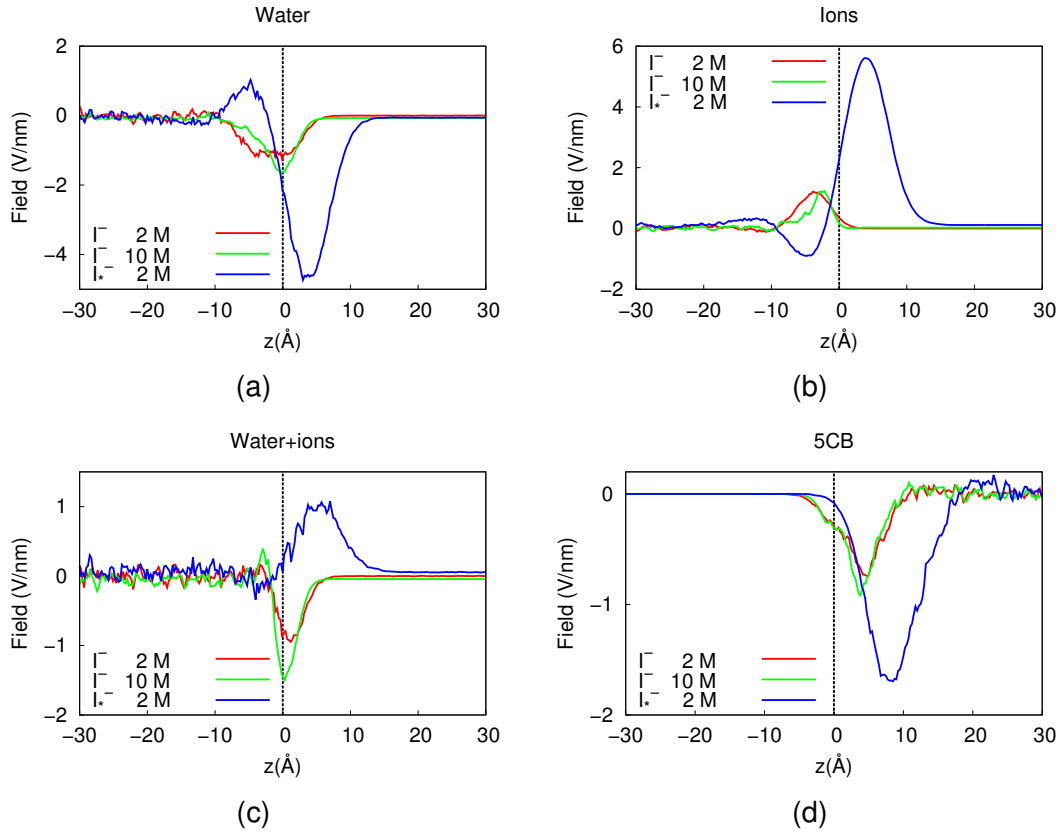

Figure 7.7: Electric field profiles for the 2 M NaI sample (original parameters), 10 M NaI sample (original parameters) and the 2 M NaI sample (modified parameters) along the direction normal to the interface z of a) water, b) ions, c) H_2O+Ions and d) 5CB.

The polarizable model was applied to the water-LC system, and the simulation was run for 80 ns, a time in which the system did not reach equilibrium. Water was modeled with the polarizable SWM4-NDP[11] and parameters for the Na^+ and I^- parameters were taken from ref[12]. Visual inspection, as well as density profiles of the sample reported in Figure 7.8 show that the LC phase diffuses in the aqueous one, suggesting that the 5CB polarizable molecule might form an intermixed interfacial region with water at the nanometric scale. In the last 5 ns of the simulation, we found the onset of a partially homeotropic alignment at the interfaces and in the bulk of the LC phase.

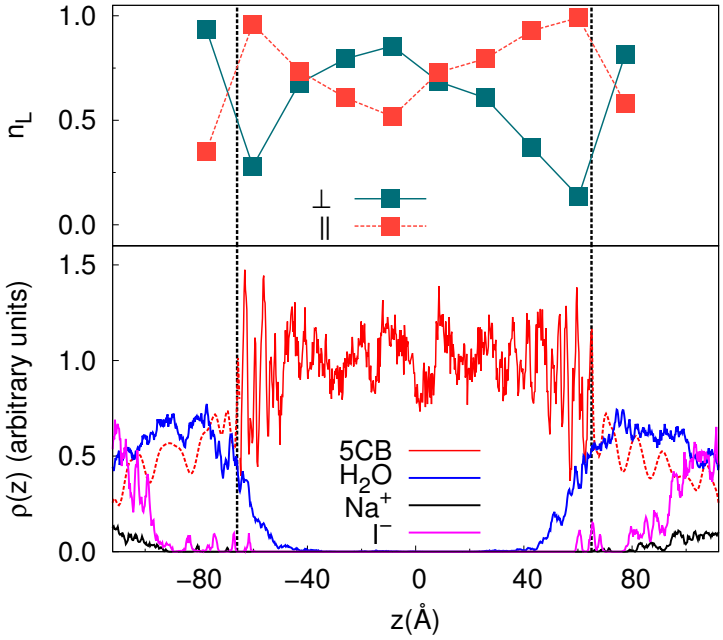

(a)

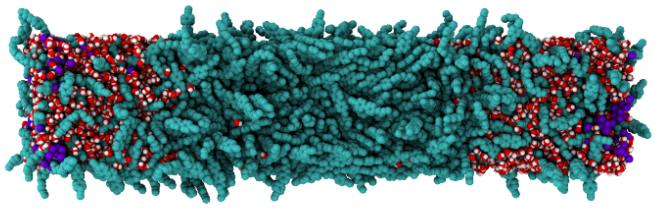

(b)

Figure 7.8: Figure a on top, parallel and perpendicular components of the LC phase director and density profiles (in arbitrary units) of the LC-water interface modeled with polarizable FF. In Figure b on bottom, snapshot of the LC-water interface modeled with polarizable FF.

This can be seen in Figure 7.8, where we report the perpendicular and planar component of the director, which is the vector describing the average alignment of the molecules in the LC phase. It can be observed that the perpendicular component is close to 1 at the two interfaces and comprised between 0.6 and 0.8 in the middle of the sample, with a narrow planar region in between.
We have not been able to effectively compute the total electric field $E(z)$ and the potential $V(z)$ and compare it with the results obtained from other samples as the charge density obtained from this system is too noisy.

7.4 Influence of other ions on the LC orientation

While I^- may be the most simple anion leading to the onset of a homeotropic alignment of the LC phase with respect to the interface with water, it is not the only one. In particular, it has been shown that also the perchlorate ion ClO_4^- is capable of determining a homeotropic alignment of the LC phase. Moreover, we also tested the assumption that it is not sufficient for ions to migrate just to the interface to generate a change in the orientation of the LC phase, by introducing a amphiphile tensioactive molecule that would target the interface (phenyl sulfate, $PhSO_3^-$). Parameters were again taken from the AMBER force field and missing ones were re-parametrized by fitting ab-initio results. Simulations were run by employing the same conditions as reported for the I^- ion.
In Figure 7.9 we report the perpendicular component of the LC director for 5CB interfaced with the solution of ClO_4^- and $PhSO_3^-$ anions, compared with the director component for the sample with the modified parameters.
It can be seen that either ions do not lead to a homeotropic alignment of the LC phase. This is expected for the sample with the $PhSO_3^-$ anion, as it was chosen to target the interface, while the result for ClO_4^- is at variance with the experimental findings[4].
Once again, we look at the density profiles of the ions to investigate their distribution at the interface, in Figure 7.10.
It can be seen that $PhSO_3^-$ anion has a high interfacial concentration due to its

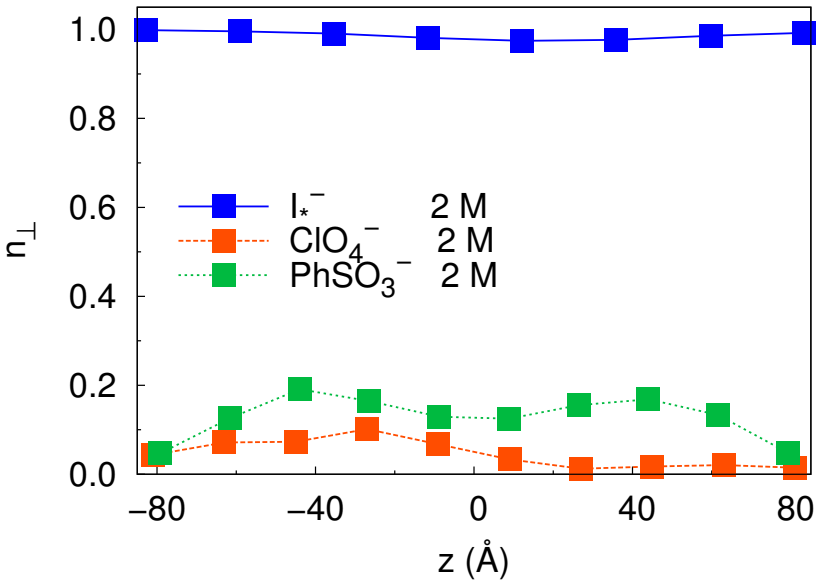

Figure 7.9: Perpendicular component of the LC phase director for 5CB interfaced with a 2 M NaI solution with modified parameters (blue), 2 M $NaClO_4$ and 2 M $PhSO_3Na$.

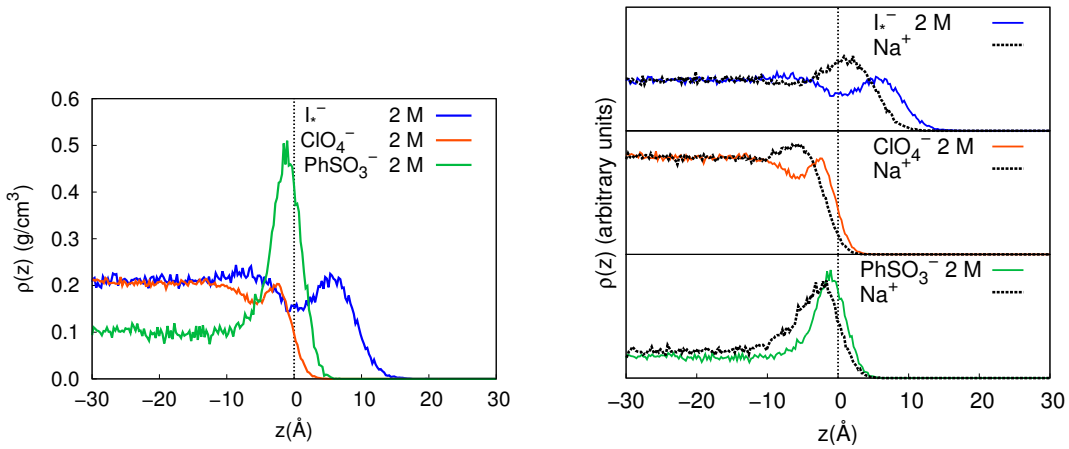

Figure 7.10: In Figure a, density profile along the normal to the interface $\rho(z)$ of the modified I^- (blue), ClO_4^- (orange) and $PhSO_3^-$ (green). In Figure b, density profiles in arbitrary units of both cation and anion (Na^+).

amphiphilic nature, but does not diffuse in the LC phase, with the concentration peak decaying drastically after the interface. On the other hand, the density profile for ClO_4^- shows almost no diffusion of the anion in the LC phase and therefore does not trigger the homeotropic alignment of the LC phase that is found experimentally. In Figure 7.10b it can also be noticed that none of the two ions form an electric double layer with Na^+ in the LC phase, as it is instead found for the sample with the modified set of parameters for the iodide ion.
In Figure 7.11 we inspect the influence of the two new anions on the electric field along z, compared to that of the modified I^-.

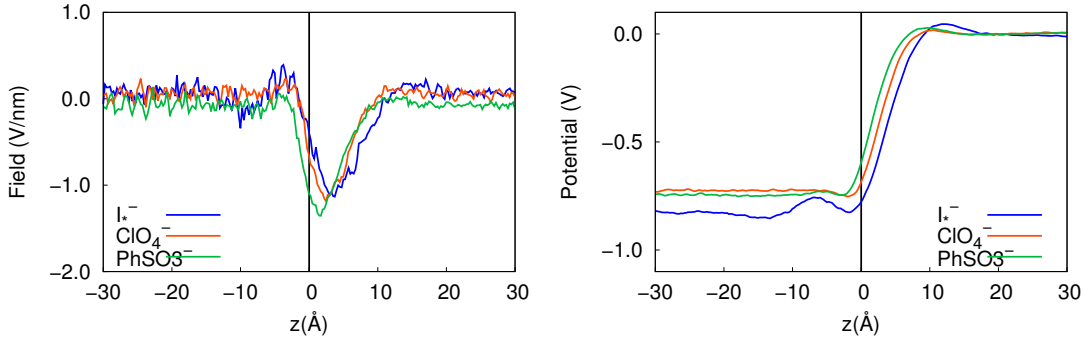

Figure 7.11: On the left, total electric field profile $E(z)$ for the 2 M NaI with modified parameters (blue), 2 M ClO_4^- (orange) and 2 M $PhSO_3^-$ (green) samples along the direction normal to the interface z. On the right, total electric potential profile $V(z)$ for the three systems along z.

It can be seen that, even though no homeotropic alignment was found in the samples, the electric field $E(z)$ in the systems with the two anions is quite similar to the one found for the modified I^-, with a negative peak beyond the interface. Consequently, also the electric potential profile $V(z)$ will not differ much from the one of the modified I^-, even though it appears that in the two new samples, cations are less stabilized in the water phase due to the slightly higher potential.
The fact the total electric field profile for the samples with 2 M ClO_4^- and $PhSO_3^-$ is surprisingly similar to the one of the modified I^- should not deceive, as it might result from different contribution. The partial contributions of ions, water and 5CB are reported in Figure 7.12.

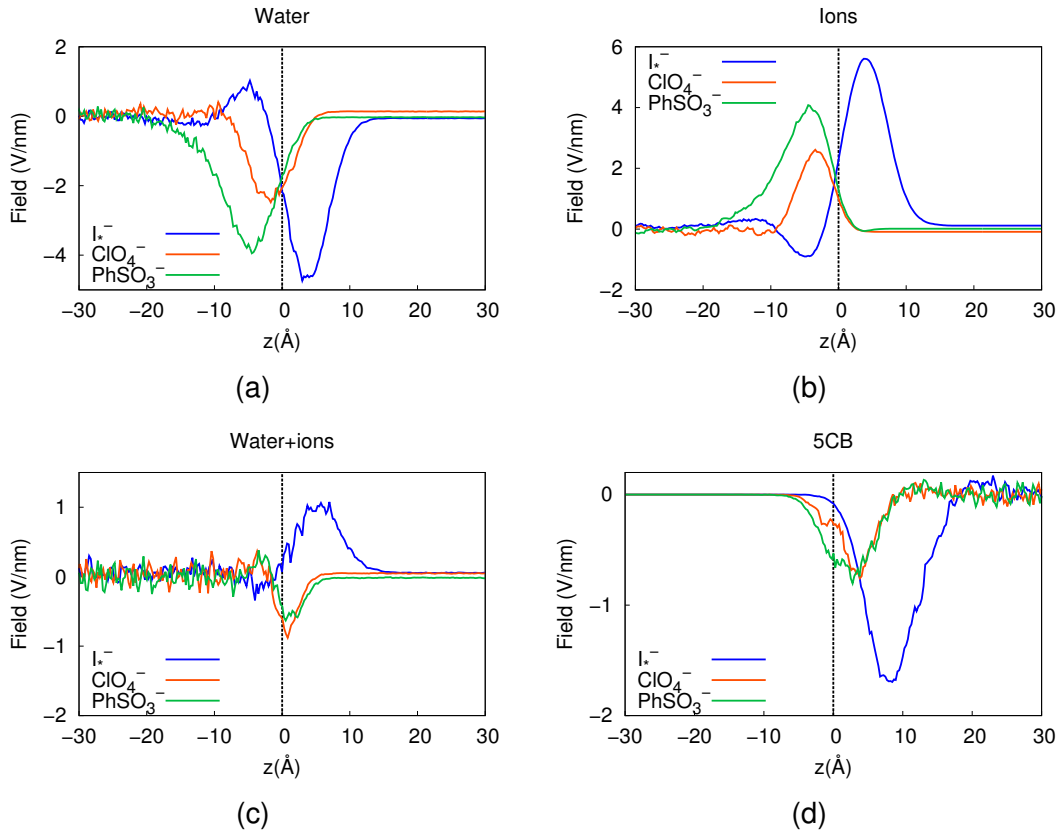

Figure 7.12: Electric field profiles for the 2 M NaI with modified parameters (blue), 2 M ClO_4^- (orange) and 2 M $PhSO_3^-$ (green) samples along the direction normal to the interface z of a) water, b) ions, c) H_2O+Ions and d) 5CB.

In fact, it can be noticed that in the 2 M ClO_4^- and $PhSO_3^-$ samples, ions feature a positive peak in the water and not within the LC phase, and thus do not lead to the homeotropic alignment of 5CB molecules. Moreover, the gradient of $E(z)$ are smaller than in the sample with the modified I^-, even though greater than those found for both the 2 M and 10 M samples with the original parameters. The partial contribution of 5CB to $E(z)$ is similar to the ones found for the sample with I^- with original parameters, which is consistent with the absence of homeotropic alignment of the LC phase.

7.5 Conclusions

We have investigated the water–LC interface for pure water and solutions of water with electrolyte species (NaI, $NaClO_4$) that are known to induce homeotropic

alignment on the liquid crystal phase by means of atomistic molecular dynamics simulations. By computing the components of the director of the LC phase in the samples, we found that the results obtained by employing static charges force field to model ions, water and 5CB were at variance with the experimental findings, with the LC phase aligning parallel to the water–LC interface. Among all simulated samples, the LC phase reorientation has been observed only by unphysically increasing the radius of the iodide ion, which apparently led to an increased interface affinity of the anion.

It was observed that the diffusion of ions beyond the interface from water to 5CB and the onset of a electric double layer are key factors to the reorientation of the LC phase. This study also led to the development of a polarizable force field for 5CB, which is still being tested to verify whether it could be employed to describe the LC-water interface and the interaction with the weak electric field raised by ions.

Bibliography

[1] Y. Bai and N. L. Abbott, "Recent advances in colloidal and interfacial phenomena involving liquid crystals," *Langmuir*, vol. 27, no. 10, pp. 5719–5738, 2011.

[2] I.-H. Lin, D. S. Miller, P. J. Bertics, C. J. Murphy, J. J. d. Pablo, and N. L. Abbott, "Endotoxin-induced structural transformations in liquid crystalline droplets.," *Science*, vol. 332, no. 6035, pp. 1297–1300, 2011.

[3] M. F. Palermo, A. Pizzirusso, L. Muccioli, and C. Zannoni, "An atomistic description of the nematic and smectic phases of 4-n-octyl-4' cyanobiphenyl (8cb)," *J. Chem. Phys.*, vol. 138, p. 204901, 2013.

[4] R. J. Carlton, C. D. Ma, J. K. Gupta, and N. L. Abbott, "Influence of specific anions on the orientational ordering of thermotropic liquid crystals at aqueous interfaces," *Langmuir*, vol. 28, pp. 12796–12805, 2012.

[5] J. C. Phillips, R. Braun, W. Wang, J. Gumbart, E. Tajkhorshid, E. Villa, C. Chipot, R. D. Skeel, L. Kale, and K. Schulten, “Scalable molecular dynamics with "NAMD",” *J. Comput. Chem.*, vol. 26, p. 1781, 2005.

[6] U. Essmann, L. Perera, M. L. Berkowitz, T. A. Darden, H. Lee, and L. G. Pedersen, “A smooth particle mesh Ewald method,” *J. Chem. Phys*, vol. 103, p. 8577, 1995.

[7] D. J. Price and C. L. Brooks, “A modified tip3p water potential for simulation with ewald summation,” *J. Chem. Phys.*, vol. 121, pp. 10096–10103, 2004.

[8] I. S. Joung and T. E. Cheatham, “Determination of Alkali and Halide Monovalent Ion Parameters for Use in Explicitly Solvated Biomolecular Simulations,” *J. Phys. Chem. B*, vol. 112, pp. 9020–9041, 2008.

[9] G. Tiberio, L. Muccioli, R. Berardi, and C. Zannoni, “Towards in silico liquid crystals. realistic transition temperatures and physical properties for n-cyanobiphenyls via molecular dynamics simulations,” *ChemPhysChem*, vol. 10, pp. 125–136, 2009.

[10] G. Lamoureux and B. Roux, “Modeling induced polarization with classical drude oscillators: Theory and molecular dynamics simulation algorithm,” *J. Chem. Phys.*, vol. 119, pp. 3025–3039, 2003.

[11] G. Lamoureux, E. Harder, I. V. Vorobyov, B. Roux, and A. D. MacKerrel Jr., “A polarizable model of water for molecular dynamics simulations of biomolecules,” *Chem. Phys. Lett.*, vol. 418, pp. 245–249, 2006.

[12] H. Yu, T. W. Whitfield, E. Harder, G. Lamoureux, I. V. Vorobyov, V. M. Anisimov, A. D. MacKerrel Jr., and B. Roux, “A polarizable model of water for molecular dynamics simulations of biomolecules,” *J. Chem. Theory Comput.*, vol. 6, pp. 774–786, 2010.